



Steel Centre Engineering Report No. 015 | October 2019

# LARGE-SCALE LATERAL-TORSIONAL BUCKLING TESTS OF WELDED GIRDERS

Dimple Ji

Robert G. Driver

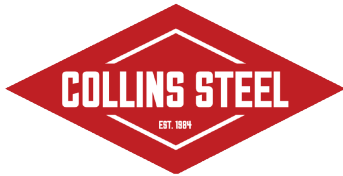
Ali Imanpour



## External Sponsor



## Steel Centre Industry Partners



**WF STEEL  
& CRANE**



---

**DIALOG®**



---

**TSE TSE STEEL LTD.**

**PRICE STEEL LTD.**

## **Large-scale Lateral–Torsional Buckling Tests of Welded Girders**

by

Dimple Ji

Robert G. Driver

and

Ali Imanpour

Steel Centre Engineering Report No. 015

## ABSTRACT

Lateral–torsional buckling is a stability-related failure mode of unbraced or insufficiently braced flexural members. In recent years, several concerns have been raised regarding the adequacy of the Canadian steel design standard, CSA S16-14, in characterising the lateral–torsional buckling resistance of members made up of three plates welded together into an I-shaped section, as is commonly done for deep girders. The large heat input from welding results in residual stress distributions that may cause these welded sections to be more susceptible to lateral–torsional buckling than their rolled counterparts, particularly in the inelastic region. However, the paucity of up-to-date physical test data for modern welded girders considerably limits the potential for an adequate evaluation of the current design provisions.

To improve the understanding of lateral–torsional buckling behaviour, an experimental programme was developed, consisting of 11 welded girders with unbraced spans of 9.75 m (32 ft). Test specimens were selected and designed by considering various parameters that may influence lateral–torsional buckling resistance. Preliminary finite element simulations were conducted to anticipate displacements and rotations of the test specimens, which were used to inform the design of an experimental test set-up capable of accommodating the full range of expected movement. The observed moment resistances and stability response from seven tests were analysed, and the effects of initial geometric imperfections, residual stresses, and geometric parameters were considered. Test results were compared against predictions from CSA S16-14, with adjustments applied to account for load height effects from the gravity load mechanism, and the adequacy of the Canadian provisions for lateral–torsional buckling resistance was evaluated.

## ACKNOWLEDGEMENTS

This research was funded by the Natural Sciences and Engineering Research Council and the Canadian Institute of Steel Construction. The first author wishes to acknowledge financial support in the form of scholarships from the University of Alberta, the Government of Alberta, DIALOG, and the Canadian Institute of Steel Construction. All plate material for girders was generously donated by SSAB; fabrication of girders and ancillary testing fixtures was completed by Supreme Group and is gratefully acknowledged.

Thank you to Greg Miller and Cameron West, whose guidance in the laboratory contributed significantly to the success of the physical testing programme. The discussions and constructive comments from professors and fellow students of the Steel Centre are also greatly appreciated.

## TABLE OF CONTENTS

<b>1</b>	<b>INTRODUCTION.....</b>	<b>1</b>
1.1	Background .....	1
1.2	Statement of Research Problem .....	2
1.3	Objectives and Scope .....	2
1.4	Organisation of Report .....	3
<b>2</b>	<b>LITERATURE REVIEW .....</b>	<b>4</b>
2.1	Design of Laterally Unsupported Girders .....	4
2.1.1	Classic Lateral–Torsional Buckling Solution .....	4
2.1.2	CSA S16-14 (2014).....	5
2.1.3	CSA S6-14 (2014).....	6
2.1.4	ANSI/AISC 360-16 (2016).....	6
2.2	Factors Affecting Lateral–Torsional Buckling .....	7
2.2.1	Residual Stress .....	7
2.2.2	Initial Geometric Imperfections .....	9
2.2.3	Load Height .....	10
2.3	Previous Physical Testing of Rolled and Welded Laterally Unsupported Girders .....	11
2.3.1	Dibley (1969).....	11
2.3.2	Dux and Kitipornchai (1983).....	12
2.3.3	Wong-Chung and Kitipornchai (1987).....	12
2.3.4	Fukumoto (1976) .....	13
2.3.5	Fukumoto and Kubo (1977).....	14
2.3.6	Fukumoto et al. (1980).....	14
2.3.7	Fukumoto and Itoh (1981) .....	15
2.4	Previous Analytical Studies of Rolled and Welded Laterally Unsupported Girders .....	16
2.4.1	European Convention for Constructional Steelwork (1976) .....	17
2.4.2	MacPhedran and Grondin (2011).....	17
2.4.3	Kabir and Bhowmick (2016; 2018) .....	19
2.4.4	Subramanian and White (2017) .....	22

2.5	Summary .....	23
<b>3</b>	<b>TEST GIRDER CHARACTERISTICS .....</b>	<b>25</b>
3.1	Test Specimen Matrix .....	25
3.1.1	Load Configuration .....	25
3.1.2	Cross-section Geometry .....	26
3.1.3	Test Constraints .....	28
3.1.4	Test Specimen Selection .....	29
3.1.4.1	Range of Inelastic Behaviour .....	31
3.1.4.2	Geometric Variability .....	32
3.1.4.3	Aspect Ratio .....	32
3.1.4.4	Section Class .....	33
3.1.4.5	Cutting Method .....	34
3.2	Test Girder Design .....	34
3.3	Measurement of Initial Geometric Imperfections .....	36
3.3.1	Cross-section Measurements .....	37
3.3.2	Global Geometric Measurements .....	40
3.4	Measurement of Residual Stresses .....	44
3.5	Material Properties .....	50
<b>4</b>	<b>EXPERIMENTAL PROGRAMME .....</b>	<b>52</b>
4.1	Preliminary Pre-test Models .....	52
4.1.1	Elements and Meshing .....	52
4.1.2	Material Properties .....	53
4.1.3	Boundary Conditions .....	53
4.1.4	Loading Procedure .....	56
4.1.5	Model Verification .....	57
4.1.6	Results and Discussion .....	60
4.2	Test Set-up .....	65
4.2.1	Gravity Load Application .....	66
4.2.1.1	Gravity Load Simulator .....	67
4.2.1.2	Hydraulic Actuator .....	70

4.2.1.3	Load Collar .....	70
4.2.1.4	Summary .....	73
4.2.2	End Conditions.....	74
4.3	Instrumentation.....	76
4.4	Test Procedure.....	80
<b>5</b>	<b>RESULTS AND DISCUSSION .....</b>	<b>83</b>
5.1	Girder Capacity Results .....	83
5.1.1	Obtained Range of Inelastic Behaviour .....	85
5.1.2	Effect of Geometric Properties .....	85
5.1.3	Effect of Cutting Method and Residual Stresses .....	88
5.2	Girder Displacement Results.....	89
5.2.1	Global Displacement Response and Observations .....	93
5.2.2	Lateral and Vertical Displacements at Buckling .....	94
5.2.2.1	Effect of Geometric Properties .....	95
5.2.2.2	Effect of Initial Geometric Imperfections .....	96
5.3	Flange Stress Analysis .....	99
5.4	Comparison of Experimental Results with Design Equations .....	104
5.4.1	Predicted Capacities – Shear Centre Loading.....	105
5.4.1.1	Effect of Lateral and Vertical Displacements at Buckling .....	107
5.4.1.2	Effect of Initial Geometric Imperfections .....	108
5.4.2	Predicted Capacities – Top Flange Loading .....	110
5.5	Experimental Errors .....	115
5.6	Discussion on the Adequacy of CSA S16-14 .....	117
<b>6</b>	<b>CONCLUSIONS AND RECOMMENDATIONS.....</b>	<b>119</b>
6.1	Summary .....	119
6.2	Conclusions .....	120
6.3	Recommendations for Further Research .....	121
	<b>REFERENCES.....</b>	<b>123</b>
	<b>Appendix A: Test Girder Drawings .....</b>	<b>128</b>
	<b>Appendix B: Measured Initial Geometric Imperfections.....</b>	<b>141</b>

**Appendix C: Material Test Results ..... 149**  
**Appendix D: Numerical Analysis Load–Displacement Curves ..... 152**  
**Appendix E: Experimental Load–Displacement Curves ..... 158**

## LIST OF TABLES

Table 2-1: Load height adjustment coefficients by Nethercot and Rockey (1971) .....	10
Table 2-2: Summary of Fukumoto (1976) test girders .....	13
Table 2-3: Number of reviewed experiments by Fukumoto and Kubo (1977).....	14
Table 2-4: Summary of imperfection measurements by Fukumoto et al. (1980).....	15
Table 3-1: Test specimen matrix.....	30
Table 3-2: Test specimen mean as-built dimensions .....	39
Table 3-3: Measured initial global geometric imperfections in test specimens.....	42
Table 3-4: Mean initial sweep and twist in different LTB studies .....	44
Table 3-5: Summary of tension coupon material properties.....	51
Table 4-1: Summary of buckling capacities for numerical model verification .....	58
Table 4-2: FE results of displacements and rotations at buckling .....	62
Table 4-3: Comparison of FE and CSA S16-14 predictions of test girder capacity.....	65
Table 4-4: Displacement demand and capacity .....	73
Table 5-1: Summary of girder capacities from experimental testing .....	84
Table 5-2: Summary of mid-span displacements at buckling.....	91
Table 5-3: Summary of mid-span displacements at ultimate.....	92
Table 5-4: Measured initial geometric imperfections and top flange lateral displacement at buckling.....	97
Table 5-5: Comparison of moment resistances from experimental results and design provisions .....	106
Table 5-6: Percent difference between test capacities of Fukumoto and Itoh (1981) and CSA S16-14 predictions with load height modifications .....	111
Table 5-7: Comparison of moment resistances from experimental results and CSA S16-14 predictions with load height modifications.....	113

## LIST OF FIGURES

Figure 2-1: Conceptual beam design curve .....	6
Figure 2-2: Representative residual stress pattern of (a) universal-mill and (b) flame-cut plates, where ‘C’ is compression and ‘T’ is tension (adapted from Chernenko and Kennedy 1991).....	8
Figure 2-3: Schematic residual stress pattern of (a) rolled section and (b) welded section, where ‘C’ is compression and ‘T’ is tension (Unsworth et al. 2019).....	9
Figure 2-4: Comparison of CSA S16-01 and proposed equation by MacPhedran and Grondin (2011) for (a) rolled and (b) welded sections.....	19
Figure 2-5: Comparison of FE results by Kabir and Bhowmick (2016) using the Fukumoto and Itoh (1981) residual stress pattern.....	21
Figure 2-6: Comparison of FE results by Kabir and Bhowmick (2016) using the mill plate residual stress pattern.....	21
Figure 3-1: Load configuration.....	26
Figure 3-2: Effect of flange thickness and width on LTB resistance .....	27
Figure 3-3: Effect of section depth and flange width on LTB resistance .....	28
Figure 3-4: LTB resistance vs. slenderness ratio for test specimens .....	31
Figure 3-5: Flange and web classes of selected test specimens.....	33
Figure 3-6: Measurement locations along test girder .....	36
Figure 3-7: Cross-section measurements of test specimens .....	37
Figure 3-8: Camber measurement methodology.....	41
Figure 3-9: Initial sweep measurement of G8-430-25-2-p .....	43
Figure 3-10: Initial twist measurement of G8-430-25-2-p .....	43
Figure 3-11: Sectioning strips for residual stress measurements (Unsworth et al. 2019).....	45
Figure 3-12: Residual stress distribution of G6-430-32-1-p (source data: Unsworth et al. 2019)	46
Figure 3-13: Residual stress distribution of G6-430-32-1-f (source data: Unsworth et al. 2019)	47
Figure 3-14: Residual stress distribution of G6-300-32-1-p (source data: Unsworth et al. 2019)	48
Figure 3-15: Residual stress distribution of G8-430-25-2-p (source data: Unsworth et al. 2019)	49
Figure 3-17: Ancillary girder used for residual stress measurements and material testing (adapted from Unsworth et al. 2019).....	50

Figure 3-18: Tension coupon locations.....	51
Figure 4-1: Stress–strain relationship used in numerical model.....	53
Figure 4-2: Conventions for degrees of freedom in numerical model.....	54
Figure 4-3: Boundary conditions in FE model .....	55
Figure 4-4: Load application to a nine-node, 2×2 element area .....	57
Figure 4-5: Load–displacement response comparing FE and experimental test results of Fukumoto et al. (1980) for 2.6 m series .....	59
Figure 4-6: Load–displacement response comparing FE and experimental test results of Fukumoto et al. (1980) for 2.0 m series .....	59
Figure 4-7: Load–displacement response comparing FE and experimental test results of Fukumoto et al. (1980) for 1.5 m series .....	60
Figure 4-8: Measurement locations in FE analysis.....	61
Figure 4-9: Ratio of lateral-to-vertical displacement at mid-span at buckling vs. slenderness ratio .....	63
Figure 4-10: Ratio of lateral-to-vertical displacement at mid-span at buckling vs. moment of inertia about minor axis.....	64
Figure 4-11: Load–displacement response from FE analysis: (a) G6-470-32-2-p and (b) G9-360-25-3-f .....	64
Figure 4-12: Model of experimental test set-up (test specimen shown in blue).....	66
Figure 4-13: Components of the gravity load mechanism.....	67
Figure 4-14: GLS maintains vertical load application as it sways laterally .....	68
Figure 4-15: Mid-span bracing to prevent excessive lateral displacement.....	69
Figure 4-16: Load collar components .....	71
Figure 4-17: Slotted angle connection in roller assembly .....	72
Figure 4-18: Fabricated gravity load mechanisms.....	74
Figure 4-19: Girder end support .....	75
Figure 4-20: Lateral bracing at boundary support .....	75
Figure 4-21: Instrumentation .....	76
Figure 4-22: Flange lateral displacement measurements at mid-span using the Miller–West Glider .....	77

Figure 4-23: Vertical displacement measurement at mid-span.....	78
Figure 4-24: Optical strain imaging set-up (a) overview, and (b) typical speckled area of interest at mid-span.....	79
Figure 4-25: Turnbuckle system for each GLS.....	81
Figure 5-1: Moment resistance vs. slenderness ratio .....	85
Figure 5-2: Moment resistance vs. St. Venant torsional stiffness.....	87
Figure 5-3: Moment resistance vs. warping stiffness .....	87
Figure 5-4: Cardinal directions of the test set-up (plan view) .....	90
Figure 5-5: Load–displacement response of G6-300-32-1-p.....	95
Figure 5-6: Load–displacement response of G8-430-25-2-p.....	95
Figure 5-7: Top and bottom flange load–displacement response of G8-390-32-2-p.....	98
Figure 5-8: Area of interest from digital imaging correlation divided into 30 mm × 600 mm strips; contours represent longitudinal strains of G6-430-32-1-p at buckling.....	100
Figure 5-9: Section curvature relationship to determine stresses at exterior and interior faces of the top flange .....	101
Figure 5-10: Top flange stress distribution at buckling of G6-430-32-1-p .....	102
Figure 5-11: Top flange stress distribution at buckling of G6-430-32-1-f.....	102
Figure 5-12: Top flange stress distribution at buckling of G6-300-32-1-p .....	103
Figure 5-13: Top flange stress distribution at buckling of G8-430-25-2-p .....	103
Figure 5-14: Plan view of top flange undergoing minor-axis bending.....	104
Figure 5-15: Moment resistances from test results and design equations .....	107
Figure 5-16: Relationship between test-to-predicted ratio and $\delta_h/\delta_v$ .....	108
Figure 5-17: Relationship between test-to-predicted ratio and initial top flange sweep .....	109
Figure 5-18: Relationship between test-to-predicted ratio and initial twist.....	109
Figure 5-19: Moment resistances from test results and design equations, adjusted for top flange loading.....	112
Figure 5-20: Centring of rotational hemisphere on flange width .....	116

## LIST OF SYMBOLS

$A$	=	Coefficient for moment gradient distribution in load height adjustment approximation from <i>SSRC Guide</i> (Galambos 1998);
$A_c$	=	Area of the compression flange
$a$	=	Parameter for determining $A$ in load height adjustment approximation from <i>SSRC Guide</i> (Galambos 1998)
$B$	=	Coefficient in load height adjustment approximation from <i>SSRC Guide</i> (Galambos 1998)
$b$	=	Flange thickness
$b_e$	=	Distance from flange tip to web
$C_b$	=	Moment gradient factor in AISC 360-16
$C_w$	=	Warping torsional constant
$c$	=	Distance from the extreme fibre to the neutral axis in section curvature
$d$	=	Section depth
$E$	=	Elastic modulus
$F_{cr}$	=	Critical stress
$F_u$	=	Ultimate stress
$F_y$	=	Yield stress
$G$	=	Shear modulus
$h$	=	Web depth measured near flange tips
$h_w$	=	Web depth measured near web
$I_y$	=	Minor axis moment of inertia
$J$	=	St. Venant torsional constant
$L$ or $L_b$	=	Length of the unbraced segment
$L_p$	=	Limiting laterally unbraced length for the limit state of yielding
$L_r$	=	Limiting laterally unbraced length for the limit state of inelastic lateral-torsional buckling
$M$	=	Bending moment in a member under specified load

$M_a$	=	Factored moment at one-quarter point of the unbraced segment
$M_{\text{annealed}}$	=	Annealed moment resistance from test results of Fukumoto (1976)
$M_b$	=	Factored moment at mid-point of the unbraced segment
$M_{\text{br}}$	=	Nominal moment capacity for an equivalent braced beam, taken as $M_p$ or $M_y$
$M_c$	=	Factored moment at three-quarter point of the unbraced segment
$M_{\text{cr}}$	=	Theoretical critical elastic moment
$M_E$	=	Critical elastic moment
$M_{\text{FE}}$	=	Maximum moment capacity predicted by finite element analysis
$M_{\text{max}}$	=	Maximum factored moment in the unbraced segment; maximum moment resistance; buckling moment resistance
$M_n$	=	Nominal moment resistance
$M_p$	=	Plastic moment resistance
$M_r$	=	Factored moment resistance
$M_{\text{S16}}$	=	Maximum moment resistance predicted by CSA S16-14
$M_u$	=	Critical elastic moment for CSA S16-14
$M_{\text{ultimate}}$	=	Maximum moment resistance
$M_{\text{as-welded}}$	=	As-welded moment resistance from test results of Fukumoto (1976)
$M_y$	=	Yield moment resistance
$n$	=	System factor
$P$	=	Applied load
$P_{\text{max}}$	=	Maximum applied load; buckling load
$q$	=	Magnitude of uniformly distributed load
$S$	=	Standard deviation
$S_x$	=	Elastic section modulus about the major axis
$t$	=	Flange thickness
$W$	=	Parameter representing ratio of warping torsion stiffness to St. Venant torsion stiffness
$w$	=	Web thickness
$y$	=	Distance from mid-height to point of load application
$Z_x$	=	Plastic section modulus about the major axis

$\alpha$	=	Shape factor for major-axis bending
$\beta$	=	Reliability index
$\delta_h$	=	Lateral displacement; lateral displacement of top flange at buckling
$\delta_r$	=	Reduction factor for stability effects
$\delta_v$	=	Vertical displacement
$\delta_z$	=	Longitudinal displacement
$\varepsilon$	=	Longitudinal strain
$\varepsilon_{\text{exterior}}$	=	Longitudinal strain at exterior face of compression (top) flange
$\varepsilon_{\text{interior}}$	=	Longitudinal strain at interior face of compression (top) flange
$\theta_z$	=	Cross-section rotation (twist)
$\bar{\lambda}$	=	Modified slenderness ratio
$\sigma$	=	Longitudinal stress
$\sigma_{\text{crD}}$	=	Theoretical critical buckling stress for elastic lateral–torsional buckling
$\sigma_D$	=	Limiting lateral–torsional buckling stress at the extreme cross-section fibre
$\sigma_{yf}$	=	Flange yield stress
$\phi$	=	Resistance factor in CSA S16-14
$\phi_b$	=	Resistance factor for flexure in AISC 360-16
$\phi_c$	=	Section curvature
$\omega_2$	=	Moment gradient factor for CSA S16-14
$\omega_2^*$	=	Modified moment gradient factor to account for load height

# 1 INTRODUCTION

## 1.1 Background

Lateral–torsional buckling (LTB) is a potential failure mode of steel beams under flexural bending. It is characterised by in-plane flexural displacement followed by simultaneous lateral movement and cross-section rotation, resulting in a beam with a twisted appearance. LTB is a stability-related failure that occurs in unbraced or insufficiently braced beams wherein members have higher stiffness about the axis of bending (major principal axis) than about the minor principal axis. Consequently, members may not be able to reach their full cross-sectional capacity before LTB occurs. At the onset of LTB failure, load capacity remains relatively constant as the member displaces laterally and twists, but eventually the substantial deformation and potentially significant yielding result in decreases in capacity and the member’s structural usefulness is terminated (Ziemian 2010). As it is unrealistic to use continuously braced members in all cases, LTB is a limit state commonly considered in the design of beams and girders for both building and bridge applications.

In Canada, LTB resistance of steel beams is determined in accordance with design standards CSA S16-14 (CSA 2014a) and CSA S6-14 (CSA 2014b) for buildings and bridges, respectively. LTB is one limit state considered in beam design, which can be represented as a curve of moment capacity versus unbraced length that identifies three distinct regions of bending resistance (local buckling having been precluded): (1) elastic LTB, occurring primarily in slender beams with long unbraced lengths; (2) inelastic LTB, when partial cross-section yielding occurs prior to instability; and (3) beams with sufficiently short unbraced lengths such that cross-section capacity is attained before LTB can occur. As cross-section capacity is easily calculated, the attention turns to representative design equations for elastic and inelastic LTB. In CSA S16-14, these equations are based on a closed-form solution of elastic LTB resistance (Timoshenko and Gere 1961), which is then reduced to account for factors such as moment gradient, initial geometric imperfections, residual stress, and yielding (Ziemian 2010).

## 1.2 Statement of Research Problem

Currently, CSA S16-14 prescribes a unified curve for determining LTB resistance that applies to both rolled and welded sections. However, recent analytical studies (MacPhedran and Grondin 2011; Kabir and Bhowmick 2016) have indicated that the existing design equations may be unconservative for welded members, particularly in the inelastic LTB region. The concern arises primarily from assumptions regarding residual stresses, which are inherent stresses induced in steel members during their production process that are known to have a significant impact on LTB capacity (Ziemian 2010). While residual stresses exist in both rolled and welded sections, the latter's welded nature produces distinct residual stress distributions that may increase their susceptibility to LTB. Though a need to change the existing provisions has been suggested (MacPhedran and Grondin 2011), the recent studies have also been primarily numerical and mostly use physical testing data from Japan in the 1960s to 1980s (Greiner and Kaim 2001). Since then, manufacturing and welding processes have been significantly updated, which is likely to have a considerable effect on LTB resistance. The lack of recent test data means these fabrication changes have not been captured in the experimental results and, more broadly, the existing database of tests may not be representative of modern welded steel girders in North America. Given the ubiquity of welded members in steel structures, an improved understanding of their LTB resistance by means of a new physical testing programme is necessary.

## 1.3 Objectives and Scope

The principal objective of the research is to contribute a new experimental study on the LTB resistance of steel welded girders that encompasses representative residual stress distributions, which will improve understanding of LTB behaviour in modern welded girders. Moreover, the test results can be used to evaluate the adequacy of the CSA S16-14 provisions for predicting the LTB resistance of welded members.

The experimental programme includes LTB tests of 11 large-scale welded girders of nine unique cross-sections produced with conventional modern manufacturing and welding processes in a steel fabrication shop with extensive experience in fabricating welded bridge girders. The research

considers only girders in the inelastic LTB range, as this is the region where residual stresses are most impactful. The successful completion of the research programme requires:

1. identifying major influential parameters in LTB resistance;
2. developing a test matrix that considers the identified influential parameters;
3. creating pre-test finite element models to provide preliminary predictions of girder displacements, rotations, and forces;
4. developing an experimental test set-up that accommodates the full range of movement expected during LTB;
5. performing large-scale LTB girder tests;
6. analysing the obtained resistance and displacement behaviour; and
7. comparing experimental results to CSA S16-14 to evaluate the adequacy of the Canadian steel design standard.

## 1.4 Organisation of Report

This report is organised into six chapters, followed by five appendices with supplementary information. Chapter 2 presents a literature review covering existing design methods for determining LTB resistance, factors influencing LTB resistance, and relevant experimental and analytical research on LTB. Test girder characteristics are discussed in Chapter 3, which outlines test specimen matrix development, as well as measured material and geometric properties. Chapter 4 details the experimental programme—from the preliminary pre-test finite element modelling to the test set-up, instrumentation, and test procedure. Test results are reported in Chapter 5; general test observations, along with discussions on girder capacity and displacement behaviour, are included. The effect of identified influential parameters on experimental LTB resistance is examined and a comparison with predicted resistances from CSA S16-14 is conducted. Chapter 6 presents conclusions drawn from this study and recommends areas for further research. Appendix A contains engineering drawings for the test specimens while Appendix B includes distributions of the measured initial geometric imperfections. Stress–strain curves from material testing are provided in Appendix C. Load–displacement curves from the numerical analysis and physical testing can be found in Appendices D and E, respectively.

## 2 LITERATURE REVIEW

This chapter reviews relevant studies and provides important context for the research programme. Several design standards and their methods of determining lateral–torsional buckling (LTB) resistance are discussed, factors affecting LTB are explained, and both numerical and experimental research pertaining to LTB is presented.

### 2.1 Design of Laterally Unsupported Girders

#### 2.1.1 Classic Lateral–Torsional Buckling Solution

To understand general LTB behaviour, it is helpful to start with a method for determining the theoretical elastic LTB moment, as it forms the basis for determining nominal flexural resistance. For the simplest case of simply-supported doubly-symmetric members under uniform moment, a closed-form solution exists for the governing differential equations (Timoshenko and Gere 1961). The critical elastic buckling moment,  $M_{cr}$ , which corresponds to the bifurcation from in-plane bending to out-of-plane bending and twisting, can be calculated as:

$$M_{cr} = \frac{\pi}{L} \sqrt{EI_y GJ + \left(\frac{\pi E}{L}\right)^2 I_y C_w} \quad 2-1$$

where  $L$  is the length of the unbraced segment of the member,  $E$  is the elastic modulus,  $I_y$  is the minor axis moment of inertia,  $G$  is the shear modulus,  $J$  is the St. Venant torsional constant, and  $C_w$  is the warping torsional constant.

While LTB design equations vary from standard to standard, they generally follow a similar approach for determining flexural bending resistance. The theoretical elastic buckling solution is used as a starting point, and various modifications—to account for parameters such as moment gradient, initial geometric imperfections, residual stress, and extent of yielding—are then applied to determine the nominal bending resistance. Additionally, there is variability and uncertainty in these factors, which design standards account for with different methods and weighting in the calculation of nominal resistance and with resistance factors.

### 2.1.2 CSA S16-14 (2014)

The Canadian steel design standard, CSA S16-14 (CSA 2014a), requires the determination of LTB resistance as part of a beam design protocol. Separate but related relationships, as defined in Equations 2-2 to 2-6, form the beam design curve for Class 1/2 sections that identifies three ranges of behaviour: elastic buckling, inelastic buckling, and cross-sectional capacity.

$$\text{If } M_u > 0.67M_p: \quad M_r = 1.15\phi M_p \left[ 1 - \frac{0.28M_p}{M_u} \right] \leq \phi M_p \quad 2-2$$

$$\text{If } M_u \leq 0.67M_p: \quad M_r = \phi M_u \quad 2-3$$

$$M_p = Z_x F_y \quad 2-4$$

$$M_u = \omega_2 M_{cr} = \frac{\omega_2 \pi}{L} \sqrt{EI_y GJ + \left( \frac{\pi E}{L} \right)^2 I_y C_w} \quad 2-5$$

$$\omega_2 = \frac{4M_{\max}}{\sqrt{M_{\max}^2 + 4M_a^2 + 7M_b^2 + 4M_c^2}} \leq 2.5 \quad 2-6$$

where  $M_u$  is the critical elastic moment of the unbraced segment,  $M_p$  is the plastic moment capacity of the section,  $M_r$  is the factored moment resistance,  $\phi$  is the resistance factor,  $Z_x$  is the plastic section modulus about the major axis,  $F_y$  is the material yield stress,  $\omega_2$  is the moment gradient coefficient,  $M_{\max}$  is the maximum factored moment in the unbraced segment, and  $M_a$ ,  $M_b$ ,  $M_c$  are the factored moments at the one-quarter point, mid-point, and three-quarter point of the unbraced segment, respectively.

A conceptual graph, shown in Figure 2-1, summarises the beam design curve. For slender beams, elastic LTB (Equation 2-5) governs and is calculated by multiplying the theoretical elastic buckling moment by a moment gradient factor and resistance factor. Stocky beams can reach their cross-sectional strength before LTB occurs and thus their factored moment capacity is equal to the resistance factor multiplied by their plastic moment (Equation 2-4). For beams that fall between these two extremes, and are therefore governed by inelastic LTB, there is an empirical transitional

curve (Equation 2-2), which was developed from Baker and Kennedy's (1984) statistical analysis of Dibley's (1969) tests on beams with rolled I-sections. It is deemed applicable when a member's elastic LTB resistance is greater than  $0.67M_p$ , but it must not exceed  $M_p$ . For Class 3 sections, the yield moment resistance,  $M_y$ , replaces  $M_p$  in Equation 2-2 and Equation 2-3. Therefore, the factored cross-sectional capacity is limited to the resistance factor multiplied by the yield moment,  $M_y = S_x F_y$ , where  $S_x$  is the elastic section modulus about the major axis.

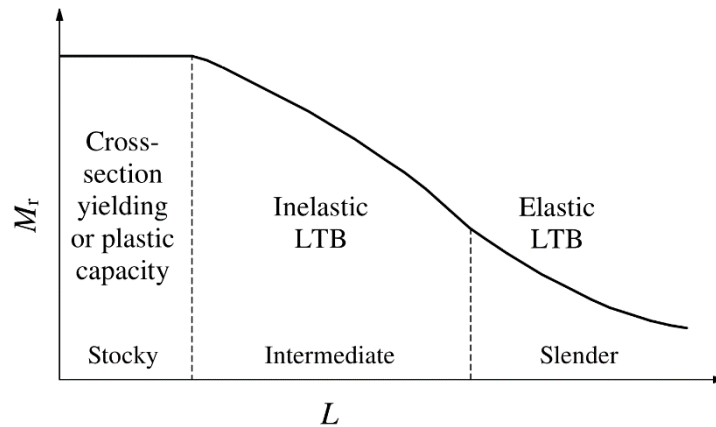


Figure 2-1: Conceptual beam design curve

### 2.1.3 CSA S6-14 (2014)

The Canadian highway bridge design code, CSA S6-14 (CSA 2014b), uses the same equations as CSA S16-14 to determine LTB resistance for steel sections. Though the proposed research does not explicitly involve bridge girders, the findings are applicable to CSA S6-14 also.

### 2.1.4 ANSI/AISC 360-16 (2016)

The American Specification for Structural Steel Buildings, ANSI/AISC 360-16 (AISC 2016), identifies three regions of behaviour that are analogous to those of CSA S16-14, but they are delineated based on the length of the unbraced segment instead of the critical moment value. The provisions for doubly-symmetric compact I-shaped members bent about their major axis are shown in Equations 2-7 to 2-11.

$$M_r = \phi_b M_n \quad 2-7$$

$$\text{When } L_b \leq L_p: \quad M_n = M_p = F_y Z_x \quad 2-8$$

$$\text{When } L_p < L_b \leq L_r: \quad M_n = C_b \left[ M_p - (M_p - 0.7F_y S_x) \frac{L_b - L_p}{L_r - L_p} \right] \leq M_p \quad 2-9$$

$$\text{When } L_b > L_r: \quad M_n = F_{cr} S_x \leq M_p \quad 2-10$$

$$C_b = \frac{12.5M_{\max}}{2.5M_{\max} + 3M_a + 4M_b + 3M_c} \quad 2-11$$

where  $\phi_b$  is the resistance factor for flexure,  $M_n$  is the nominal flexural strength,  $L_b$  is the unbraced length,  $L_p$  is the limiting laterally unbraced length for the limit state of yielding,  $L_r$  is the limiting laterally unbraced length for the limit state of inelastic LTB,  $C_b$  is the moment gradient factor and its constituent parameters are defined as for Equation 2-6, and  $F_{cr}$  is the critical stress,.

The AISC 360-16 elastic LTB resistance (Equation 2-10) can be rewritten as  $M_n = C_b M_u$ , which is nearly identical to the Canadian provision, the only difference being the definition of the moment gradient factor. Though, it should be noted, the AISC 360-16 commentary permits the use of CSA S16-14's moment gradient factor definition (Equation 2-6), which would effectively make the elastic LTB resistance calculation identical between the two standards.

## 2.2 Factors Affecting Lateral–Torsional Buckling

Factors affecting LTB that are pertinent to this research project are discussed in this section, and previous research concerning their effect on LTB is summarised.

### 2.2.1 Residual Stress

Residual stresses are inherent in unloaded steel sections and are attributed to various stress-inducing processes during fabrication, such as straightening, flame-cutting, welding, and cooling after rolling (Ziemian 2010). Flame-cutting (also called oxygen, oxy-fuel, or oxy-flame cutting) introduces intense heat near the flame-cut edge, and the resulting residual stress distribution may include large tensile spikes at the plate tips (Alpsten and Tall 1970; McFalls and Tall 1970).

Residual stresses vary depending on the cutting method; for example, in contrast to flame-cutting, universal-mill plates show largely compressive residual stresses at the plate edge (Alpsten and Tall 1970), as shown in Figure 2-2. Other cutting methods, such as waterjet and plasma-cutting, also create different distributions.

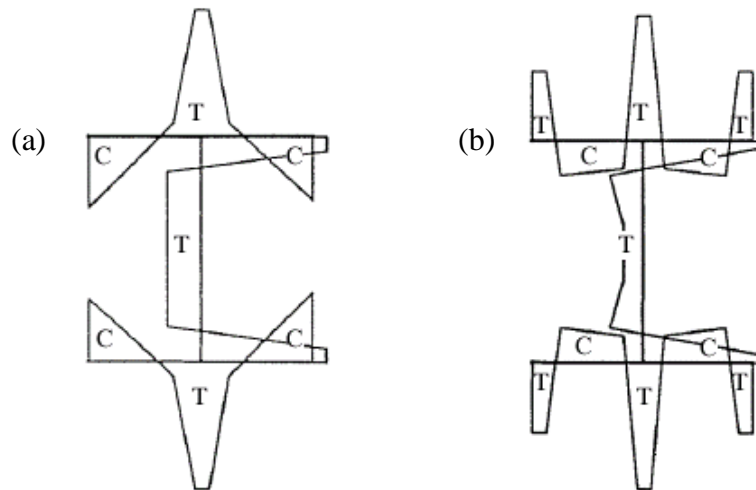


Figure 2-2: Representative residual stress pattern of (a) universal-mill and (b) flame-cut plates, where ‘C’ is compression and ‘T’ is tension (adapted from Chernenko and Kennedy 1991)

In welded sections, the welding process considerably alters the residual stresses in the plate. Like flame-cutting, welding creates a narrow region of intense heat input. This results in large tensile residual stresses in the area surrounding the weld with magnitudes that can equal the yield strength of the weld metal, which is typically larger than that of the parent metal (Tall 1966). To satisfy equilibrium, these large tension spikes must be balanced by large spikes and/or large regions of compressive residual stress in the remaining portions of the plate.

Schematic residual stress patterns of rolled and welded I-sections (the latter with plates cut using a method of relatively low heat input) are shown in Figure 2-3. In both sections, the presence of compressive residual stresses at the flange tips can cause yielding to occur in the compression flange before the theoretical yield strength is attained. However, the large flat region of compressive stress in the welded section will lead to a sudden loss of stiffness and therefore a rapid decrease of flexural bending capacity. In the case of flame-cut plates, the tensile stresses at the

flange tips have the beneficial effect of postponing yielding in that region, which helps with lateral stability. It follows that, for sections of similar geometry, the flame-cut sections tend to have larger buckling capacity than those with less favourable distributions, such as universal-mill plates (Subramanian and White 2017).

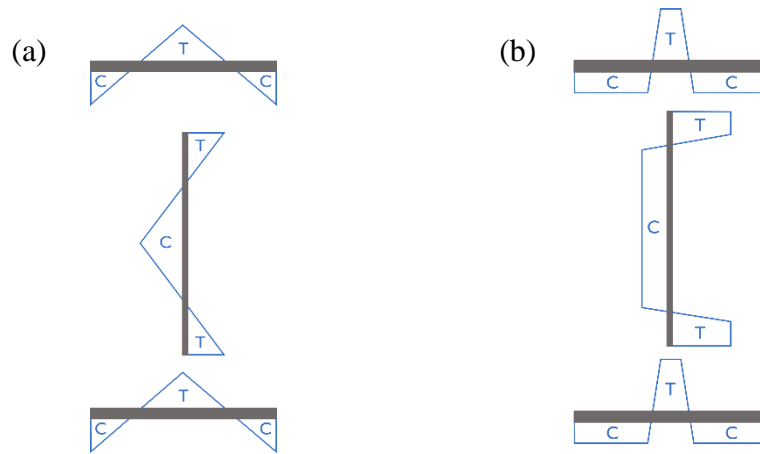


Figure 2-3: Schematic residual stress pattern of (a) rolled section and (b) welded section, where ‘C’ is compression and ‘T’ is tension (Unsworth et al. 2019)

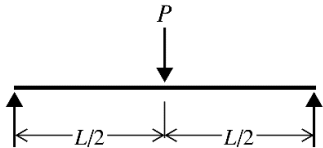
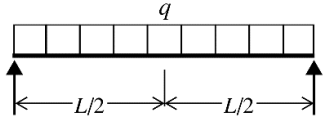
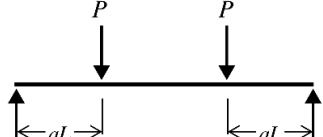
### 2.2.2 Initial Geometric Imperfections

Geometric imperfections in girders can arise from the fabrication process and are known to have a significant effect on LTB capacity. For example, increasing initial twist and lateral out-of-straightness of the compression flange (sweep) have both been shown to reduce LTB capacity, though sweep is thought to have the stronger influence (Boissonnade and Somja 2012). The Canadian standards for welded steel construction and structural quality steel, CSA W59-13 (CSA 2013a) and CSA G40.20-13 (CSA 2013b), respectively, both specify a limit of  $L/1000$  for permissible flange sweep; the American structural welding code (AWS 2015) specifies the same. While numerical simulations of LTB often use the permissible limit of  $L/1000$  (Boissonnade and Somja 2014; Kabir and Bhowmick 2018), Subramanian and White (2017) have suggested that this value is too severe, as previous measurements of sweep in experimental studies have been far lower (e.g.,  $L/2000$  by Essa and Kennedy (1993),  $L/3600$  by Dux and Kitipornchai (1983) and  $L/12,500$  by Fukumoto et al. (1980)).

### 2.2.3 Load Height

The vertical position of the applied load affects a member's LTB resistance. For doubly-symmetric sections, shear centre loading is assumed in CSA S16-14's general LTB provisions. If a section is loaded through its bottom flange instead, there will be a restoring torque that creates a stabilising effect (higher LTB resistance). Conversely, top flange loading generates an amplifying torque that has a destabilising effect (lower LTB resistance). In CSA S16-14, loading above the shear centre is accounted for approximately by using  $\omega_2 = 1.0$  for determining  $M_u$  and an effective length of  $1.2L$  for pinned-ended members and  $1.4L$  for all other cases of in-plane rotational restraint (Clause 13.6). Alternatively, the *SSRC Guide* (Galambos 1998) proposed a method—based on the work of Nethercot and Rockey (1971)—to account for the change in LTB resistance due to load height for three transverse loading conditions, as summarised in Table 2-1, Equation 2-12, and Equation 2-13. LTB resistance calculations using these equations were found to match closely with accurate numerical solutions, with a maximum error of 5% (Nethercot and Rockey 1971). Helwig et al. (1997) then determined that the effects of load height can be approximated by taking  $B = 1.4$ , as shown in Equation 2-14.

Table 2-1: Load height adjustment coefficients by Nethercot and Rockey (1971)

Loading	A	B
	1.35	$1 - 0.180W^2 + 0.649W$
	1.12	$1 - 0.154W^2 + 0.535W$
	$1 + a^2$	$1 - 0.465W^2a + 1.636Wa$

$$\omega_2^* = AB^{2y/d} \quad 2-12$$

$$W = \frac{\pi}{L} \sqrt{\frac{EC_w}{GJ}} \quad 2-13$$

$$\omega_2^* = \omega_2(1.4^{2y/d}) \quad 2-14$$

where  $\omega_2^*$  is the modified moment gradient factor to account for load height,  $d$  is the beam depth and  $y$  is the distance from mid-height to the point of load application (negative for above mid-height loading and positive for below the mid-height).

## 2.3 Previous Physical Testing of Rolled and Welded Laterally Unsupported Girders

This section presents an overview of the previous physical testing programmes that investigate LTB behaviour in rolled and welded members. Relevant observations and conclusions regarding the effect of identified influential parameters on LTB resistance are reported.

### 2.3.1 Dibley (1969)

The introduction of new, higher strength steel into the British Standard Specification for structural steels prompted a need to investigate the adequacy of the bending clauses. Dibley (1969) reviewed the existing theories for LTB design and extended their application to higher yield strength steels. To verify the design theories, he conducted 30 tests on high strength, rolled, universal beams under four-point bending (to create uniform moment in the unsupported centre segment). Members were simply-supported in vertical and lateral bending, with twist prevented, but warping allowed, at the supports. Five unique cross-sections were considered; sections were Class 2 or Class 3 and were predicted to fail in elastic LTB, inelastic LTB, or attain their cross-sectional capacity. Actual cross-sectional dimensions were determined by taking the mean of four readings of flange thickness, flange width, and section depth along the member; web thickness was measured at the top, centre, and bottom at both ends of the member. Approximate initial lateral out-of-straightness measurements were completed, but a measurable imperfection was found in two cases only.

The direction of lateral movement and torsional rotation was highly variable and, in some cases, members changed direction of movement during the test. Residual stresses were measured and were found to be of similar magnitudes to those in low strength steel, which suggests residual stresses may have less effect in high strength steel than in low strength steel. Furthermore, Dibley (1969) concluded that the British Specifications adequately predicted the bending strength of high strength steel beams. His test results were later used by Baker and Kennedy (1984) to calibrate resistance factors in the Canadian provisions for laterally unsupported steel beams.

### 2.3.2 *Dux and Kitipornchai (1983)*

To investigate the effect of moment gradient on inelastic LTB resistance, Dux and Kitipornchai (1983) conducted tests on nine beams in three groups of three. The three groups corresponded to three different moment distributions: (1) concentrated load at mid-span, (2) two equal concentrated loads applied at  $L/4$  from the ends, and (3) two unequal concentrated loads applied at  $L/4$  from the ends; within each group, the beams were of different lengths. Loads were applied through the top flange, but the beams were braced against lateral movement and twist at the load points (as well as the end supports). The loading configuration of (2) and (3) created a critical central segment, where inelastic LTB would occur, and restraining end segments. Residual stresses, as well as initial sweep at the shear centre and initial twist, were measured; the maximum geometric imperfection values were  $L/1250$  and  $0.003$  rad, respectively.

During testing, the attainment of maximum load capacity was followed by load shedding and large deformations, signalling a rapid loss of strength. Results of the inelastic LTB tests showed that buckling capacity was a function of moment gradient. The beams were tested under less severe moment gradients and were able to sustain higher moments compared to Dibley's (1969) test specimens, which involved stockier beams but were tested under a uniform moment demand. However, the beneficial effect of restraining end segments was not discussed.

### 2.3.3 *Wong-Chung and Kitipornchai (1987)*

Wong-Chung and Kitipornchai (1987) used a similar set-up to that of Dux and Kitipornchai (1983); they tested 11 rolled beams under two equal concentrated loads at the outer quarter-points

and varied the partial bracing at mid-span—members were either unbraced, laterally braced at the bottom flange, laterally braced at the shear centre, or rotationally braced at the top and bottom flanges. Initial sweep and twist were measured and found to meet the Australian steel structures specification, AS 4100-1998 (Standards Australia 1998). Post-buckling behaviour was not recorded. Results indicated that bottom (tension) flange lateral bracing was ineffective, as it produced similar capacities to those of the unbraced beams. In contrast, lateral bracing at the shear centre was found to be equally effective as rotational bracing.

#### 2.3.4 Fukumoto (1976)

Fukumoto (1976) performed tests on 36 welded beams to investigate their LTB resistance. Two steel grades were considered: SM 50 and quenched and tempered HT 80. As summarised in Table 2-2, several test specimens were annealed to relieve welding residual stresses. Members were laterally and torsionally restrained at the end supports and were loaded under either uniform moment or a moment gradient. Initial lateral out-of-straightness was measured and ranged from  $L/4100$  to  $L/940$ . Residual stress measurements were not taken.

Using the experimental ultimate moments, the effect of residual stress on LTB resistance was examined by comparing annealed and as-weld beam capacities of the same cross-sections. Taking the ratio  $M_{\text{annealed}}/M_{\text{as-welded}}$ , Fukumoto (1976) concluded that welding residual stress distributions reduced the LTB capacity of SM 50 and HT 80 beams by 11% and 6%, respectively. Similar to Dibley’s (1969) findings, this suggests that the effect of residual stress on LTB decreases with higher yield strength steels.

Table 2-2: Summary of Fukumoto (1976) test girders

Steel Grade	Nominal Yield Stress (MPa)	Number of Annealed Beams	Number of As-welded Beams
SM 50	314	9	12
HT 80	686	3	12

### 2.3.5 Fukumoto and Kubo (1977)

A review of existing LTB tests on laterally supported and unsupported beams and girders was conducted by Fukumoto and Kubo (1977), with an emphasis on the Japanese contributions in this area. A total of 159 rolled and 116 welded specimens, including 28 plate girders, were reviewed. They were further divided into three ranges by a modified slenderness ratio,  $\bar{\lambda} = \sqrt{M_p/M_E}$ , as shown in Table 2-3, where  $M_E$  is the critical elastic moment. A comparison of rolled and welded tests for  $\bar{\lambda} = 0.9 - 1.4$  indicated larger scatter for welded beams than for rolled beams. Furthermore, the mean ultimate strength of welded beams was found to be lower than that of rolled beams of equivalent cross-section.

Table 2-3: Number of reviewed experiments by Fukumoto and Kubo (1977)

	$\bar{\lambda} = 0 - 0.4$ (Plastic Range)	$\bar{\lambda} = 0.4 - 1.4$ (Inelastic Range)	$\bar{\lambda} > 1.4$ (Elastic Range)
Rolled Beams	36	95	28
Welded Beams	26	89	1

### 2.3.6 Fukumoto et al. (1980)

An experimental study on laterally unsupported rolled beams was conducted by Fukumoto et al. (1980) to provide reliable statistical data on residual stresses, initial imperfections, and LTB strength under nominally identical support conditions, load conditions, and member sizes. Degrees of correspondence between various beam parameters and the obtained buckling strengths were then studied. The test programme considered 25 beams of 7 m length with nominally identical cross-sections. The beams were then cut into three different span lengths of 2.6 m, 2.0 m, and 1.5 m (totalling 75 test specimens), which were named series A, B, and C, respectively; the remaining length was used for residual stress measurements and tension coupon tests. Beams were simply supported and tested under a concentrated load applied vertically at mid-span to the compression flange using a Lehigh-type gravitational load simulator; fork supports at either end prevented twist but allowed warping.

Statistical data of geometrical and material properties and of ultimate strengths were recorded; the pertinent observations are herein summarised. From the tension coupon tests, mean values of yield stress were found to be greater than the minimum specified value of 235 MPa by 7.1% in the flange and by 22.3% in the web. Residual stresses were measured using the sectioning method; the mean compressive residual stress at the flange tips was  $0.08F_y$  (using the measured yield stress of the flange) and a considerably large coefficient of variation of 0.438 was observed. Initial out-of-straightness about the major and minor axes and angle of rotation were measured for all 75 test specimens at five equally spaced points along the beam length, though the imperfections were small in all cases. Table 2-4 summarises the imperfection measurements, where  $S$  is standard deviation; to present the data in an understandable and comparable format, the denominators are rounded. Of the recorded beam parameters and ultimate strengths, initial geometric imperfections exhibited the largest coefficients of variation. The effect of top flange loading was not considered.

Table 2-4: Summary of imperfection measurements by Fukumoto et al. (1980)

	Initial Out-of-straightness About Major Axis	Initial Out-of-straightness About Minor Axis	Angle of rotation (rad)
Mean	$L/12,000$	$L/12,500$	$1/760$
Mean + $2S$	$L/5000$	$L/5000$	$1/250$

### 2.3.7 Fukumoto and Itoh (1981)

As a continuation of the laterally unsupported beam test series, Fukumoto and Itoh (1981) conducted experimental tests on welded beams that were geometrically similar to the rolled beams tested by Fukumoto et al. (1980). A similar statistical evaluation was performed, wherein the variations in material and geometric imperfections were obtained and the degree of correlation with the scatter in ultimate strength was examined. The test programme considered 34 welded beams of 5.02 m length with nominally identical cross-sections. Beams were then cut into 1.8 m (D series) and 2.6 m (E series) span for a total of 68 specimens, with the remaining length used for residual stress measurements and tension coupon tests. The same loading and support conditions as Fukumoto et al. (1980) were used.

Mean values of yield stress were greater than the minimum specified value of 235 MPa by 24.5% in flange and by 43.5% in web. The mean non-dimensionalised initial out-of-straightness at mid-span about the major axis, minor axis, and angle of rotation were  $0.125 (0.084) \times 10^{-3}$ ,  $0.296 (0.080) \times 10^{-3}$ , and  $0.504 (0.138) \times 10^{-3}$ , respectively, where the values in parentheses refer to the associated measurements for rolled beams (Fukumoto et al. 1980).

A modified non-dimensional residual stress parameter was defined and it was observed that welded girders had larger compressive residual stresses and greater variability in compression regions than rolled beams. Further statistical evaluation was conducted to analyse the effects of the defined residual stress parameter and initial lateral out-of-straightness on ultimate strength in series B (rolled) and D (welded), as they had similar nominal slenderness. The obtained buckling load,  $P_{\max}$ , was converted to a non-dimensional form,  $M_{\max}/M_p$ , where  $M_{\max}$  was the ultimate moment obtained during the test. The mean  $M_{\max}/M_p$  ratios for series B and D were 0.823 and 0.790, respectively. Low correlation between residual stress and  $M_{\max}/M_p$  was found for both series; however, the mean residual stress parameter was 1.82 times larger in the welded series than in the rolled, which may have attributed to the decreased mean  $M_{\max}/M_p$  for the welded series. Though the correlation coefficients for lateral out-of-straightness and  $M_{\max}/M_p$  were nearly zero for both series (i.e., very little correlation), the mean lateral out-of-straightness in welded beams was 4.38 times larger than in rolled and may have reduced the mean  $M_{\max}/M_p$ . For clarity, a lack of correlation does not mean there is no effect; rather, it signifies the relationship between the parameters is unclear.

## 2.4 Previous Analytical Studies of Rolled and Welded Laterally Unsupported Girders

This section summarises analytical studies of LTB behaviour in rolled and welded members. These studies comprise alternative equations to the accepted design provisions for laterally unsupported members, as well as numerical models that investigate the effect of influential parameters on LTB resistance.

#### 2.4.1 European Convention for Constructional Steelwork (1976)

An LTB work group with participating members from the Column Research Committee of Japan, Structural Stability Research Council, and European Convention for Constructional Steelwork (ECCS) Committee on Stability published recommendations of their research on laterally supported and unsupported beams in a manual-type Introductory Report (ECCS 1977). In the recommendations, they proposed a design equation for LTB of doubly-symmetric sections, as follows:

$$\sigma_D \leq \delta_r \alpha F_y \quad 2-15$$

$$\delta_r = \left(1 + \bar{\lambda}^{2n}\right)^{-1/n} \quad 2-16$$

$$\bar{\lambda} = \sqrt{\frac{\alpha F_y}{\sigma_{crD}}} \quad 2-17$$

where  $\sigma_D$  is the limiting LTB stress at the extreme cross-section fibre  $\delta_r$  is the reduction factor for stability effects,  $\alpha$  is the shape factor for major-axis bending,  $\bar{\lambda}$  is the modified slenderness ratio,  $\sigma_{crD}$  is the theoretical critical buckling stress for elastic LTB, and  $n$  is the “system” factor.

The value of  $n$  was deemed critical and is dependent on cross-section, type of loading, form and amount of eccentricity of the loading, grade of steel, mode of load application, and fabrication procedure. Though  $n$  was not meant to be constant, a value of 2.5 was recommended to correspond to a mean value rather than a lower bound, as other favourable effects were neglected in the formulation of the proposed equation. However, Fukumoto and Kubo (1977) conducted a review of LTB tests on rolled and welded beams and recommended that a value of 2.0 be used for welded beams as they showed larger scatter and lower lateral buckling capacity than rolled beams.

#### 2.4.2 MacPhedran and Grondin (2011)

A simplified one-part equation to calculate the strength of laterally unbraced beams was proposed by MacPhedran and Grondin (2011) as a replacement to the existing three-part curve in CSA

S16-09 (CSA 2009); the same curve is prescribed in CSA S16-14. Their proposed equation mirrors the general form of the Canadian steel column design curve, as it similarly uses a modified slenderness ratio to calculate resistance. In this case, the modified slenderness ratio ( $\bar{\lambda}$ ) was derived from the braced (maximum) moment capacity and unbraced (elastic buckling) capacity; the complete proposed beam equation for nominal moment capacity is as follows:

$$M_n = M_{br} \left( 1 + \bar{\lambda}^{2n} \right)^{-1/n}, \quad \bar{\lambda} = \sqrt{M_{br}/M_u} \quad 2-18$$

where  $M_{br}$  is the nominal moment capacity for an equivalent braced beam. This generalised, nominal equation can be rewritten for Class 1/2 sections as well as Class 3 sections, as shown in Equation 2-19 and Equation 2-20.

$$\text{Class 1/2: } M_r = \phi M_p \left( 1 + \bar{\lambda}^{2n} \right)^{-1/n}, \quad \text{where } \bar{\lambda} = \sqrt{M_p/M_u} \quad 2-19$$

$$\text{Class 3: } M_r = \phi M_y \left( 1 + \bar{\lambda}^{2n} \right)^{-1/n}, \quad \text{where } \bar{\lambda} = \sqrt{M_y/M_u} \quad 2-20$$

The generalised Equation 2-18 proposed by MacPhedran and Grondin (2011) is an alternative form of the ECCS recommended Equation 2-15. In this research, MacPhedran and Grondin (2011) calibrated the system factor  $n$  and conducted a reliability analysis to determine an appropriate resistance factor. Test data gathered by Greiner and Kaim (2001) was used, totalling 144 tests on rolled shapes and 71 tests on welded sections; all sections were Class 1/2. Of these tests, it was observed that welded sections exhibited significantly larger scatter and lower capacity than rolled sections, which indicates a need to differentiate between the two types. Using coefficient of variation (CV) as a beam curve calibration parameter, the  $n$  values that minimised CV for rolled and welded sections were 3.1 and 1.9, respectively, for the data used. This is a notable difference, as the existing Canadian beam design curve does not make a distinction between rolled and welded sections. A comparison of the proposed beam equation (using the calibrated  $n$  values) and the CSA S16-01 (CSA 2001) provisions showed good agreement for rolled shapes, but significant

differences for welded sections, as shown in Figure 2-4. The depicted points in Figure 2-4 are separated into slender and stocky sections, where slender refers to a section depth to flange width ratio ( $d/b$ ) of greater than 2 and stocky indicates  $d/b \leq 2$ .

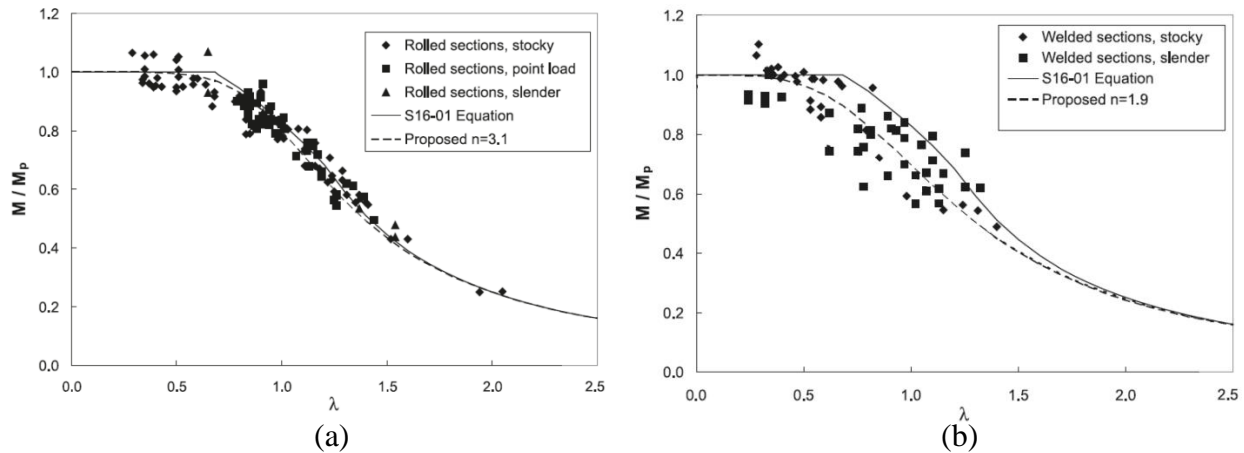


Figure 2-4: Comparison of CSA S16-01 and proposed equation by MacPhedran and Grondin (2011) for (a) rolled and (b) welded sections

In the reliability analysis, MacPhedran and Grondin (2011) considered a range of modified slenderness ratios up to  $\bar{\lambda} = 2.5$ . For four representative  $\bar{\lambda}$  values, the minimum reliability index,  $\beta$ , of the proposed equation using the CSA S16 prescribed resistance factor of 0.9 was 2.63 for rolled sections and 2.70 for welded sections. In comparison, the CSA S16-09 equation resulted in reliability indices of 3.0 for rolled sections and 1.6 for welded sections using a resistance factor of 0.9. To achieve a reliability index of 3.0 for welded sections would require a resistance factor of approximately 0.82 for the CSA S16-09 equation, which suggests it is overestimating the buckling capacity of welded members. A reliability analysis was also done on Class 3 sections, with a limited database of 27 rolled shape tests from White and Jung (2004). For rolled shapes only and  $n = 3.1$ , a resistance factor of 0.92 would give a reliability index of 3.0 or greater for the proposed equation. No comparison was made with the CSA S16-09 equation for Class 3 sections.

#### 2.4.3 Kabir and Bhowmick (2016; 2018)

Following MacPhedran and Grondin's (2011) observations that CSA S16-09 may overestimate the LTB resistance of welded beams, Kabir and Bhowmick (2016; 2018) conducted an extensive finite

element (FE) study on welded wide-flange beams, totalling 256 simulations. Members were modelled in Abaqus (Dassault Systèmes 2014) with simply-supported boundary conditions; lateral displacement and twist were prevented at the ends. The FE analysis consisted of two parts: an eigenvalue buckling analysis was first conducted, then the lowest eigenmode was selected for the initial geometric imperfection pattern, which was used for the subsequent non-linear Riks analysis. The imperfection pattern was scaled to have a maximum lateral out-of-straightness of  $L/1000$  at mid-span. Ten welded Class 1/2 cross-sections were selected for the analysis.

Four residual stress patterns were considered: mill plate type, flame-cut type, Fukumoto and Itoh (1981), and Dux and Kitipornchai (1983). The first two patterns were simplified distributions based on residual stress measurements at Lehigh University (Chernenko and Kennedy 1991), whereas the latter two were measurements from physical testing programmes by the respective researchers. Dux and Kitipornchai's (1983) measurements were on rolled members, but the remaining three residual stress distributions were representative of welded girders. Each of the ten cross-sections was modelled with the four different residual stress patterns. It was found that the two Lehigh patterns consistently resulted in lower LTB resistances; between the two, the flame-cut type residual stress pattern gave slightly higher capacities than the mill plate type, which was attributed to the presence of high tensile stresses at the flange tips. The Fukumoto and Itoh (1981) pattern involved tensile residual stress across the majority of the flange and produced the highest capacities of the four distributions.

Results of the numerical analyses were compared with capacity predictions from CSA S16-14, AISC 360-10 (AISC 2010), Eurocode 3 (CEN 2005), and the proposed MacPhedran and Grondin (2011) equation. Figure 2-5 and Figure 2-6 depict these comparisons assuming the Fukumoto and Itoh (1981) and mill plate residual stress patterns, respectively, where  $M_{ultimate}$  represents the maximum attained moment. Though CSA S16-14 and AISC 360-10 gave good predictions of elastic LTB, they were found to significantly overestimate member resistance in the inelastic LTB range—simulations showed capacities up to 37% lower than the CSA S16-14 predictions. In comparison, Eurocode gave satisfactory predictions in the inelastic LTB range, particularly for the mill plate and flame-cut type residual stress patterns from Lehigh. MacPhedran and Grondin's (2011) equation showed reasonably good predictions for the Fukumoto and Itoh (1981) and Dux

and Kitipornchai (1983) patterns, but slightly overestimated capacity for the Lehigh distributions. Furthermore, a simulation with zero assumed residual stresses and negligible lateral out-of-straightness ( $L/20,000$ ) was found to align closely with CSA S16-14 predictions.

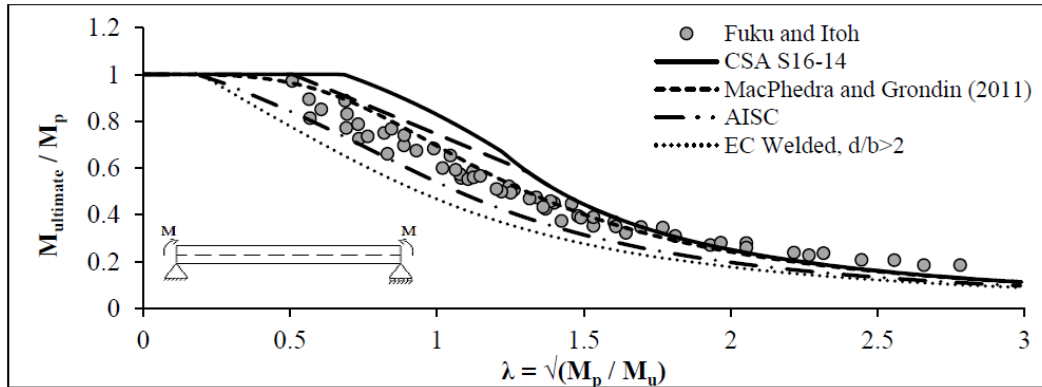


Figure 2-5: Comparison of FE results by Kabir and Bhowmick (2016) using the Fukumoto and Itoh (1981) residual stress pattern

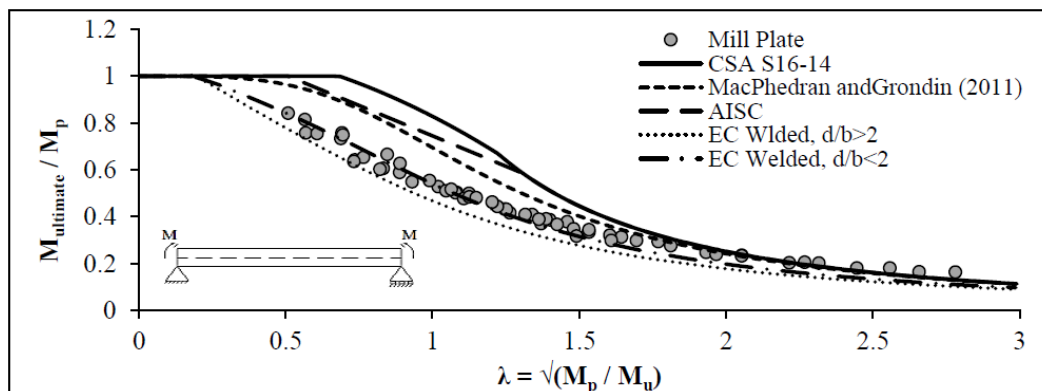


Figure 2-6: Comparison of FE results by Kabir and Bhowmick (2016) using the mill plate residual stress pattern

The effect of load height—top flange, shear centre, and bottom flange loading—was also examined for the case of a concentrated load applied at mid-span and uniformly distributed load. Kabir and Bhowmick (2016) observed that, for top flange loading, CSA S16-14 overestimated member resistance by 17% and 33% for concentrated load and uniform moment, respectively. However, it is important to note that the CSA S16-14 predictions were based on shear centre loading. Kabir and Bhowmick (2016) then employed the Helwig et al. (1997) equation to adjust the code's

moment gradient factor to account for load height effect (Equation 2-14). The adjusted code-calculated moment gradient factors were compared to  $\omega_2$  values from numerical results (back-calculated from the maximum moment). For top flange loading, they found that  $\omega_2$  values from the FE analysis were 36% and 13% larger than those calculated by Equation 2-14 for the cases of concentrated load and uniform moment, respectively, which suggests that Helwig et al. (1997) equation may be overly conservative.

#### 2.4.4 *Subramanian and White (2017)*

Though there is numerical evidence suggesting the Canadian provisions overestimate LTB resistance, researchers have also observed that predictions of LTB capacity from numerical simulations tend to be lower than test results (Subramanian and White 2017; Greiner et al. 2001). This may be attributed to overly-severe residual stresses and imperfections assumed in finite element models. Subramanian and White (2017) attempted to resolve this disconnect by determining the appropriate residual stress patterns and geometric imperfections necessary to achieve good agreement between their numerical model and existing experimental data. They also evaluated the adequacy of the AISC 360-10 and AASHTO (2015) specifications for predicting flexural resistance; both are based on unified provisions by White (2008) that use approximations to quantify moment gradient and end restraint, which may no longer be necessary with the increased use of more rigorous computer-based design calculations.

Six sets of existing experimental test results were used for the numerical simulations—four sets of rolled sections and two sets of welded sections, for a total of 21 and 14 tests, respectively. All tests were expected to fail in inelastic LTB. The Best-Fit Prawel (Kim 2010) residual stress pattern (initially developed for shear-cut welded I-sections) was used to represent welded members, while the Galambos and Ketter (1959) residual stress pattern was chosen for rolled sections. Four values of initial geometric lateral out-of-straightness were analysed:  $L/1000$ ,  $L/2000$ ,  $L/4000$ , and  $L/8000$ . A comparison of the maximum moments from experimental results and simulations showed that an imperfection value of  $L/2000$  and one-half the Best-Fit Prawel residual stress pattern produced test-to-predicted ratios closest to 1.00.

Further FE simulations were conducted on two rolled and two welded sections to examine the sensitivity of each cross-section's LTB resistance to various residual stress patterns and initial geometric imperfections. Five residual stress distributions were considered (three representative of rolled; two of welded); for imperfections, the previous four lateral out-of-straightness values and the AWS (2010) specifications for flange tilt and web out-of-flatness were used. All members were modelled as simply-supported with lateral displacement and twist restrained at the ends and loaded under constant moment. Results of the FE analysis indicated that a flange sweep of  $L/2000$ , one-half the AWS tolerances for flange tilt and web out-of-flatness, and one-half Best-Fit Prawel residual stress were reasonable parameters to use for LTB modelling of plate girders. Comparison of FE results to the AISC 360-10 and AASHTO equations showed good agreement in the elastic LTB range. However, at the transition from inelastic LTB to plastic capacity, the specifications were unconservative by up to 13%, which indicates a need to lower the strength curves within the inelastic range.

## 2.5 Summary

While LTB has been studied since the mid-1900s, there remains concerns in the adequacy of North American specifications to predict inelastic LTB resistance accurately in laterally unsupported members. FE studies have indicated that CSA S16 and AISC 360 may overestimate the inelastic buckling capacity of welded members, which has culminated in the proposal of new beam design equations. However, some caution should be exercised with numerical results, as researchers often use overly-severe residual stress distributions and geometric imperfections. Nonetheless, the simulations have provided informative results on the relationship between residual stresses, initial geometric imperfections, load height, and LTB resistance. In these aspects, the physical testing evidence is not as clear. Measured lateral out-of-straightness values are highly variable and, similarly, the effect of different residual stress distributions (e.g., rolled vs. welded) on LTB resistance could not be definitively observed. Moreover, the reviewed experimental research did not examine the effect of load height though, in some studies, the load height effect was negated by laterally bracing the member at the load points. Experimental studies have, however, indicated that welded members tend to show larger scatter and lower mean LTB resistance as compared to

their rolled counterparts. While this is consistent with expectations from theory, the physical testing results should nevertheless be used prudently as the majority of tests was conducted in the 1960s to 1980s. Significant updates in fabrication procedures since then means the test results may not be representative of the capacities of modern welded girders.

### 3 TEST GIRDER CHARACTERISTICS

As part of the physical testing programme, influential parameters affecting inelastic lateral-torsional buckling (LTB) were identified and used to inform the test matrix development. The primary goals were to select girders that incorporated the various identified parameters to examine their effect on LTB resistance and to ensure girder fabrication followed conventional modern processes. This chapter discusses the development of the test specimen matrix and the design considerations. The measured initial geometric imperfections, residual stresses, and material properties are also presented.

#### 3.1 Test Specimen Matrix

A methodical approach was adopted for the development of the test specimen matrix. To begin, it was important to first establish a load configuration. The possible cross-section geometries were then explored and constraints in the test set-up were assessed. Lastly, a selection criterion that considers influential parameters to LTB resistance was used to select the final test girders.

##### 3.1.1 Load Configuration

The premise of the experimental programme was to conduct large-scale testing, as previous physical tests primarily constituted girders of smaller scale, with typical girder depths of 150 to 350 mm. The selected load configuration considers a girder with a span of 9.75 m (32 ft), and was simply supported in-plane and torsionally pinned with eight applied points loads,  $P$ , spaced 1.22 m (4 ft) apart, as shown in Figure 3-1. As lateral bracing was provided only at the end supports, the unbraced length of the girder was the full 9.75 m span. To make use of a load configuration with a well understood moment distribution, eight equally spaced point loads were chosen, which resembles a uniformly distributed load. The number of applied loads was limited by the number of loading apparatuses available for use and laboratory floor space. The significance of the 1.22 m (4 ft) load spacing comes from the floor holes in the laboratory, which are spaced in a 0.61 m (2 ft) grid pattern and are necessary for anchoring the loading apparatuses. This loading configuration formed the basis for the development of the test matrix.

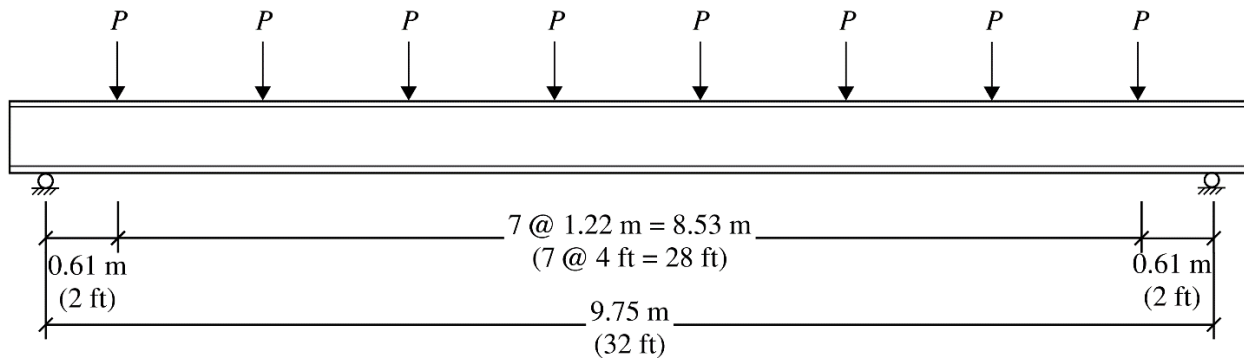


Figure 3-1: Load configuration

### 3.1.2 Cross-section Geometry

As part of determining cross-section geometry, the capacity limit of the laboratory had to be considered. The loading apparatuses were the limiting component in the test set-up, with a capacity of 360 kN, as discussed in Section 4.2.1.1. The cross-section dimensions considered were flange width ( $b$ ), flange thickness ( $t$ ), web thickness ( $w$ ), and section depth ( $d$ ). To understand the effect of cross-section geometry on LTB resistance, a series of surface plots using MATLAB (Mathworks 2017) were generated, with the  $x$ -axis as one cross-section dimension, the  $y$ -axis as a different cross-section dimension, and the  $z$ -axis as the nominal LTB resistance calculated in accordance with CSA S16-14 (CSA 2014a). Surface plots allow the effect of one cross-section dimension on LTB resistance to be observed relative to that of another, as shown in the surface plot of  $b$  vs.  $t$  in Figure 3-2, where  $M/M_p$  is the normalised moment resistance. The slopes of the  $x$ - $z$  and  $y$ - $z$  planes can be interpreted as the respective dimension's influence on LTB resistance. In Figure 3-2, for example, the flange width appears to be more influential than flange thickness, as it forms a steeper slope with the  $z$ -axis.

To determine the extents of the  $x$ - and  $y$ -axes (i.e., the range of each dimension), a list of standard welded wide-flange shapes from the *Handbook of Steel Construction* (CISC 2014) that would fail in inelastic LTB under the eight 360 kN point loads was created. In this list, the smallest and largest values of each cross-section dimension were identified and used to form the range for that dimension. For example, the smallest and largest flange widths of standard welded wide-flange

sections that failed in inelastic LTB under the load configuration were 300 mm and 650 mm, respectively, which then formed the extents of the flange width axis shown in Figure 3-2.

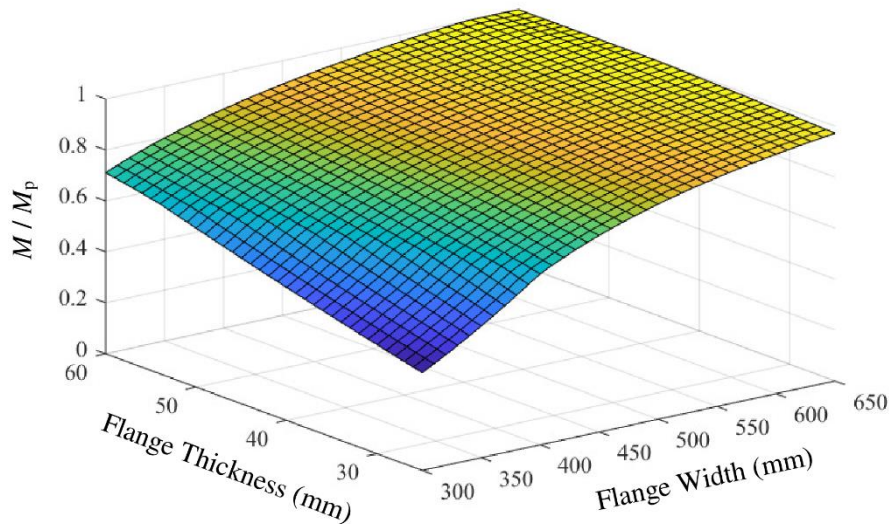


Figure 3-2: Effect of flange thickness and width on LTB resistance

As only two dimensions were varied on a given surface plot, the other two dimensions had to be kept constant. The geometry of the WWF1000×293 was used for this purpose, as it was deemed geometrically representative of the eventual test specimens. In Figure 3-2, the flange widths and thicknesses were varied, but the web thickness and section depth of WWF1000×293 were used as constants, and similarly follows for other combinations. Through creating surface plots for every possible combination of dimensions for the  $x$ - and  $y$ -axes, the relationships between dimensions and their effect on LTB could be observed, as detailed below.

- Flange width had a larger effect on LTB resistance than flange thickness.
- Increasing section depth combined with narrowing flange widths significantly reduced LTB resistance, as shown in Figure 3-3. However, at large flange widths the effect of varying section depth had little effect on LTB resistance.
- In comparing the effects of flange thickness and section depth on LTB resistance, there was no noticeable dominant effect of one cross-section dimension over the other.
- Varying web thickness had the least effect on LTB resistance, while flange width had the greatest influence; section depth and flange thickness fall somewhere in between.

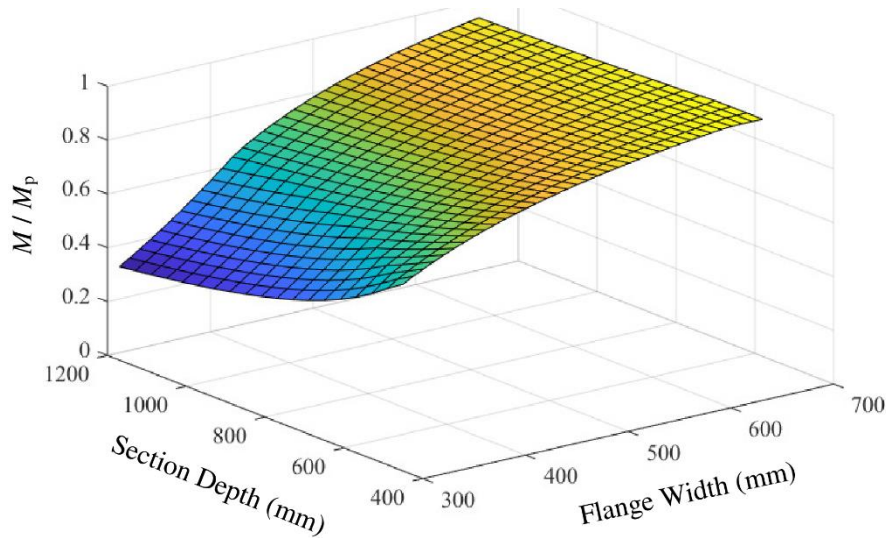


Figure 3-3: Effect of section depth and flange width on LTB resistance

The surface plot analysis revealed that flange width was the most influential dimension in determining LTB capacity, which is consistent with expectations as LTB is greatly influenced by weak-axis flexural stiffness. It is important to note that all sections were assumed to be able to reach their plastic moment capacity, which was deemed acceptable for the current stage, as the purpose was to observe overall trends of the effect of cross-section dimensions on LTB.

### 3.1.3 Test Constraints

With an improved understanding of cross-section geometry, the attention turned to test specimen selection, which began with considering several test constraints. The selected girders must fail in inelastic LTB, local buckling requirements had to be satisfied, shear checks had to pass, and girder capacity was not to exceed laboratory capacity (limited by the 360 kN capacity of the gravity load simulators). A MATLAB (Mathworks 2017) code was written to implement these constraints and generate the available cross-section geometries for two section classes: Class 1/2 and Class 3. As part of this process, a range for each cross-section dimension had to be determined to create a database of cross-sections from which to choose. Several discussions with industry partner Supreme Group were conducted at this point and their input regarding realistic values for  $b$ ,  $d$ ,  $t$ , and  $w$  was considered for the initial test matrix. Additionally, as they tend to be more readily available, imperial plate thicknesses were used.

The ranges of cross-section dimensions considered were:

- $b = 200 - 600$  mm, in 10 mm increments
- $d = 600 - 1000$  mm, in 100 mm increments
- $t = \{19.1, 22.2, 25.4, 31.8, 38.1\}$  mm or  $\{0.75, 0.875, 1, 1.25, 1.5\}$  in.
- $w = \{9.53, 12.7\}$  mm or  $\{0.375, 0.5\}$  in.

Using the above ranges of dimensions generated 4000 possible cross-sections for the initial test matrix. However, after applying the constraints, the number of possible sections reduced to 143 (3.6% of the original sample size), with shear check and lab capacity being the most limiting factors. For Class 3 sections, web slenderness was also a dominant constraint as it is difficult to achieve a sufficiently slender web (to be considered Class 3) that also has adequate shear strength but does not exceed lab capacity.

#### 3.1.4 Test Specimen Selection

A holistic approach that considered various influential parameters was used to select the final test specimens from the 143 cross-sections that met the test constraints. Eleven test girders of nine unique cross-section geometries formed the final test specimen matrix, as presented in Table 3-1. For fabrication purposes, the test girders were assigned a fabrication number. However, for this report, girders will be referred to by an alphanumeric specimen identification (ID) that indicates information regarding their cross-section dimensions, section class, and plate cutting method. The naming convention is ‘G’ (for girder) followed by: first digit of section depth in mm – flange width in mm – flange thickness in mm – section class – cutting method (‘p’ for plasma and ‘f’ for oxy-flame).

Girders were 10.4 m (34 ft) in length but spanned 9.75 m (32 ft) from support to support; the additional length of 0.305 m (1 ft) on either end of the girder was required for boundary support configuration in the laboratory. The flange and web thicknesses of 31.8 mm, 25.4 mm, 12.7 mm, and 9.53 mm correspond to standard imperial plate thicknesses of 1.25 in., 1 in., 0.5 in., and 0.375 in. The methodology and various parameters considered in the selection process are discussed in the following sub-sections.

Table 3-1: Test specimen matrix

No.	Specimen ID	Qty	$w$ (mm)	$d$ (mm)	$b$ (mm)	$t$ (mm)	$A$ (mm <sup>2</sup> )	$J$ ( $\times 10^3$ mm <sup>4</sup> )	$C_w$ ( $\times 10^9$ mm <sup>4</sup> )	$I_y$ ( $\times 10^6$ mm <sup>4</sup> )	$d/b$	$L/r_y$
SP1	G6-470-32-2-p	1	12.7	600	470	31.8	36659	10417	44359	549	1.28	79.7
SP2-1	G6-430-32-1-p	2	12.7	600	430	31.8	34119	9563	33971	421	1.40	87.8
SP2-2	G6-430-32-1-f											
SP3	G6-300-32-1-p	1	12.7	600	300	31.8	25864	6789	11541	143	2.00	131
SP4	G8-430-25-2-p	1	12.7	800	430	25.4	31359	5227	50507	337	1.86	94.1
SP5	G8-390-32-2-p	1	12.7	800	390	31.8	34119	8846	46335	314	2.05	102
SP6	G8-390-25-2-p	1	12.7	800	390	25.4	29327	4790	37687	251	2.05	105
SP7-1	G9-360-32-3-p	2	9.53	900	360	31.8	30828	7932	46541	247	2.50	109
SP7-2	G9-360-32-3-f											
SP8	G9-360-25-3-f	1	9.53	900	360	25.4	26377	4185	37782	198	2.50	113
SP9	G9-430-25-3-f	1	9.53	900	430	25.4	29933	4950	64376	337	2.09	92.0

### 3.1.4.1 Range of Inelastic Behaviour

This study is focused on the inelastic LTB range, as it has been identified as a region where the CSA S16-14 provisions may over-predict LTB resistance (Kabir and Bhowmick 2016; MacPhedran and Grondin 2011). Therefore, it was important to capture a spectrum of inelastic behaviour with test girder geometries selected to cover a range of both LTB resistances and slenderness ratios. The resulting test matrix is depicted in Figure 3-4 in terms of the relationship between normalised moment capacity and girder slenderness ratio. The limits for inelastic LTB prescribed by CSA S16-14 for Class 1/2 sections are  $0.67 < M/M_p < 1.0$  and are similarly defined for Class 3 sections as  $0.67 < M/M_y < 1.0$ . Subramanian and White (2017) found that the transition from inelastic LTB to plastic capacity produced the greatest difference between their numerical simulations and the AISC 360-10 (AISC 2010) predictions. Although the moment capacity of G6-470-32-2-p (labelled in Figure 3-4) was near the lab capacity limit, it was purposely chosen to provide a representative data point for girders with strengths near their plastic capacity.

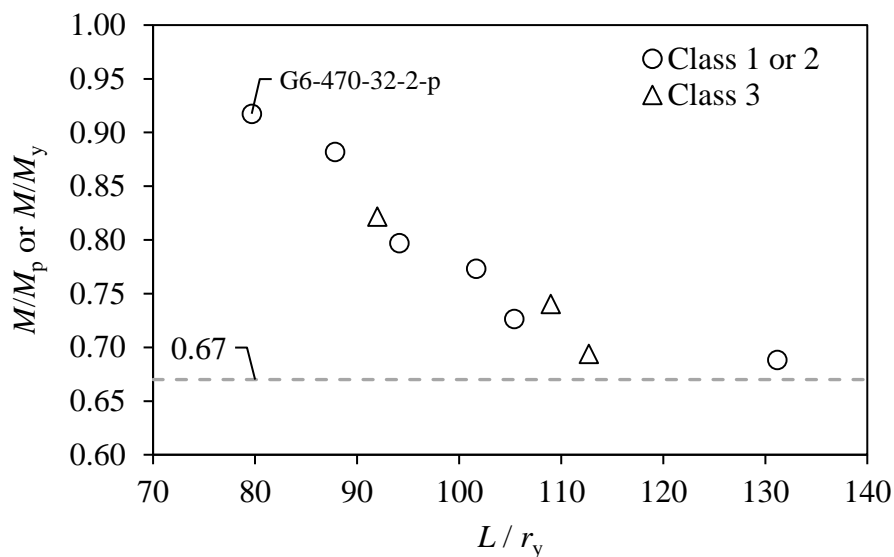


Figure 3-4: LTB resistance vs. slenderness ratio for test specimens

### 3.1.4.2 Geometric Variability

Observations from the surface plot analysis aided in selecting nine unique cross-sections from the 143 possible. Flange widths ranged from 300 mm to 470 mm, with five different widths in total; it was the most varied dimension as the surface plot analyses revealed it to be most critical of cross-section dimensions considered for LTB resistance. The increments between flange widths were always 30 mm or more, as the effect on LTB would not be significantly observed in smaller increments. Three section depths—600 mm, 800 mm, and 900 mm (referred to as the G6, G8, and G9 series)—were considered, as section depth was shown to be influential to LTB resistance. While flange thickness was shown to have a similar degree of influence on LTB resistance as section depth, a large difference in thickness would be necessary to observe its effect. Two flange thicknesses—25.4 mm and 31.8 mm—were included, as thicker flanges could not be used due to lab capacity constraints. Although web thickness was not observed to be an influential dimension for LTB resistance, two thicknesses were necessary to effect different web classes, as discussed in Section 3.1.4.4. A web thickness of 12.7 mm corresponds to a section class of 1 or 2, while the 9.53 mm web thickness results in Class 3 sections. As the cross-section geometries change, cross-sectional properties—such as area, minor axis moment of inertia, St. Venant torsional constant, and warping torsional constant—also change, which directly affect LTB resistance. By changing cross-section geometry, these cross-sectional properties were inherently accounted for when selecting sections to cover a range of inelastic behaviour.

### 3.1.4.3 Aspect Ratio

Defined as  $d/b$ , the aspect ratio indicates the stockiness or slenderness of the cross-section. Following Greiner and Kaim's (2001) distinction, stocky sections are considered to have  $d/b \leq 2$ , while slender sections are defined as having  $d/b > 2$ . The aspect ratio can be interpreted as a simple proxy for the moment of inertia about the strong axis relative to that of the weak axis, which may have an effect on LTB resistance. Moreover, the surface plot analysis indicated that large aspect ratios significantly reduce LTB resistance. Therefore, the chosen test girders range in aspect ratios from 1.38 to 2.50, with four stocky and seven slender sections.

### 3.1.4.4 Section Class

The test specimen matrix considers girders of three section classes, though CSA S16-14 only differentiates moment capacity between sections of Class 1/2 and Class 3. In early discussions with Supreme Group, inclusion of Class 3 sections in the test matrix was deemed important given their applicability to industry. Welded girders are often used in bridge construction and typically fall under section class 3 due to their slender webs. The G9 series was included with this in mind and were furthermore designed to comply with typical bridge girder specifications. Before finalising the test matrix, the proposed sections were reviewed by Supreme Group. They confirmed that the cross-section proportioning of the Class 3 girders was representative of nearly half-scale bridge girders.

In addition to the overall section class, girders were chosen to include a range of flange class and web class combinations, as indicated in Figure 3-5; the maximum values of the  $x$ - and  $y$ -axes represent the associated limits for Class 3 sections. Though CSA S16-14 is only concerned with overall section class, it is possible for the flange and web of a member to fall into different classes, which could influence LTB resistance. Furthermore, the degree to which the flange and web fall into each category—e.g., firmly Class 1 or at the boundary between Class 1 and 2—could also create nuances in LTB strength and were considered in the test specimen matrix.

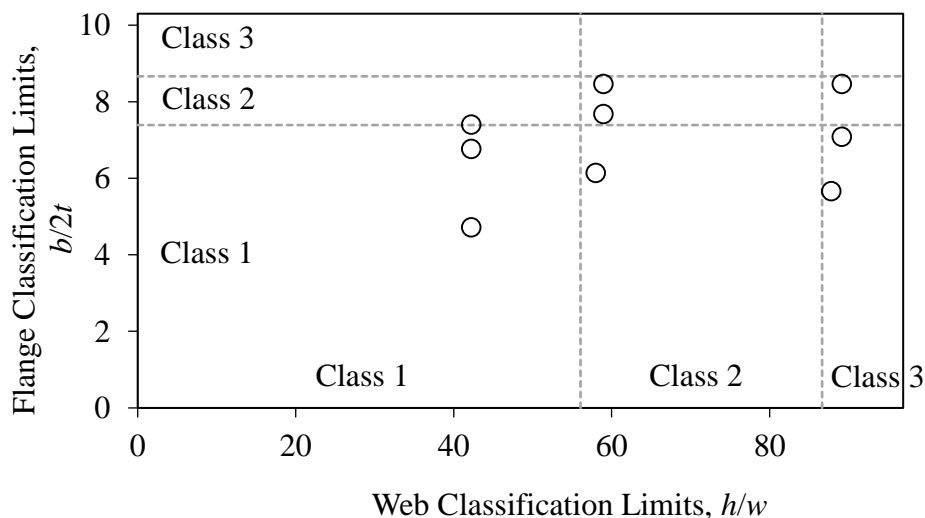


Figure 3-5: Flange and web classes of selected test specimens

### 3.1.4.5 Cutting Method

The cutting method of individual plates has been shown to have an effect on residual stress (Ballio and Mazzolani 1983; Subramanian and White 2017), which is an influential parameter in determining LTB resistance. Discussions with Supreme Group indicated that the two common cutting methods in their fabrication shop were plasma- and oxy-flame-cutting. Plasma-cutting is faster and produces a cleaner cut edge, which makes it favourable from a fabrication point of view. However, it can affect the hardness of the plate material and is more commonly used for building applications, where fatigue is not a significant concern. Plates for bridge girders typically use flame-cutting; in fact, Alberta Transportation's Standard Specifications for Bridge Construction (2017) necessitates that all plate material for main members be flame-cut. This appears to be a client-specific requirement as the Canadian bridge design code, CSA S6-14 (CSA 2014b), does not enforce a cutting method for steel bridge girders.

To follow Supreme Group's typical fabrication processes, the G6 and G8 series girders were plasma-cut as they resemble building-type girders, while the G9 series were flame-cut as they are representative of bridge-type girders. To further analyse the effect of different plate cutting methods, G6-430-32-1 and G9-360-32-3 were fabricated using both methods. As no geometric properties change, the effect of cutting method was isolated for the selected specimens.

## 3.2 Test Girder Design

A major objective of the research is to conduct physical testing on specimens that are representative of modern North American welded girders, which influenced many of the design decisions. As part of this objective, one week was spent at the Supreme Group fabrication shop in Acheson, Alberta to learn about the fabrication process of welded girders. Engineering drawings for the test girders can be found in Appendix A.

All girders were fabricated from CSA G40.21-13 (CSA 2013b) grade 350W steel and were designed in accordance with both CSA S16-14 and CSA S6-14 specifications to increase the applicability of the research. While the standards are similar (within the scope of this research), the CSA S6-14 requirements were found to be slightly stricter. For example, bearing stiffeners

were needed for all test girders and had to be full-depth per CSA S6-14 specifications, whereas CSA S16-14 does not impose the full-depth requirement.

Shear strength was an important limit state to consider. To include Class 3 sections (i.e., the G9 series) in the test matrix without exceeding laboratory capacity limits meant that the girders would have insufficient shear strength. The solution was to use intermediate transverse stiffeners in the G9 series; when loaded in shear, the transverse stiffeners create panels in the girder that exhibit truss-like behaviour, which is referred to as tension-field action. The added shear capacity is due to tensile forces forming in the web and compressive forces in the transverse stiffeners. The stiffeners were located at load points and were provided on both sides of the web; G9-360-32-3-p/f and G9-430-25-3-f required two sets of stiffeners at each end, while G9-360-25-3-f only needed one set per end (in addition to the bearing stiffeners). All the intermediate transverse stiffeners were 795 mm in depth and were welded to the girder along the web and the compression flange; they were intentionally chosen not to extend the full depth of the girder, which reduced fabrication times. Both bearing and intermediate transverse stiffeners were 125 mm wide and 12.7 mm (0.5 in.) thick, with 25×25 mm shear-cut copes to clear the web-to-flange welds. Plasma-cutting was used for all stiffeners.

Supreme Group's welding procedures were followed and two welding processes were used: submerged arc welding (SAW) and metal-cored arc welding (MCAW). SAW was used for all web-to-flange welds and MCAW was used for stiffener welds. Continuous fillet welds on both sides of the web and stiffener were specified and matching electrodes for 350W steel were used in all cases. The minimum weld size requirements governed—8 mm for web-to-flange welds and 6 mm for stiffener to web/flange. All welds were visually inspected by an in-house welding inspector. The weld direction and sequence were also marked on all girders, as it may affect residual stress distribution. Prior to welding, materials were preheated to the minimum temperature specified by CSA W59-13 (CSA 2013a). Should the completed girders' dimensional tolerances exceed the CSA W59-13 and CSA G40.20-13 (CSA 2013b) limits, heat straightening was permitted, provided that it was rigorously documented. However, heat straightening was not deemed necessary for any of the girders.

While adherence to the typical industry practices was important, the research remains a fundamental study of LTB behaviour. Some parameters were not considered—even though they may be common in industry applications—to limit the number of manipulated variables. For this reason, test girders did not include a specified camber and only continuous plates were permitted (i.e., no shop splices).

### 3.3 Measurement of Initial Geometric Imperfections

Initial geometric imperfections have been shown to have a large influence on LTB resistance and were documented for each test girder. Cross-section imperfections and global geometric imperfections were measured at five equally divided points, as shown in Figure 3-6, where Point 1 was considered the north end of the girder, Point 5 was considered the south end, and the cardinal directions corresponded to the north and south ends of the I.F. Morrison Structural Engineering Laboratory at the University of Alberta, where the tests were performed. Prior to recording imperfections, the centrelines of the top and bottom flanges were marked at the five locations.

While the complete test matrix comprises 11 girders, time constraints meant that the results of only seven girders could be included in this report. Therefore, initial geometric imperfections were only measured for the seven tested girders and are herein presented. The remaining four sections will be tested as part of a continuing research initiative at the University of Alberta Steel Centre.

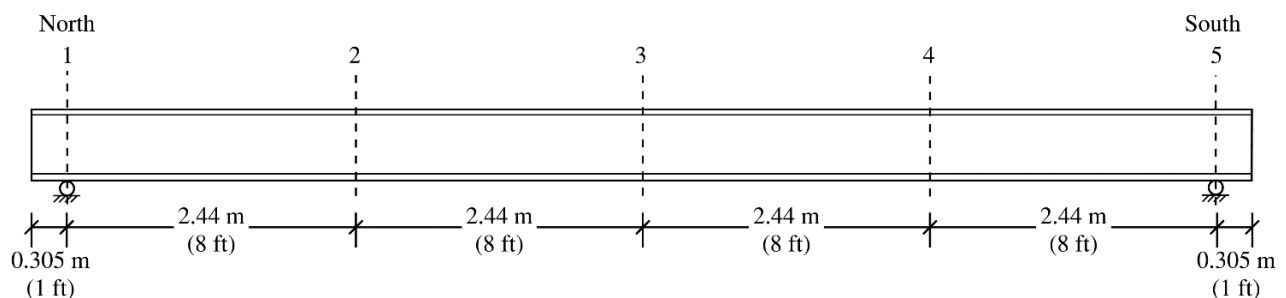


Figure 3-6: Measurement locations along test girder

### 3.3.1 Cross-section Measurements

Cross-section measurements were taken prior to testing to report the as-built dimensions of each girder and to assess cross-sectional imperfections. Figure 3-7 illustrates the different dimensions measured, as well as where on the cross-section they were measured. Table 3-2 provides a summary of the mean as-built dimensions at the five points along the beam. To reduce human error and inaccuracies in measurement instrumentation, two measurements of a given dimension were completed and/or the dimension was measured at different locations on the cross-section. To measure the flange width and section depth, a measuring tape was used. Callipers were used for measuring the flange thickness, while ultrasonic thickness measurement was employed for the web. As the remaining measurements shown in Figure 3-7 were difficult to access with a tape measure, they were measured with a Fluke 414D distance-measuring laser that can measure up to 50 m with a 2 mm accuracy.

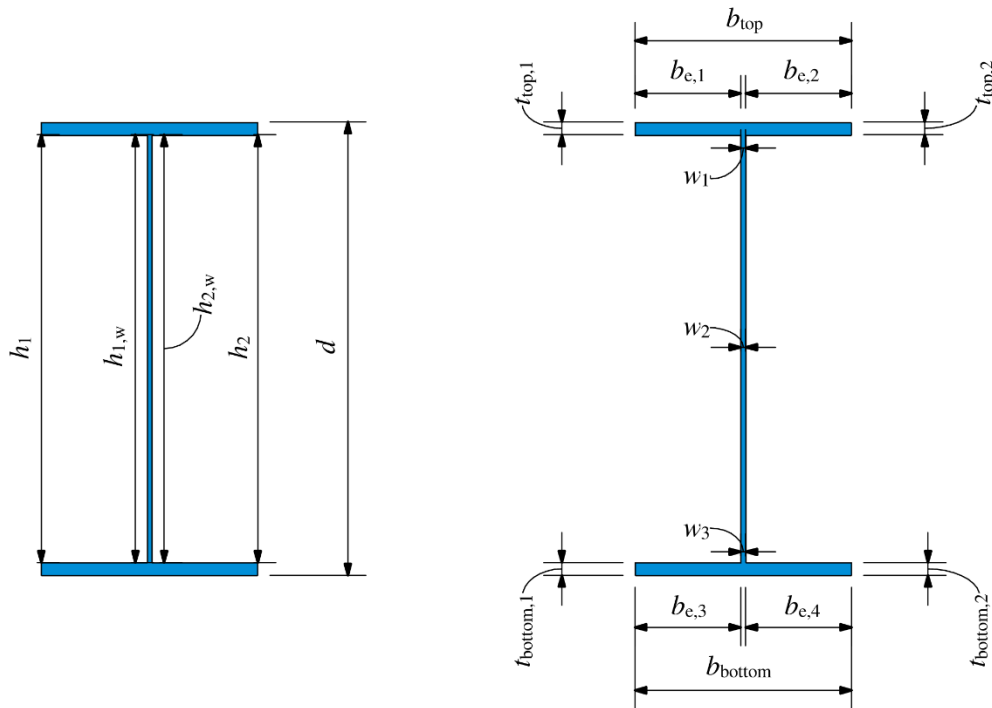


Figure 3-7: Cross-section measurements of test specimens

At the five points, section depth was measured along the flange tips (as indicated in Figure 3-7), but was often found to be approximately 10 mm below the nominal value. To investigate, the

section depth was also measured at the ends of the girders, through the web centreline rather than along the flange tips, and was found to match closely with the nominal value. This discrepancy may be due to weld distortion, which occurs when the contraction of the weld metal during cooling warps the base material. In this case, the distortion of the web-to-flange weld may have caused the flange tips to curl towards the web, thereby resulting in a seemingly smaller section depth when measuring along the flange tips. However, in some cases, the flange tips did not curl; instead, there was a tilt in the flange whereby one side of the flange was lower than the other—perhaps caused by the weld on one side of the web “pulling” more than the other or a misaligned web-to-flange angle. As a result of these imperfections, the section depths reported in Table 3-2 are the mean values measured at the ends of the girders (rather than at the five points). Another considered cross-section imperfection was the position of the web on the flange width. This is characterised by  $b_e$ , which measures the distance between the flange tip and the web and therefore indicates whether the web was welded to the centres of the flanges. By comparing the measured values of  $b_{e,1}$  to  $b_{e,2}$  and  $b_{e,3}$  to  $b_{e,4}$ , the webs of the fabricated specimens were observed to be relatively centred on the flange, with small misalignments of 0 to 3 mm from centre.

The margin of error generally accepted for plasma- and flame-cutting is 3 mm from the specified width. However, for G6-470-32-2-p, G6-430-32-1-p/f, G6-300-32-1-p, and G8-390-32-2-p, there was up to 9 mm difference between the specified and fabricated flange widths. Further investigation revealed that the nesting of the flange pieces on the 31.8 mm thick plate material was very tight. It seems likely that the assumed gap between the flange pieces was unachievable during fabrication and the flange pieces were purposely cut narrower to compensate, though it was not documented in the inspection and test plan.

Table 3-2: Test specimen mean as-built dimensions

Specimen ID	$d$ (mm)	$b$ (mm)	$t$ (mm)	$w$ (mm)	$b_{e,1}$ (mm)	$b_{e,2}$ (mm)	$b_{e,3}$ (mm)	$b_{e,4}$ (mm)	$h_1$ (mm)	$h_{1,w}$ (mm)	$h_2$ (mm)	$h_{2,w}$ (mm)
G6-470-32-2-p	599	461	31.9	12.9	226	226	224	226	533	536	534	536
G6-430-32-1-p	599	422	32.1	12.9	206	204	207	208	538	537	530	537
G6-430-32-1-f	597	422	32.2	13.1	203	205	205	204	534	535	529	535
G6-300-32-1-p	599	291	31.8	13.0	139	140	139	140	536	537	533	537
G8-430-25-2-p	799	429	25.1	12.8	210	209	211	208	743	749	746	749
G8-390-32-2-p	800	382	32.1	12.9	187	188	187	189	729	735	738	735
G8-390-25-2-p	801	390	25.1	12.9	188	189	189	189	743	749	751	749

### 3.3.2 Global Geometric Measurements

The span length of the test girders was defined as the centre-to-centre distance of the bearing stiffeners—the points used for aligning the centres of the girder end support mechanism. The Fluke 414D was used to measure the distance between the bearing stiffeners (inside face to inside face); the thickness of the stiffener was then added to this measurement to obtain the centre-to-centre span length. The out-of-straightness imperfections—lateral out-of-straightness (sweep), camber, and twist—were measured at the five points along the girder; sweep and camber were measured at the top and bottom flanges, while twist was measured at the web.

For the sweep measurement of a given flange, a fine line was stretched tightly along the girder length and held in place with strong magnets at the girder ends. The line was positioned to pass through the flange centreline at Points 1 and 5; the sweep deviation at the remaining three points was then measured to the fine line from the marked flange centreline. This method was used to measure both the top and bottom flange sweep. For the specimens listed in Table 3-2, the non-dimensionalised initial sweep ranged from  $L/9800$  to  $L/1400$  in the top flange and  $L/9800$  to  $L/900$  in the bottom flange, with mean values of  $L/5500$  and  $L/4200$  in the top and bottom flanges, respectively. The tolerances specified by CSA W59-13 and CSA G40.20-13 limit sweep to  $L/1000$ , which means the bottom (tension) flange sweep of  $L/900$  (measured in G8-390-32-2-p) slightly exceeded the limits in these standards. The large range in measured sweep is indicative of the inevitable variability in fabrication.

As part of camber measurement, the Fluke 180LG line laser level was used to provide a continuous horizontal reference line across a  $180^\circ$  field of view above the top flange (for top flange camber) and below the bottom flange (for bottom flange camber). The laser is self-levelling and accurate to 3 mm when used at a 10 m distance from the measurement location. The principles of trigonometry were then used to determine camber, as shown in Figure 3-8 for the case of top flange camber. The vertical distance between the flange and the laser was measured at the five points (denoted  $D_x$  in Figure 3-8, where the subscript is the location along the beam). Using the measured  $D_1$  and  $D_5$  values, the slope between Points 1 and 5 was determined—this represented the slope of the laboratory strong floor (which is exaggerated in Figure 3-8). For the remaining three points,

the difference between  $D_x$  and a sloped notional line between Points 1 and 5 was the camber at that point. This is illustrated in Figure 3-8, where  $C_3$  is the measured camber at Point 3. The maximum camber recorded for each girder ranged from  $L/9800$  to  $L/1000$  for the top flange and  $L/7100$  to  $L/1300$  for the bottom flange, with mean values of  $L/3600$  and  $L/3700$ , respectively. As CSA W59-13 and CSA G40.20-13 specify a maximum camber of  $L/1000$  (for members with a specified camber of zero), all measured values were within the tolerance.

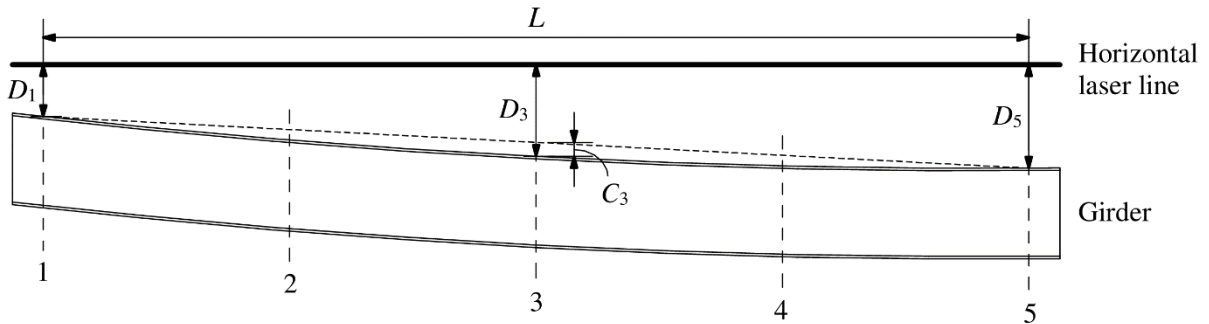


Figure 3-8: Camber measurement methodology

Twist was measured using the Mitutoyo Pro 360 digital protractor, with a precision of  $0.1^\circ$ . Assuming the girder webs had negligible out-of-flatness, the tilt of the web was considered representative of cross-section twist, where a perfectly vertical web (i.e.,  $90^\circ$ ) corresponded to zero twist. While sweep and camber values were measured with the test girder resting on pedestals on the laboratory strong floor, twist was measured once the girder was lifted into the test set-up. The girder web at both end supports was then aligned to  $90^\circ$  using the lateral braces and twist at the three intermediate stations was measured; measurements were taken on both sides of the web. By fixing the verticality of the web at the ends, girder stability at the supports was improved, which was important from a safety standpoint. A plumb web also provided consistency throughout the tests, as the twists at Points 2, 3, and 4 were always measured relative to a vertical web at the supports. The mean twist observed in the test girders was  $0.6^\circ$ ; CSA W59-13 and G40.20-13 do not specify a tolerance limit for twist. It should be noted that in some cases, the lateral direction of the top (compression) flange sweep and web twist were measured to be in opposite directions, as twist is related to the relative sweep of the two flanges.

Table 3-3 summarises the initial global geometric measurements; the reported values represent the maximum imperfection measured among the five points (and may not have occurred at mid-span). A positive sweep or twist value indicates bowing or tilting, respectively, towards the east direction of the laboratory and a negative camber corresponds to a sag. Top flange sweep and twist are expected to be the most influential imperfections. The largest top flange sweep and twist were measured in G8-430-25-2-p, with values of  $L/1400$  and  $1.3^\circ$ , respectively. G8-430-25-2-p was also the only test girder for which the maximum bottom flange sweep was in the opposite direction of the maximum top flange, which likely attributed to the larger twist value. Figure 3-9 and Figure 3-10 show the sweep and twist distribution for G8-430-25-2-p, where the  $x$ -axis represents the five points of measurement along the girder. Sweep, camber, and twist distributions for all test specimens are provided in Appendix B.

Table 3-3: Measured initial global geometric imperfections in test specimens

Specimen ID	Length, $L$ (mm)	Sweep / Length		Camber / Length		Twist ( $^\circ$ )
		Top Flange $\times 10^{-3}$	Bottom Flange $\times 10^{-3}$	Top Flange $\times 10^{-3}$	Bottom Flange $\times 10^{-3}$	
G6-470-32-2-p	9752	0.15	0.15	-0.10	-0.14	0.4
G6-430-32-1-p	9751	-0.21	-0.26	-1.00	0.77	0.6
G6-430-32-1-f	9761	-0.31	-0.10	-0.64	0.23	-0.3
G6-300-32-1-p	9755	0.31	0.26	-0.18	0.42	0.4
G8-430-25-2-p	9749	0.72	-0.36	-0.29	-0.18	1.3
G8-390-32-2-p	9760	-0.10	-1.13	-0.74	0.49	-1.1
G8-390-25-2-p	9751	-0.10	-0.62	-0.44	0.31	-0.2

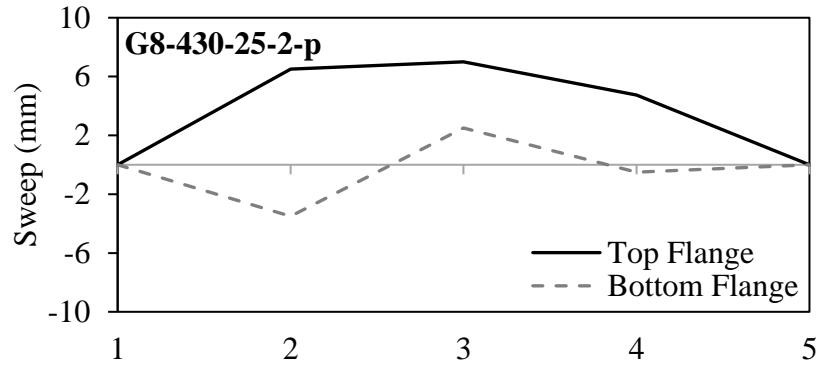


Figure 3-9: Initial sweep measurement of G8-430-25-2-p

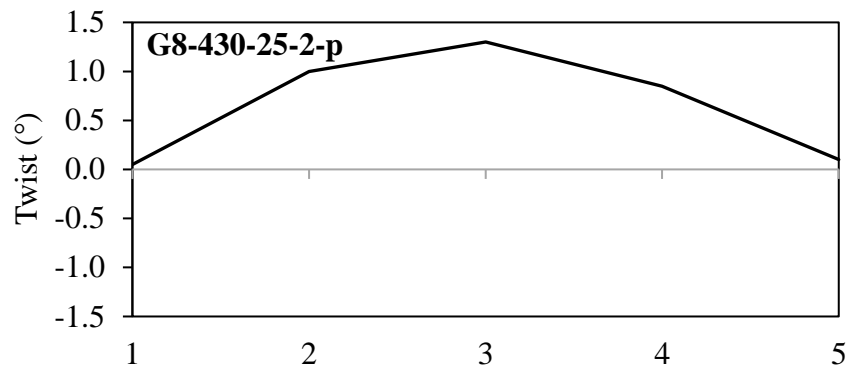


Figure 3-10: Initial twist measurement of G8-430-25-2-p

Table 3-4 provides a summary of the mean measured sweep and twist in this study and from previous physical testing programmes. Camber is not included in Table 3-4 as it was not always measured in other studies. The location at which sweep was measured varies among the studies; for this study, the mean top (compression) flange sweep was reported as it is more influential than bottom flange sweep. From Table 3-4, it is evident that initial imperfections vary significantly; the measured values for this study fall around the mean for sweep and above the mean for twist.

Table 3-4: Mean initial sweep and twist in different LTB studies

	Number of girders	Length, $L$ (m)	Sweep		Twist (°)
			Location <sup>†</sup>		
Current study	7	9.75	$L/5500$	TF	0.5
Fukumoto et al. (1980)	75	1.5 – 2.6	$L/12,500$	U	0.008
Fukumoto et al. (1981)	68	1.8 – 2.6	$L/3400$	U	0.03
Dux and Kitipornchai (1983)	9	5 – 11	$L/3600$	SC	0.01
Essa and Kennedy (1993)	11	9	$L/2000$	SC	1.2

†Location of sweep measurement: TF – Top Flange  
SC – Shear Centre  
U – Unknown

### 3.4 Measurement of Residual Stresses

Residual stresses are a crucial aspect of the experimental programme. Detailed residual stress measurements of each girder were taken using the sectioning method (Pekoz et al. 1981) and non-destructive ultrasonic method in a companion research project (Unsworth et al. 2019). In previous research projects, specimens were fabricated with additional length for the purpose of material testing and residual stress measurements. For this project, an additional length of 3.05 m (10 ft) was required. As test girders were already 10.4 m (34 ft) long, it was not feasible to source 13.4 m (44 ft) lengths of steel plate material. While splicing was an option, it would introduce additional welding into the girders and affect the residual stresses, which was undesirable. The selected solution was to fabricate the required additional length as an entirely separate 3.05 m girder. Therefore, each test girder would have a corresponding, geometrically identical, ancillary girder of 3.05 m length, fabricated with the exact same fitting and welding procedures. Plates for each test girder and its shorter twin were cut using the same method (either plasma- or flame-cut) and plates of the same thickness came from a single heat of steel for the entire test matrix.

The aim of performing ultrasonic measurements was to explore a non-destructive method of measuring residual stresses. As the ultrasonic method is under development, only the sectioning

residual stress results were used for this report. The sectioning method measures residual stresses through the release of elastic stresses. When a strip is cut out of a sample, the stresses in the strip are released; by measuring the change in length of the strip, the residual stress in the longitudinal direction of the girder at that point can be determined. For sectioning measurements, a 400 mm long sectioning piece was flame-cut from the middle of the 3.05 m long girder and then cut into 30 mm × 300 mm strips using a water-cooled band saw, the results of which are shown in Figure 3-11. Due to time constraints, only four sets of sectioning data were completed, but residual stresses will be measured for the remaining girders in a continuing research project. Complete details regarding the residual stress measurement programme are reported by Unsworth et al. (2019).



Figure 3-11: Sectioning strips for residual stress measurements (Unsworth et al. 2019)

The residual stress distributions of the four measured girders are shown in Figure 3-12 to Figure 3-15, where a positive stress value indicates tension and negative represents compression. To convert the strain measurements to stresses, the measured elastic modulus for each plate thickness from material testing was used. The results of the sectioning method indicate that the plasma-cut girders have small compressive residual stresses at the flange tips, with a mean of  $-16.0$  MPa. In the flame-cut girder, G6-430-32-1-f, the mean tensile residual stress at the flange tips was  $10.2$  MPa. In the simplified flame-cut residual stress model proposed by Chernenko and Kennedy (1991), the predicted tensile stress is  $0.7F_y$  at the flange tips, which would correspond to  $243$  MPa,

and is much greater than the measured stresses. In general, the measured residual stresses were smaller than those measured or proposed by previous researchers for welded sections (Chernenko and Kennedy 1991; Fukumoto and Itoh 1981; Kim 2010; Nethercot 1974).

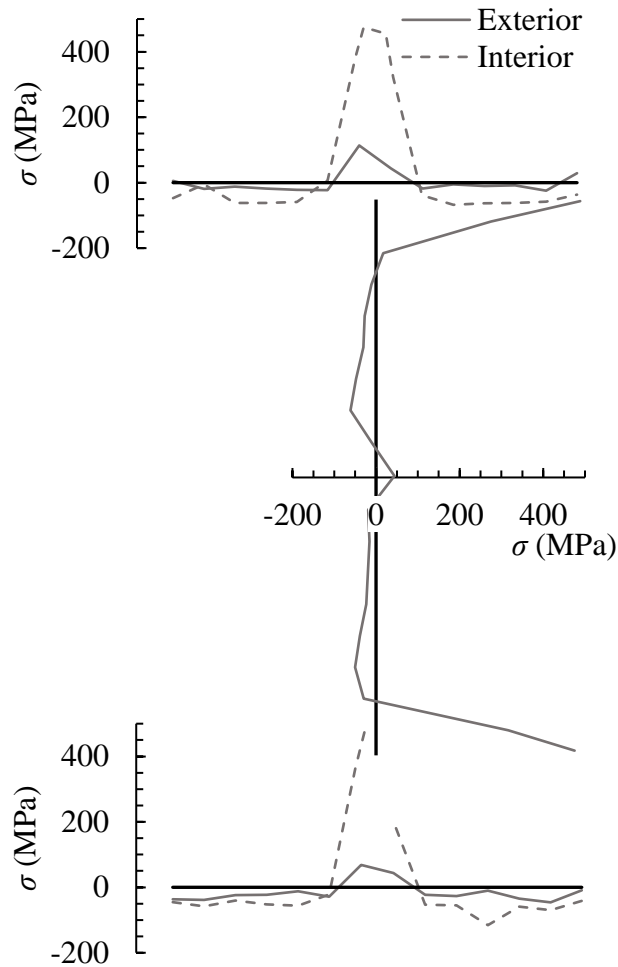


Figure 3-12: Residual stress  $\sigma$  distribution of G6-430-32-1-p (source data: Unsworth et al. 2019)

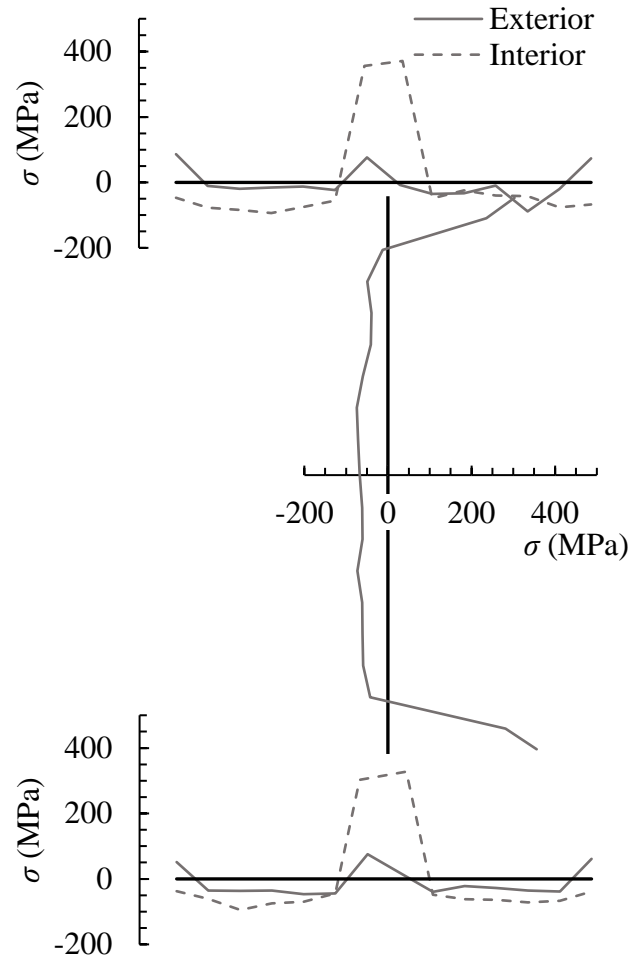


Figure 3-13: Residual stress distribution of G6-430-32-1-f (source data: Unsworth et al. 2019)

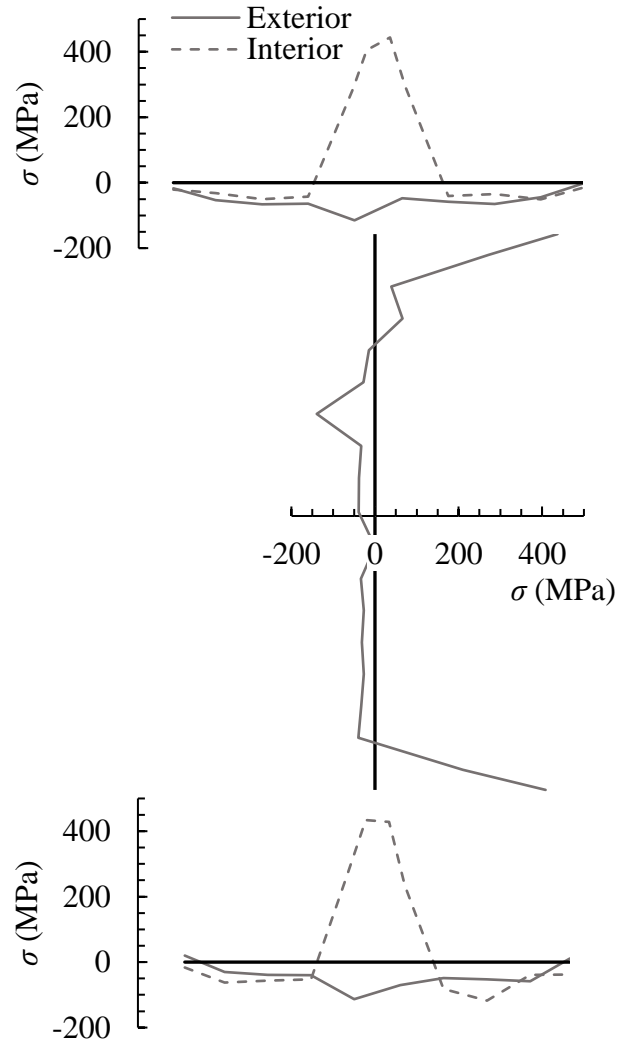


Figure 3-14: Residual stress distribution of G6-300-32-1-p (source data: Unsworth et al. 2019)

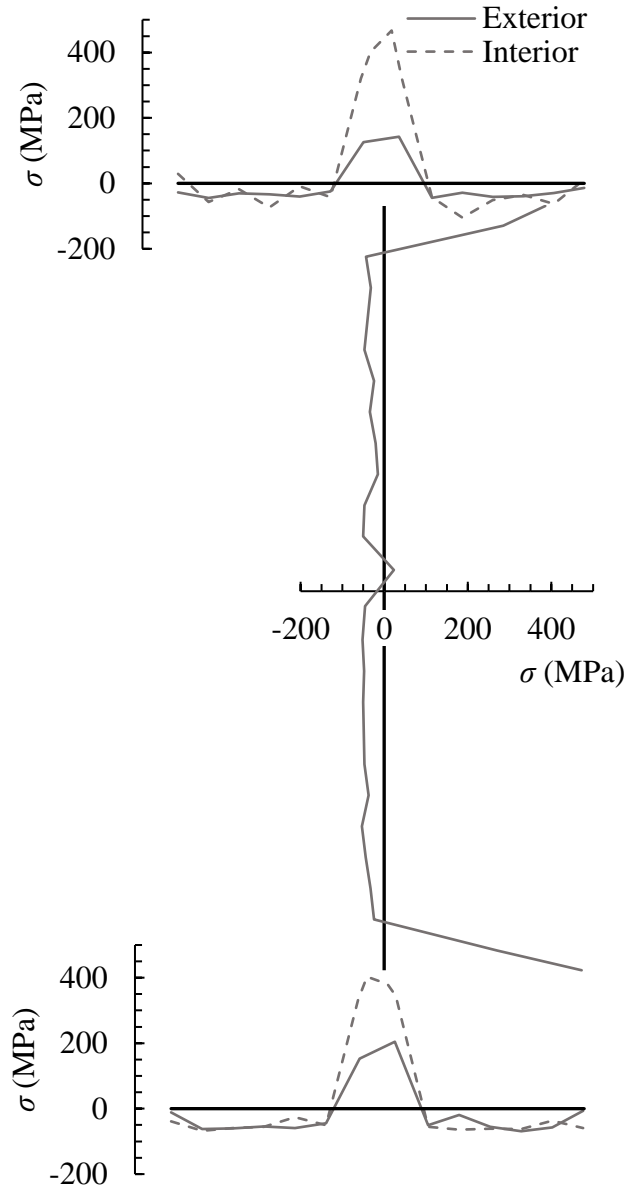


Figure 3-15: Residual stress distribution of G8-430-25-2-p (source data: Unsworth et al. 2019)

### 3.5 Material Properties

As the residual stress measurements required only a 400 mm long section of the ancillary girders, approximately 1.3 m of material remained on either side, as shown in Figure 3-16. One of these pieces was used for material testing to determine pertinent properties such as the elastic modulus, static yield stress, and static ultimate stress. Flame-cutting was used to separate the flanges from the web. From the flange and web plates, standard specimens of a dog-bone shape were cut following the requirements prescribed in ASTM A370-17 (ASTM International 2018). For plate thicknesses of 9.53 mm, 12.7 mm, and 25.4 mm, coupon dimensions followed those of sheet-type specimens with a 50 mm gauge length, while coupons for the 31.8 mm plate thickness were categorised as plate-type specimens with a 200 mm gauge length. Two coupons were cut from the web and from each flange, as shown in Figure 3-17; all coupons were water-jet cut and oriented parallel to the rolling direction of the girder. Callipers were used to measure the cross-sectional area of each coupon prior to testing. As steel plates of the same thickness were fabricated from a single heat, little variation in material property is expected between pieces of the same thickness. Therefore, it was deemed sufficient to conduct one set of top and bottom flange coupon tests—totalling four tests per flange plate thickness. Though only one set of web coupon tests were necessary, web coupons were taken from two different girders to similarly achieve four tests per web plate thickness.



Figure 3-16: Ancillary girder used for residual stress measurements and material testing (adapted from Unsworth et al. 2019)

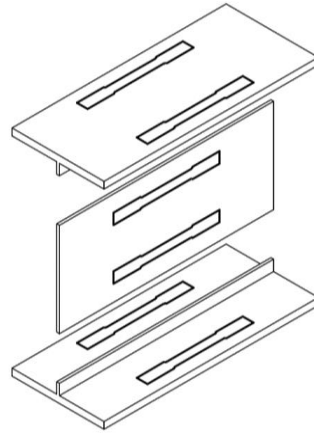


Figure 3-17: Tension coupon locations

A uniaxial load frame was used to exert a tensile strain on the coupon at a rate of 0.2 mm/min in the elastic region, which was increased to 3 to 4 mm/min at the onset of strain hardening. Three static readings were taken on the yield plateau and one more at the approximate maximum engineering stress to obtain a value for mean static yield stress and static ultimate stress, respectively. Table 3-5 summarises the results of the material tests that are most relevant to this research; the stress–strain curves for the tension coupons can be found in Appendix C.

As the grips in the uniaxial load frame were only rated to 500 kN, the 31.8 mm coupons could not be tested to failure; therefore, the static ultimate stress is not reported. The elastic modulus was calculated using a linear regression trendline to determine the slope of the stress–strain curve between zero and the proportional limit. As girders with web thicknesses of 9.53 mm have not been tested yet, tension coupon tests for the 9.53 mm were not completed. The yield stress and elastic modulus values for the remaining plate thicknesses were within the expected range.

Table 3-5: Summary of tension coupon material properties

Plate Thickness, $t$ (mm)	Yield Stress, $F_y$ (MPa)	Ultimate Stress, $F_u$ (MPa)	Elastic Modulus, $E$ (MPa)
12.7	364	450	203,673
25.4	355	442	202,368
31.8	347	-	201,263

## 4 EXPERIMENTAL PROGRAMME

To investigate the lateral–torsional buckling (LTB) behaviour of welded girders, an experimental programme consisting of flexural tests of 11 large-scale girders was developed and seven tests were performed in the I.F. Morrison Structural Engineering Laboratory at the University of Alberta. This chapter presents the preliminary pre-test numerical models, development of the girder-stability test bed, instrumentation plan, and test procedure.

### 4.1 Preliminary Pre-test Models

Under the eight point loads and simply-supported boundary conditions, the test girders are expected to move vertically and laterally, rotate torsionally, and displace longitudinally (at the end supports) as they undergo LTB. The load mechanisms and end supports must therefore accommodate their respective expected movements without imposing unintended restraint on the girders. As all test girders are anticipated to partially yield, a numerical model is advantageous for capturing inelastic behaviour. To estimate expected displacements and rotations at buckling and post-buckling for the design of the test set-up, a preliminary numerical model of the test specimens was developed in the general-purpose finite element software, Abaqus (Dassault Systèmes 2014). Buckling capacities from simulations can provide further insight into expected girder behaviour and be used for a preliminary comparison with CSA S16-14 (CSA 2014a) predictions. Details of the model are herein summarised; for simplicity, residual stresses were not modelled although their anticipated effects were considered in interpreting the simulation results.

#### 4.1.1 Elements and Meshing

Two-dimensional shell elements were used to model the test girders. Solid elements were deemed unnecessary for a preliminary pre-test model, particularly as the girders' flange and web thicknesses are considerably smaller than the span. However, three-dimensional brick elements may be useful for modelling thicker plates, where residual stresses may vary considerably through the thickness (Alpsten and Tall 1970). A general-purpose 4-node conventional shell element with reduced integration (S4R) was selected. General-purpose elements are robust and give accurate solutions for thick and thin shell models (Dassault Systèmes 2010). S4R is suited for large-strain

applications such as inelastic LTB simulations, and reduced integration was employed for faster computation times. A mesh size of 25.4 mm (1 in.) was chosen, which resulted to 12 to 16 elements across the flange width and 22 to 34 elements along the web depth; this is consistent with mesh densities used by other researchers in numerical LTB studies (Kabir and Bhowmick 2016; Subramanian and White 2017).

#### 4.1.2 Material Properties

An elastic–perfectly plastic stress–strain relationship was employed, as shown in Figure 4-1; for simplicity, strain hardening effects were omitted as anticipated strains were not large enough to elicit significant material hardening. As 350W steel was specified for the test girders, a probable yield stress of 385 MPa was chosen for simulations. An elastic modulus of 200 GPa and Poisson’s ratio of 0.3 were assumed.

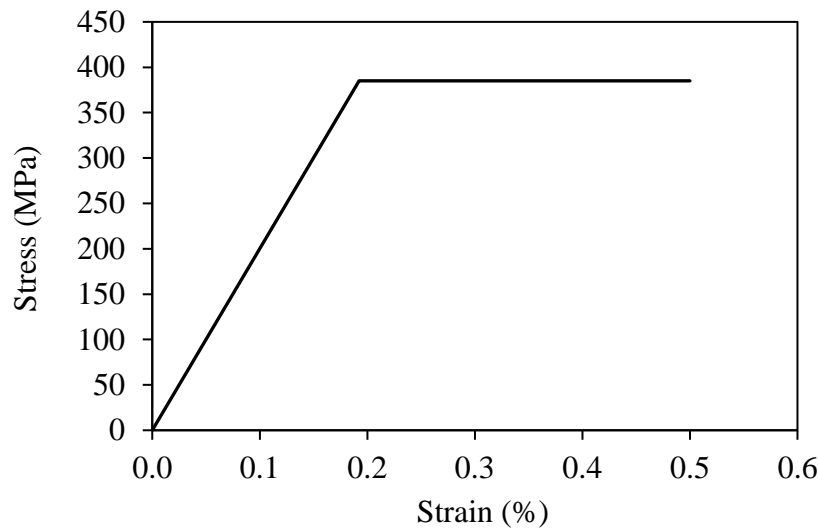


Figure 4-1: Stress–strain relationship used in numerical model

#### 4.1.3 Boundary Conditions

In the experimental set-up, test girders are simply-supported both in- and out-of-plane, as well as torsionally pinned, at both ends. To achieve this in Abaqus requires applying restraints to the applicable degrees of freedom. Creating a torsionally pinned condition, where the cross-section is permitted to warp but twist is prevented, requires particular attention. Previous researchers have

used Vlasov's beam kinematics theory to achieve the torsionally pinned condition, which defines an equation for calculating the longitudinal displacement of a generic point at both ends of a beam. Using Vlasov's theory, the theoretical warping displacements (for a perfect torsionally pinned member) can be defined for every node at the end support cross-sections. These equations can be applied to the boundary constraints in the model, thereby fixing the warping displacements to match theory and achieving the desired torsionally pinned boundary condition.

As Vlasov's approach is complex and time-consuming, a simplified procedure to achieve simply-supported in-plane and torsionally pinned boundary conditions was proposed and implemented in the finite element (FE) model. Though the girder actually rests on roller supports, the need for numerical stability dictated the use of a pin at one support and a roller at the other in the FE model to achieve the in-plane simply-supported condition. The orientation of the axes is shown in Figure 4-2 and the degrees of freedom are defined such that  $U_1$ ,  $U_2$ , and  $U_3$  signify translation in the 1-, 2-, and 3-direction, respectively, while  $UR_1$ ,  $UR_2$ , and  $UR_3$  represent rotation about the 1-, 2-, and 3-direction, respectively.

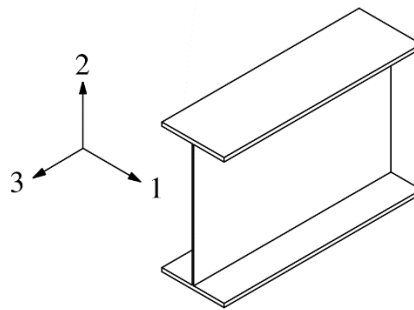


Figure 4-2: Conventions for degrees of freedom in numerical model

The support modelling procedure is:

1. Constrain all web nodes with a rigid body tie to the cross-section centroid;
2. Restrain web centroid against all degrees of freedom except for major- and minor-axis rotation ( $U_1 = U_2 = U_3 = 0$ ;  $UR_3 = 0$ ), and longitudinal movement if at the roller end ( $U_3$  is free);
3. At each flange, apply a kinematic coupling interaction to tie flange nodes to flange centroid (i.e., the reference node) so that all nodal degrees of freedom are defined by the motion of the reference node, except for warping displacement ( $U_1$ ,  $U_2$ ,  $UR_1$ ,  $UR_2$ , and  $UR_3$  constrained).

The simplified boundary condition treats the web as a rigid body, where the in-plane rotations of the web dictate the longitudinal displacement at the web–flange junction nodes. A coupling interaction then determines the corresponding warping displacements for the remaining flange nodes. This concept is illustrated in Figure 4-3. In the test set-up, the bottom flange of the girder rests on the boundary supports, which suggests the rigid body constraint should be tied to the bottom web–flange junction node instead of the centroid. However, this was found to create negligible differences and therefore the constraint was kept at the centroid.

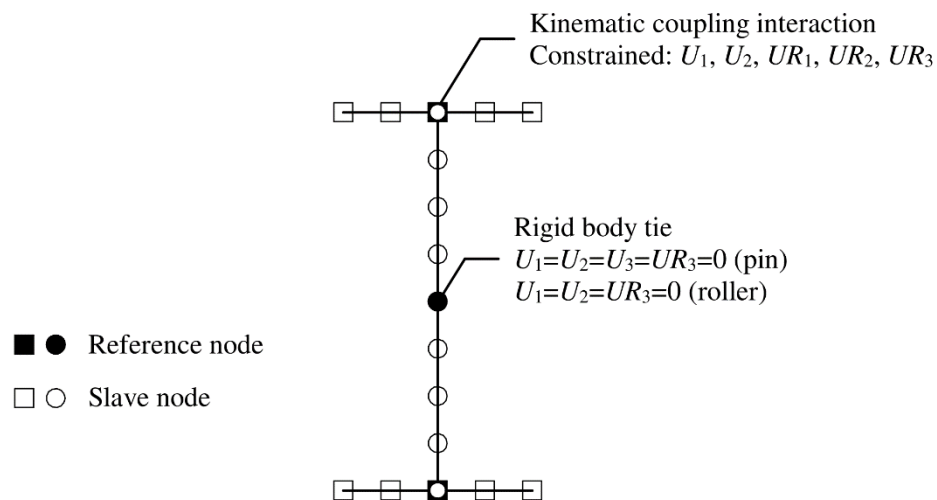


Figure 4-3: Boundary conditions in FE model

#### 4.1.4 Loading Procedure

A two-part analysis was completed to evaluate the buckling response of the test specimens. An eigenvalue buckling analysis was first performed to determine an initial or “seed” geometric imperfection before conducting a non-linear buckling analysis of inelastic LTB behaviour. While eigenvalue buckling is generally used to estimate the critical elastic buckling loads of stiff structures, its chosen utility was determining the elastic buckling mode shapes, which are useful estimates of collapse mode shapes for structures that exhibit non-linear response prior to buckling such as inelastic LTB (Dassault Systèmes 2010). During this analysis, a downward load perturbation was applied to the member at mid-span. Ten eigenvalues and their respective eigenvectors were then extracted using the Lanczos eigensolver method, where the eigenvectors represent the elastic buckling modes, which include LTB mode shapes. As the intent of this analysis was to obtain a seed geometric imperfection pattern, only the lowest LTB mode shape was of interest. The normalised LTB mode shape was then scaled so that the lateral out-of-straightness value at mid-span of the numerical model equalled the tolerance limit of  $L/1000$ , per CSA W59-13 (CSA 2013a) and CSA G40.20-13 (CSA 2013b) standards. The scaled LTB mode shape formed the initial geometric imperfection pattern for the subsequent non-linear analysis.

The Modified Riks method was chosen for the non-linear analysis of the test girders, as it can predict unstable post-buckling behaviour such as LTB. It assumes that the applied loading is proportional and the load–displacement response is smooth with no sudden bifurcations. The algorithm perceives a solution as a single equilibrium path in space; development of the solution (i.e., as loads and displacements increase) involves traversing this path as far as necessary (Dassault Systèmes 2010). As the Modified Riks method treats load magnitude as an unknown and solves for displacement and load simultaneously, the solution progress is tracked by an additional parameter: arc length along the static equilibrium path (Dassault Systèmes 2010). To ensure the correct buckling solution is obtained, the increment in arc length must be limited, as there is a finite radius of convergence and materials often have path-dependent responses (Dassault Systèmes 2010). An initial arc length increment and total arc length of 0.1 and 1 were chosen, respectively; as the solution progressed, the increment size was adjusted automatically based on convergence rate.

A load-controlled method was chosen over displacement-controlled because non-linear behaviour is anticipated, and the relationships between the vertical deformations at the eight load locations change once the member begins to yield. Elastic beam deflection theory can no longer be used, thereby rendering a displacement-controlled loading scheme impractical. In the analysis using the load-controlled method, each concentrated load was applied to a small area rather than a single node, which is more representative of actual loading conditions and prevents unrealistic stress concentrations that may cause the top flange to yield prematurely or buckle locally before LTB occurs. The small area was defined by a  $2 \times 2$  element set centred across the width of the top flange, as shown in Figure 4-4; an arbitrary 1 kN load was initially applied to each of the nine nodes that form the element set, and during the analysis the load was incrementally increased according to the arc length factor.

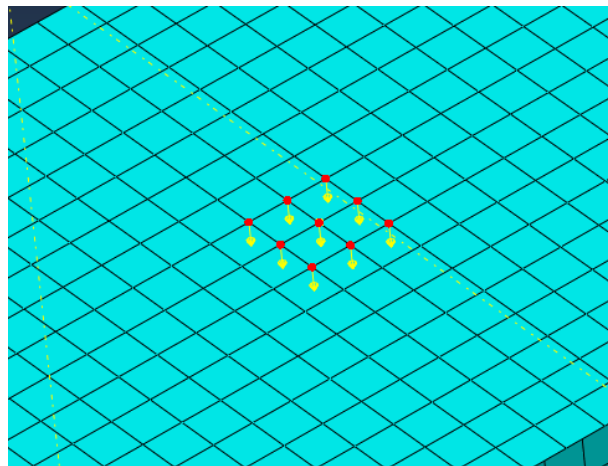


Figure 4-4: Load application to a nine-node,  $2 \times 2$  element area

#### 4.1.5 Model Verification

To validate the numerical model, experimental results by Fukumoto et al. (1980) were used. They performed 75 tests on nominally identical rolled beams, which were separated into three groups based on their unbraced lengths of 2.6 m, 2.0 m, and 1.5 m. Beams were simply supported in- and out-of-plane and torsionally pinned. A concentrated downward load was applied at mid-span to the compression flange, which was applied in the model as per the nine-node,  $2 \times 2$  element area defined in Section 4.1.4. Material properties measured from tension coupon tests were used and

the different yield strengths of the flange and web were accounted for. An initial lateral out-of-straightness of  $L/5000$  was applied, which corresponds to the 95<sup>th</sup> percentile value measured in the test specimens (individual lateral out-of-straightness values were not reported). Residual stresses were reported, but not included in the numerical model for simplicity. Table 4-1 summarises buckling capacity results from the experimental tests and FE models. Numerical simulations can predict member capacity within approximately 8%, which is reasonable considering the simplified nature of the model.

Table 4-1: Summary of buckling capacities for numerical model verification

Section	Yield Stress, $F_y$		Modulus of Elasticity, $E$	Length, $L$	$M_{max}$		Percent Difference
	Flange	Web			Test	FE Model	
	(MPa)	(MPa)	(GPa)	(m)	(kN·m)	(kN·m)	(%)
I-200×100×5.5×8				2.6	41.2	39.9	-2.98
	252	287	202	2.0	57.6	55.2	-4.18
				1.5	78.6	72.2	-8.13

While the numerical model must give good approximations of capacity (for model verification), the load–displacement response is also important as the FE predictions of expected movement will help inform the required displacement and rotation allowances in the test set-up. Load–displacement curves for experimental and FE results are provided in Figure 4-5 to Figure 4-7. Though the numerical model slightly underpredicts in-plane stiffness and over-predicts out-of-plane (lateral) stiffness, the overall response is adequately captured and the predicted displacements at buckling (i.e., the maximum applied load) are within 2 mm of test results.

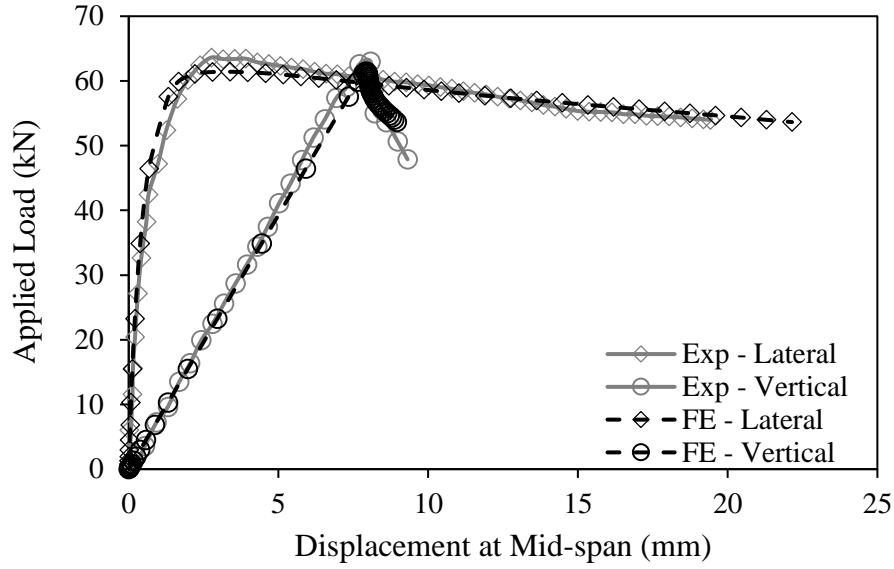


Figure 4-5: Load–displacement response comparing FE and experimental test results of Fukumoto et al. (1980) for 2.6 m series

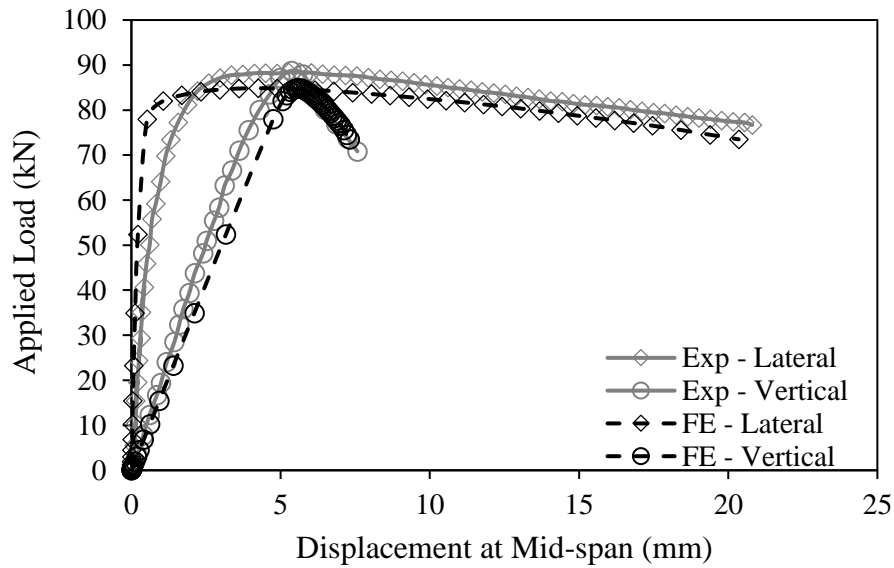


Figure 4-6: Load–displacement response comparing FE and experimental test results of Fukumoto et al. (1980) for 2.0 m series

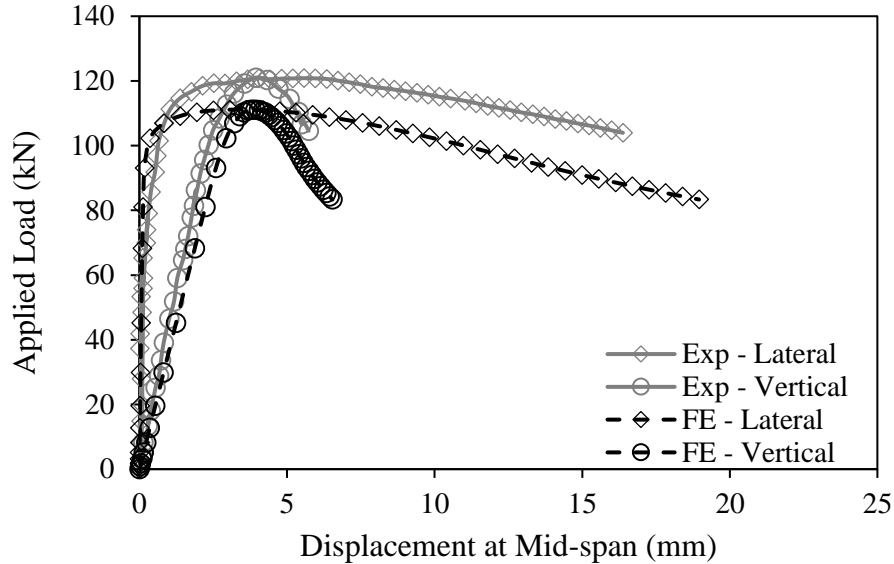


Figure 4-7: Load–displacement response comparing FE and experimental test results of Fukumoto et al. (1980) for 1.5 m series

#### 4.1.6 Results and Discussion

Following the model validation, the nine unique test girder cross-sections were modelled and pertinent displacements and rotations were extracted to aid in experimental set-up design. As the primary objective of physical testing was to determine the buckling capacity of the test girders, the displacements and rotations from the numerical model were taken at the buckling point, which is defined as the maximum attained load. A secondary objective was to continue past the peak load and capture the post-buckling response. In LTB failures, the vertical displacement generally increases little in the post-buckling domain, while the lateral movement steadily increases with a near-horizontal slope, as evidenced in the tests by Fukutmoto et al. (1980) shown in Figure 4-5 to Figure 4-7. Knowing the approximate post-buckling behaviour, considerations for extra displacement and rotation capacity could be made during the test set-up design.

In the experimental set-up, the critical locations that must accommodate girder movement were the end supports and load points. Rollers were used at each support to allow symmetrical longitudinal deformations about the girder centreline and must have sufficient longitudinal displacement capacity. Each load point must accommodate vertical and lateral girder

displacements as well as cross-section rotation. As the greatest amount of deformation was expected to occur at mid-span, displacement and rotation values at mid-span were used as conservative estimates for movements at each load point. The pertinent displacements extracted from the model were:

- Lateral (horizontal) displacement at compression (top) flange at mid-span,  $\delta_h$
- Vertical displacement at tension (bottom) flange at mid-span,  $\delta_v$
- Twist of top flange at mid-span,  $\theta_z$
- Longitudinal displacement at bottom flange at end supports,  $\delta_z$

Figure 4-8 indicates where on the cross-section the abovementioned values were extracted.

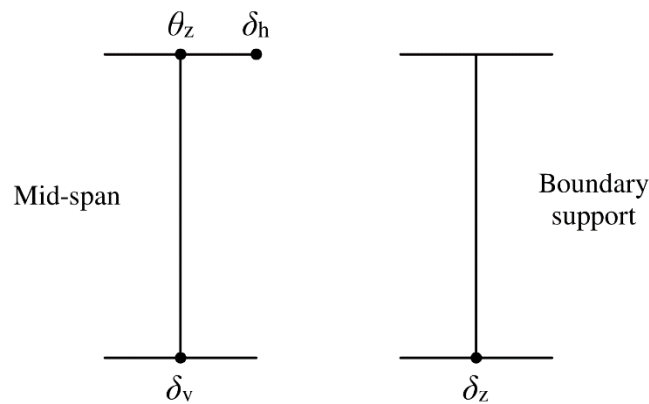


Figure 4-8: Measurement locations in FE analysis

Table 4-2 provides a summary of the displacements and rotations at buckling obtained from the FE model. Positive values of vertical displacement indicate downward movement; lateral displacement and twist are arbitrarily shown to be positive as the test set-up must accommodate buckling (and therefore lateral displacement and twist) in either direction; positive values for longitudinal movement indicate movement away from the girder centreline. The boundary conditions were modelled as pin-roller, whereas the actual supports were roller-roller, which may create slight discrepancies in the predicted longitudinal displacements. However, because the predicted longitudinal displacements were small (i.e., less than 5 mm at buckling), any slight increases in movement due to a roller-roller set-up can be easily managed. From the FE results,

the largest expected mid-span vertical displacement, lateral displacement, and twist at buckling were 57.0 mm, 73.1 mm, and 6.0°, respectively. The largest longitudinal movement at the end supports at buckling was 4.9 mm at the bottom flange, away from the girder centreline. These values were used to inform boundary condition and load mechanism design.

Table 4-2: FE results of displacements and rotations at buckling

Specimen ID	$L/r_y$	$I_y$ ( $\times 10^6$ mm <sup>4</sup> )	Mid-span			$\delta_{z, \text{roller}}$ (mm)	$\delta_{z, \text{pin}}$ (mm)
			$\delta_v$ (mm)	$\delta_h$ (mm)	$\theta_z$ (°)		
G6-470-32-2-p	79.7	549	57.0	25.1	2.5	4.0	4.9
G6-430-32-1-f	87.8	421	53.7	34.4	3.3	3.7	4.7
G6-430-32-1-p							
G6-300-32-1-p	131	143	40.4	73.1	6.0	2.4	3.7
G8-430-25-2-p	94.1	337	31.9	47.0	3.8	3.2	3.8
G8-390-32-2-p	102	314	31.7	53.6	4.0	3.0	3.7
G8-390-25-2-p	105	251	28.5	55.2	4.3	2.8	3.5
G9-360-32-3-f	109	247	24.6	53.6	4.2	2.4	3.2
G9-360-32-3-p							
G9-360-25-3-f	113	198	22.7	72.7	5.2	2.2	3.1
G9-430-25-3-f	92.0	337	27.3	54.1	4.3	2.9	3.5

The expected vertical and lateral displacement at buckling predicted by the numerical model varies between the test girders. In previous LTB experiments, vertical displacements were typically greater than lateral displacements at buckling (Fukumoto et al. 1980; Richter 1998), which is consistent with expectations as even a small amount of lateral displacement can cause instability and initiate buckling. However, the FE model predicted larger lateral displacements than vertical at mid-span for all test girders except for G6-470-32-2-p and the G6-430-32-1 pair. This trend seems to be related to slenderness ratio ( $L/r_y$ ), moment of inertia about the minor axis ( $I_y$ ), and

girder depth, as depicted in Figure 4-9 and Figure 4-10. When  $L/r_y$  and girder depth increase, the ratio of top flange lateral displacement to vertical displacement at buckling ( $\delta_h/\delta_v$ ) generally also increases, whereas increasing  $I_y$  results in lower  $\delta_h/\delta_v$  values. These parameters seem to affect out-of-plane stiffness and should be noted during testing and analysis of results. For reference, the load–displacement response of the test girders with the highest and lowest  $\delta_h/\delta_v$  values are shown in Figure 4-11, where  $P$  is the applied load at each load location. All the load–displacement curves from the numerical analysis can be found in Appendix D.

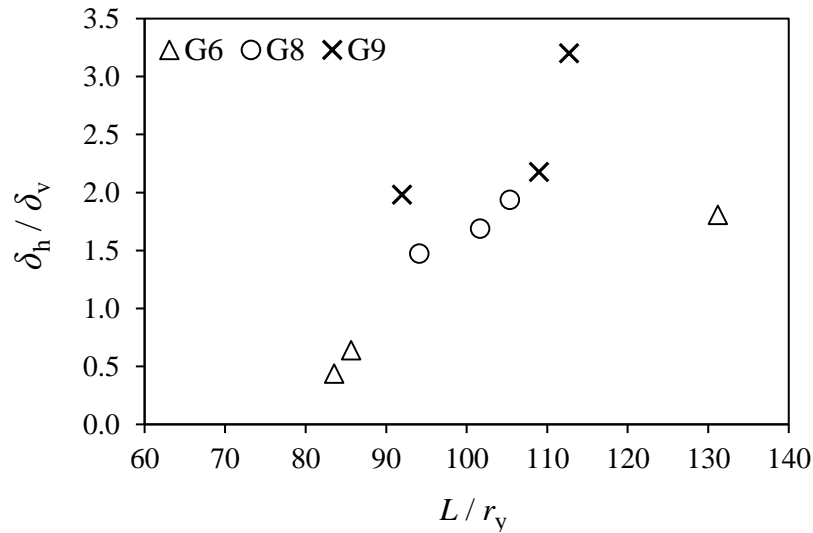


Figure 4-9: Ratio of lateral-to-vertical displacement at mid-span at buckling vs. slenderness ratio

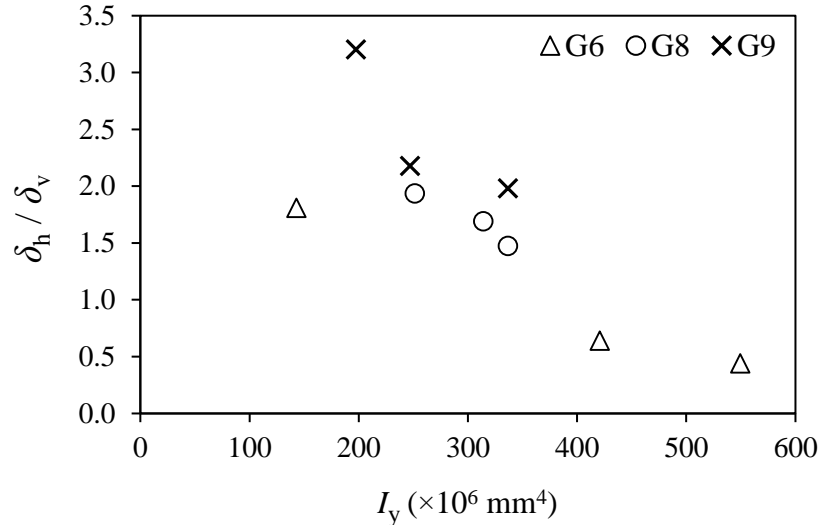


Figure 4-10: Ratio of lateral-to-vertical displacement at mid-span at buckling vs. moment of inertia about minor axis

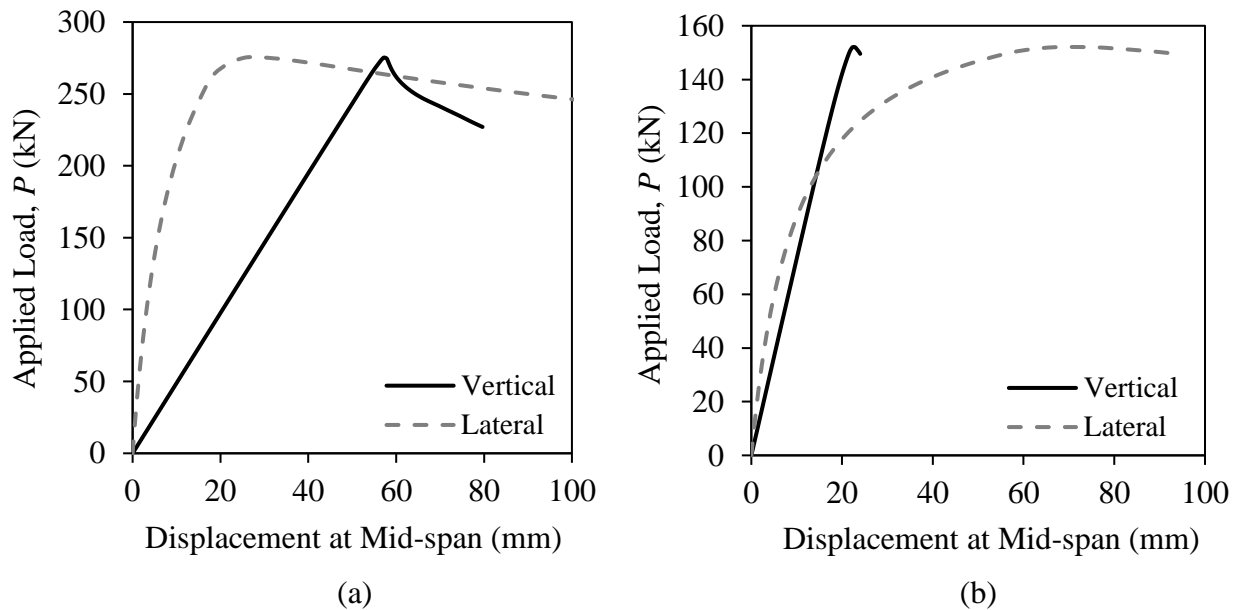


Figure 4-11: Load–displacement response from FE analysis: (a) G6-470-32-2-p and (b) G9-360-25-3-f

Table 4-3 summarises the FE predictions of buckling capacity; predictions from CSA S16-14 are provided for comparison, but were not corrected to account for top flange loading. As residual stresses were not modelled, the FE-predicted moment capacities are the same for each of the G6-430-32-1 and G9-360-32-3 girder pairs, which are nominally identical but have different cutting methods. Numerical simulations consistently predicted lower capacities than CSA S16-14,

though this is unsurprising since the model considers top flange loading, which is known to have a destabilising effect. Interestingly, the difference between predicted capacities appear to increase as girder depth increases.

As the FE model is predominately used for displacement and rotation predictions, these observations are not meant to comment on CSA S16-14’s adequacy. Rather, the FE capacity predictions serve to provide a check-point during testing—they offer insight on what the buckling capacities may be but are not used to make accurate predictions.

Table 4-3: Comparison of FE and CSA S16-14 predictions of test girder capacity

Specimen ID	$M_{FE}$ (kNm)	$M_{S16}$ (kNm)	% Difference
G6-470-32-2-p	2682	3405	25.0
G6-430-32-1-f	2322	3036	28.1
G6-430-32-1-p			
G6-300-32-1-p	1204	1793	41.2
G8-430-25-2-p	2125	3286	49.3
G8-390-32-2-p	2272	3513	48.6
G8-390-25-2-p	1740	2804	53.5
G9-360-32-3-f	1911	3197	59.8
G9-360-32-3-p			
G9-360-25-3-f	1483	2526	61.1
G9-430-25-3-f	2129	3414	55.3

## 4.2 Test Set-up

Based on the FE results of displacement and rotation, the test set-up was designed to accommodate the predicted girder movements without inducing undesired restraint to the test girders. A model

of the test set-up is shown in Figure 4-12. The test girder rests on elevated end supports; eight sets of gravity load mechanisms apply load through the top flange of the girder; lateral bracing is provided only at the beam ends. This section describes the design of the gravity load mechanism and end supports, including the safety measures implemented into the set-up.

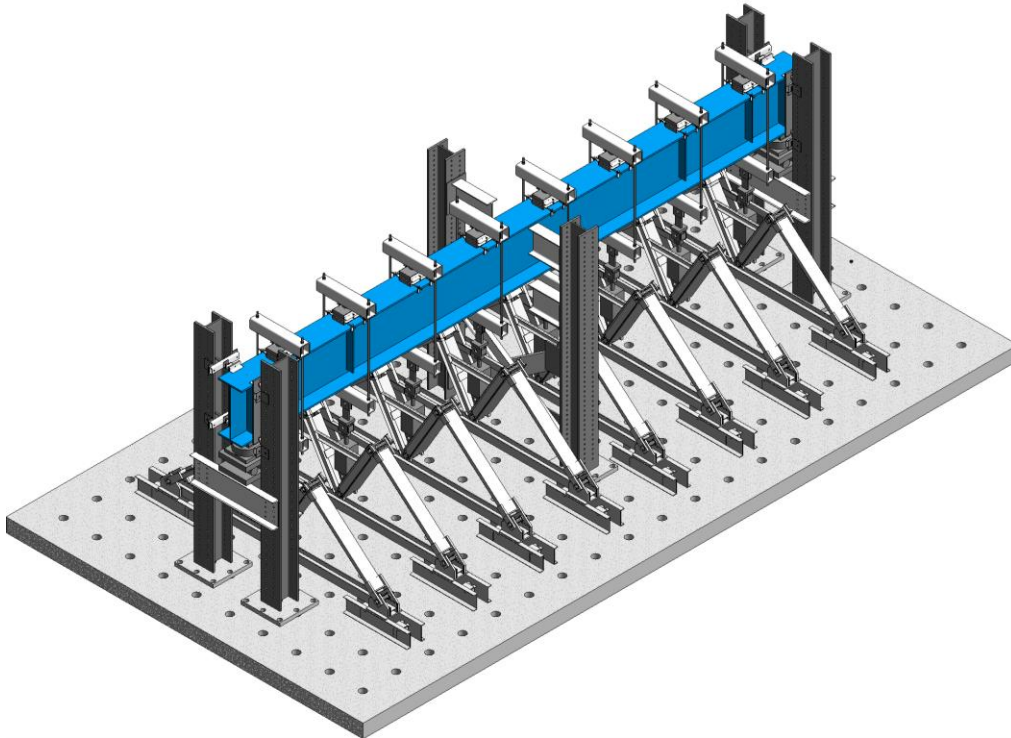


Figure 4-12: Model of experimental test set-up (test specimen shown in blue)

#### 4.2.1 Gravity Load Application

The gravity load mechanism comprises three components: (1) gravity load simulator, (2) hydraulic actuator, and (3) load collar, as shown in Figure 4-13. The components are attached to each other through pivot pin connections. At the start of the test, the hydraulic actuator is fully extended; as it retracts, it pulls on the load collar, which delivers a downward concentrated force to the top flange of the test girder. The vertical displacement of the girder is therefore accommodated by the retracting stroke of the hydraulic actuator. Girder twist and lateral movement are accommodated by the load collar and gravity load simulator, respectively. Details of the gravity load mechanism components are herein presented.

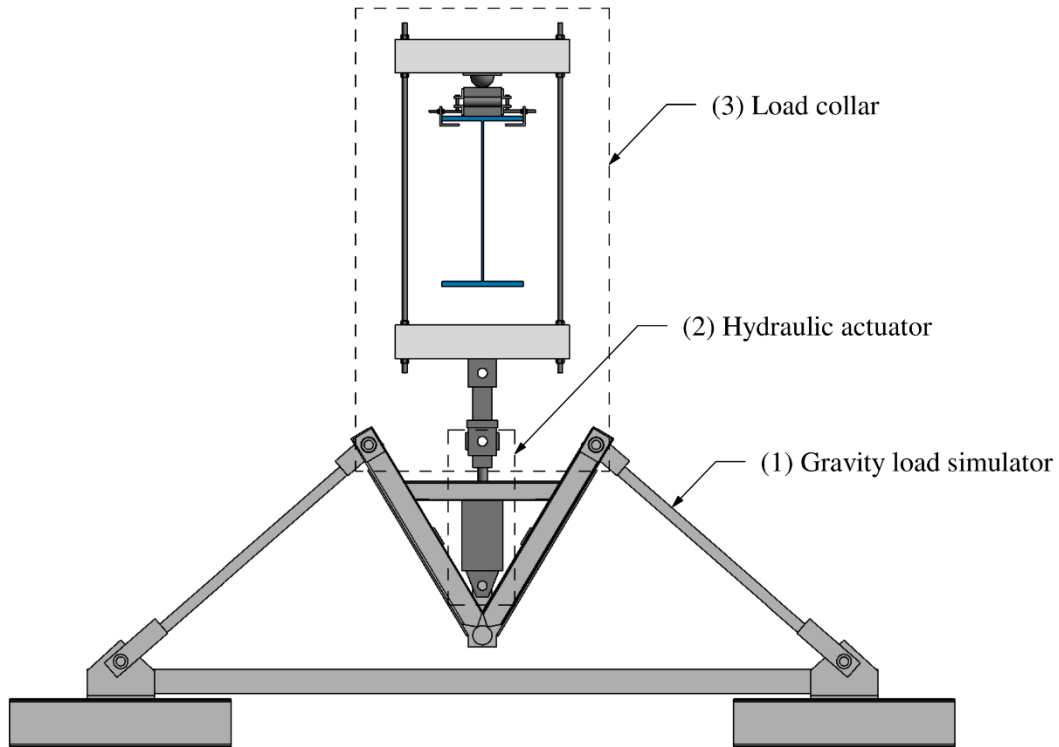


Figure 4-13: Components of the gravity load mechanism

#### 4.2.1.1 Gravity Load Simulator

A major challenge in conducting LTB tests is maintaining continuous vertical load application as the member undergoes free lateral movement. A potential solution used by previous researchers is laterally bracing the member at load points and inducing LTB in the unbraced segments between load points. However, this decreases the member's unbraced length and, as a result, much longer beams (and potentially smaller cross-sections) must be used to achieve LTB in the unbraced segment. It also introduces some (likely undefined) degree of restraint to the ends of the critical section due to its continuity with the adjoining segments of the member. The solution employs gravity load simulators (GLS), a pin-jointed mechanism designed to test structures that sway (Yarimci et al. 1967). The GLS can sway laterally from the equilibrium position in either direction without manual adjustments, while keeping the hydraulic actuator (and therefore load application) close-to-vertical, as shown in Figure 4-14. By using a GLS at each load point, it is possible to

apply continuous vertical load without lateral bracing, thereby achieving the 9.75 m (32 ft) unbraced length.

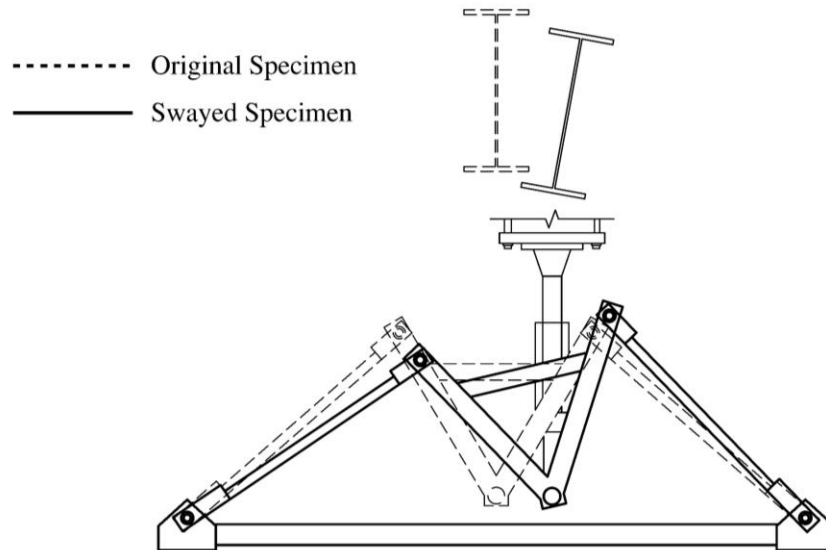


Figure 4-14: GLS maintains vertical load application as it sways laterally

In the set-up, the hydraulic actuator retracts as it exerts a downward pull force on the test girder, which results in an upward vertical load on the GLS at its connection with the actuator. A static analysis was conducted using SAP 2000 (CSI 2015) to determine the capacity of the as-built GLS in its equilibrium and maximum swayed configurations. Allowing for the fact that the GLS must remain elastic during testing, the in-plane capacity was determined to be 380 kN, which was verified with hand-calculations using beam-column design equations from CSA S16-14. The out-of-plane buckling capacity of the GLS was then calculated by following the procedure outlined by Yarimci et al. (1967) but was found to be much higher than the in-plane capacity. The GLS' in-plane load capacity of 380 kN was identified as the limiting factor in the entire test set-up capacity. Since Driver et al. (1997) successfully loaded the same GLS up to 360 kN, the maximum allowed load for the tests was limited to 360 kN, to provide an additional margin of safety.

The displacement capacity of the GLS is approximately 400 mm in either direction, which is well above the expected maximum mid-span lateral displacement at buckling of 73.1 mm. As 400 mm

of lateral movement was deemed unsafe and lateral displacement can increase rapidly after buckling, safety stops to ward against excessive movement were necessary. As such, columns located on either side of the test girder were installed at mid-span (where the largest girder deformations are expected); a stub cantilever beam was then mounted to each column and oriented toward the test girder at the approximate height of the girder's top flange to limit top flange lateral displacement in either direction. The mid-span bracing assembly is shown in Figure 4-15. The cross-braces pictured were added for increased column stiffness, while the stub beam near the bottom flange of the girder was used for mounting instrumentation, as discussed in Section 4.3. One of the beams installed at the top flange height served a dual purpose, as it was used for limiting lateral displacement as well as mounting instrumentation. In the finalised configuration, the lateral displacement was capped at 140 mm for the widest flange and 225 mm for the narrowest flange. Their respective predicted lateral displacements at buckling were 25.1 mm and 73.1 mm.

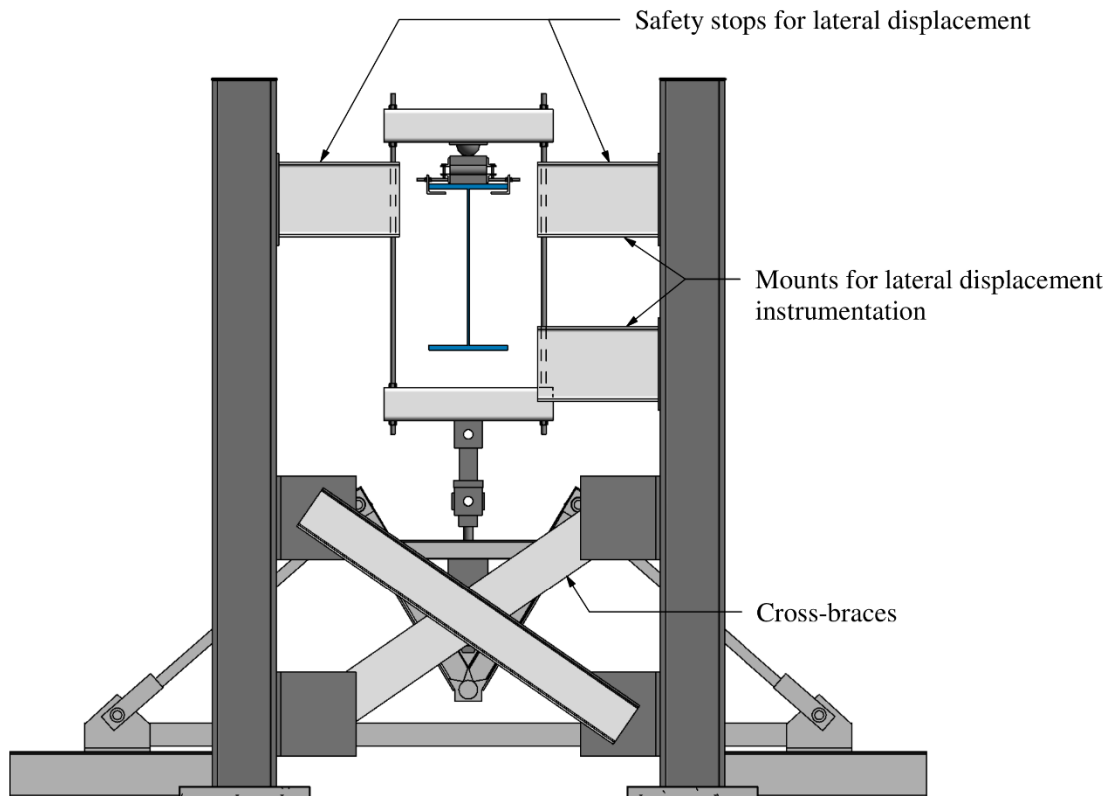


Figure 4-15: Mid-span bracing to prevent excessive lateral displacement

#### 4.2.1.2 Hydraulic Actuator

Connected to each GLS was a hydraulic actuator, which was used to generate the concentrated load applied to the test girders. The eight actuators were linked to a single manifold and used a common control system, which meant they were hydraulically dependent. Therefore, it was essential for them to have identical bore and piston diameters to ensure they exerted the same force at a given pressure. At the maximum allowable operating pressure of 21 MPa (3000 psi), the actuators' load capacity was 385 kN in pull and 514 kN in push, though only the pull capacity was important for the tests. The maximum expected vertical displacement at buckling at mid-span was 57.0 mm, which is easily accommodated by the 150 mm stroke of the hydraulic actuator.

#### 4.2.1.3 Load Collar

The load from the hydraulic actuator was applied to the test girder through a load collar, as shown in Figure 4-16. The main portion of the collar comprised a load box around the girder; two HSS members of steel grade 350W formed the top and bottom member of the load box, while Grade 8 threaded rods connected the HSS members. Also part of the collar was a rotational hemisphere, which was bolted to the top HSS of the load box to accommodate cross-section twist. The hemisphere bore on a set of rollers, which allowed for longitudinal movement. This was particularly important at the beginning of each test, as the set-up underwent initial longitudinal alignment to ensure the load applied at the top flange was centred above the hydraulic actuator.

To prevent the rollers from sliding off when the girder undergoes large twist, adjustable tabs were used to secure the rollers' position on the flange, as shown in Figure 4-16. Steel angles were fitted to the top and bottom roller plates, and connected to each other with a bolt, as shown in Figure 4-17. When the bolt was tightened, the top and bottom roller plates could not slide and the roller assembly was effectively prevented from displacing, which was useful during the test set-up process. When each load collar was fully assembled, the bolt was loosened to release longitudinal movement of the roller assembly, but slotted holes in the upper angle prevented excessive displacement during the test. A sacrificial piece of machined steel plate (not depicted in Figure 4-16) was used between the hemisphere and roller to prevent bearing deformations in the top roller plate.

Lastly, a yoke was welded to the bottom HSS member, which allowed a tension rod to be connected to the load box through a pivot pin. The tension rod completed the load collar assembly and served to connect the load collar to the hydraulic actuator; the extra length provided by the tension rod was necessary to ensure the bottom HSS member cleared the top of the GLS.

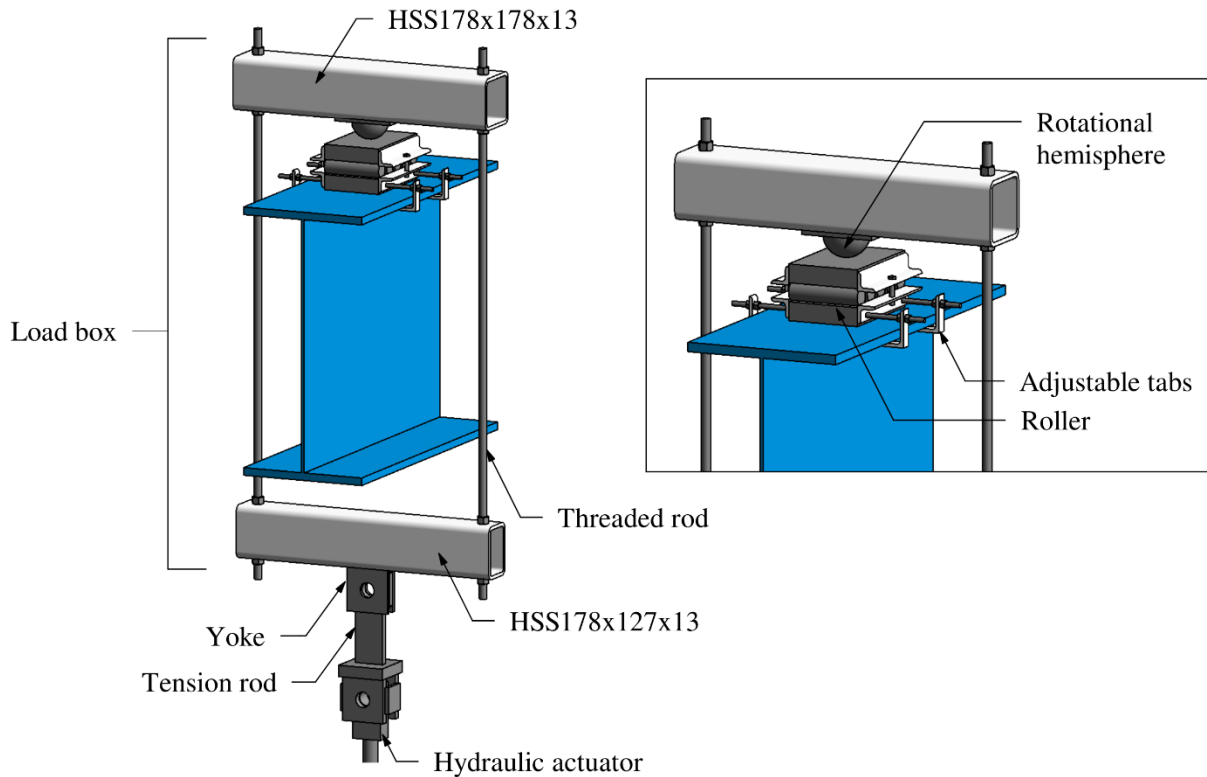


Figure 4-16: Load collar components



Figure 4-17: Slotted angle connection in roller assembly

In the load collar assembly, the load box was designed to remain square while the girder rotated about the hemisphere over the course of a test. Though the hemisphere had large rotational capacity, a maximum allowed rotation of  $9^\circ$  was chosen to limit the possibility of slippage between the hemisphere and roller. As the FE results predicted a maximum mid-span rotation of  $6.0^\circ$  at buckling, the  $9^\circ$  capacity was deemed acceptable. The width of the load box was therefore designed to accommodate all girders at a  $9^\circ$  rotation. Because the point of rotation was the contact point between the hemisphere and the roller (or, in actuality, the sacrificial steel plate), the girder was effectively loaded above its top flange. The combined height of the roller assembly and sacrificial steel plate resulted in a load height of 178 mm above the top surface of the top flange.

All components of the load collar were designed to remain elastic up to an applied load of 360 kN from the hydraulic actuator, with sufficient rigidity to minimise (elastic) deformations during loading. Flexural collar members were designed using the yield moment as the ultimate capacity rather than plastic moment. Yield line theory was employed to ensure the thin wall of the HSS members would not yield from the downward force at the yoke and from the bearing of the nuts at the connections with the threaded rods. As yield line theory is an upper-bound approach, an additional 10% reduction factor was applied.

Further considerations were made to ensure a conservative design, which include:

- adding a load eccentricity of 15%;
- meeting a minimum capacity-to-demand ratio of 1.3 for flexure, shear, and axial force (resistance factors from CSA S16-14 were included in determining the capacity); and
- using elastic beam deformation and axial elongation theory to confirm designed collar members would not deform excessively.

#### 4.2.1.4 Summary

A gravity load simulator, hydraulic actuator, and load collar constitute the gravity load mechanism. Combined, they accommodate vertical displacement, lateral movement, and cross-section twist of the test girder at each load point, as summarised in Table 4-4. The fabricated assembly is shown in Figure 4-18. The displacement or rotation capacity of the designed mechanisms are well above the predicted movements at buckling from the numerical model, which was done in part to observe the girders’ post-buckling response. Referencing the load–displacement curves from numerical simulations, an estimated 1.1 times the vertical displacement and 1.5 times the lateral displacement at buckling captures an adequate amount of post-buckling behaviour. This results in vertical and lateral displacement demand predictions of 62.7 mm and 110 mm, respectively, which remains within the mechanisms’ displacement capacities. Post-buckling response aside, LTB is a stability-related failure that is inherently difficult to predict and therefore necessitates generous safety margins.

Table 4-4: Displacement demand and capacity

	Maximum Mid-span Displacement at Buckling from FE Results	Allowable Displacement in Designed Load Mechanism	Corresponding Component of Load Mechanism
Vertical Displacement	57.0 mm	150 mm	Stroke of hydraulic actuator
Lateral Displacement	73.1 mm	140 – 225 mm	Gravity load simulator
Twist	6.0°	9°	Rotational hemisphere



Figure 4-18: Fabricated gravity load mechanisms

#### 4.2.2 End Conditions

The end supports were another critical aspect of the test set-up and identical configurations were used at the two ends of the test girder. As the girders must be positioned above the GLS, elevated end supports were created by back-to-back channels spanning between two stocky columns. On the channels rested a set of rollers, followed by a load cell, then a knife edge, and finally the test girder, as pictured in Figure 4-19—this formed the simply-supported in-plane boundary condition. As rollers were used at both supports, they were fitted with a slotted connection that limited longitudinal movement to 65 mm in either direction, which easily accommodated the expected maximum longitudinal displacement at buckling of 4.9 mm. Furthermore, a chain was fastened across the two columns at both ends to prevent the girder from excessive longitudinal movement.

To achieve the torsionally pinned boundary condition, lateral displacement and twist must be restrained while allowing the girder to warp. Four lateral braces at each end support were employed and bore against the top or bottom flange tips, thereby preventing lateral movement and twist, as shown in Figure 4-20. As the braces were also equipped with rollers, the girder was free to displace

longitudinally and warp. To provide a larger bearing area for the rollers, plates that hung off either side of the girder were used. Additionally, by employing a threaded rod in the brace design, the overall length of the brace could be adjusted, which served multiple purposes: (1) to ensure the brace bore firmly against flange tip, (2) to centre the girder position on the knife edge assembly, (3) to align the girder so that its web was vertical at the end supports, and (4) to accommodate various flange widths. The lateral braces were designed using Appendix 6 of AISC 360-16 (AISC 2016), which prescribes both strength and stiffness requirements. Strength governed, and the braces were designed to resist brace forces of 117 kN.

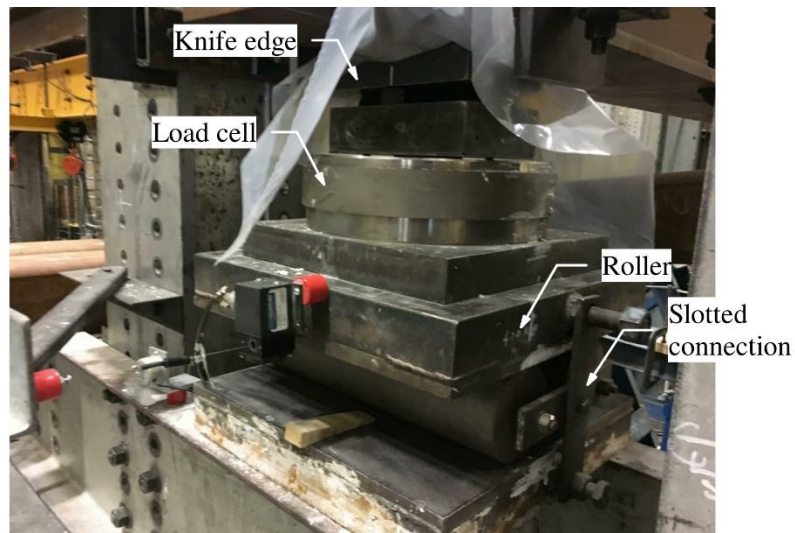


Figure 4-19: Girder end support

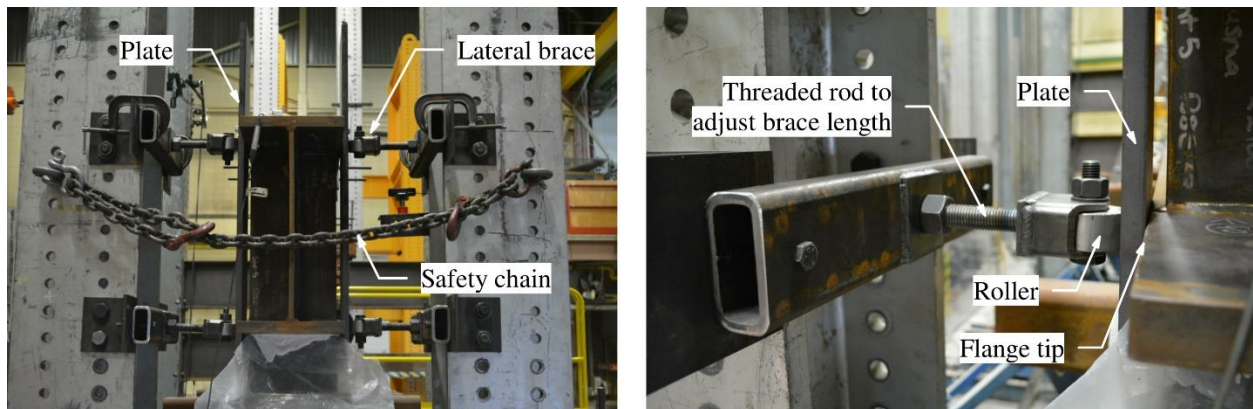


Figure 4-20: Lateral bracing at boundary support

### 4.3 Instrumentation

A schematic diagram depicting the arrangement and types of instrumentation used to measure forces, displacements, rotations, and strains is shown in Figure 4-21; the columns and beams at the end supports and mid-span have not been shown for image clarity. At the girder end supports, Strainsert load cells with 2200 kN capacity were used to measure the reaction forces. Load cells fabricated with biaxial strain gauges and rated to 3% strain were attached to each of the eight tension rods to record the force at each load point. The redundancy in load measurement affirms accuracy of the recorded data. Two-point calibration was performed on all load cells using uniaxial load frames; the end support load cells were calibrated in compression, while load cells at the load points were calibrated in tension.

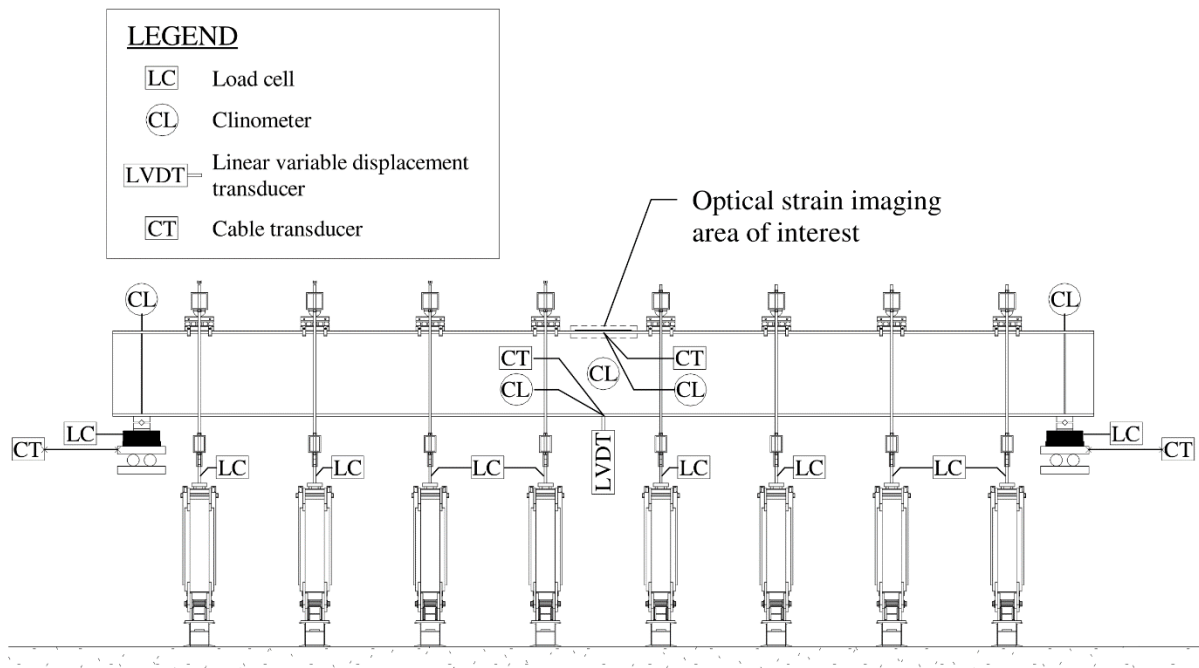


Figure 4-21: Instrumentation

Rotation and displacement measurements were recorded only at the mid-span and the supports, as they were deemed the critical locations. Clinometers were installed at the top flange, web, and bottom flange at mid-span to measure cross-section rotation (twist), while a clinometer to measure major-axis rotation was mounted to the top flange at both ends of the girder. At mid-span, top and

bottom flange lateral displacements were individually measured as they were expected to be significantly different. Measuring lateral displacement proved to be a challenge; because vertical and lateral displacement and twist occur concurrently, it was necessary to find a method of uncoupling the movements to isolate lateral displacement. An innovative uniaxial translation device, the Miller–West Glider, was designed and fabricated in the laboratory for this purpose. Miller–West Gliders were mounted to the mid-span safety stop beams at the top and bottom flanges (discussed in Section 4.2.1.1), as shown in Figure 4-22.

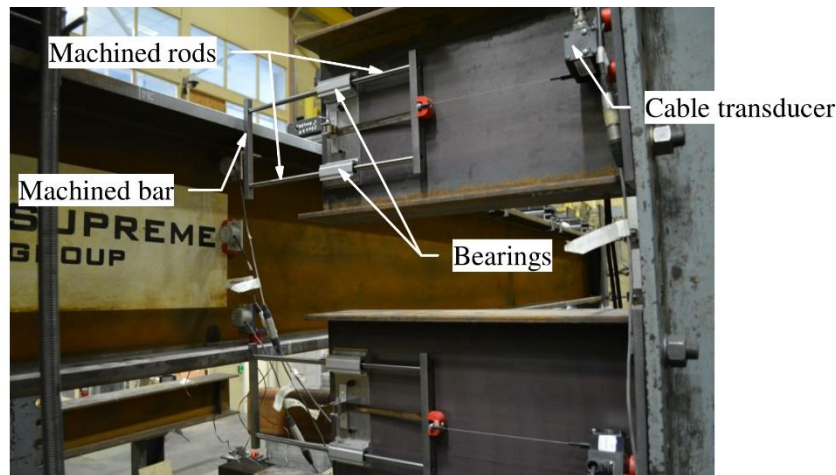


Figure 4-22: Flange lateral displacement measurements at mid-span using the Miller–West Glider

Each Miller–West Glider was equipped with a spring-loaded bar that rested against the girder flange tip; the spring was sufficiently flexible to effectively eliminate friction between the bar and flange. The bar was attached to two machined rods that were held in place by bearings, which provided a horizontal track for the rods to slide through easily. Hence, the bar could only move in the lateral direction. The span of the bar could accommodate 190 mm of downward vertical displacement and had a lateral displacement capacity of 135 mm in either direction. Therefore, even as the girder rotated and displaced vertically and laterally, only the lateral component of the movement was captured. Lateral displacements of the test girders could then be recorded by connecting a cable transducer to the bar. It should be noted that lateral displacements could only be measured up to 135 mm, whereas 140 mm of lateral movement was permitted by the test set-

up. As the only consequence would be potentially losing 5 mm of post-buckling displacement behaviour, it was deemed acceptable.

To obtain the vertical displacement of a girder at mid-span, it was adequate to measure only at the bottom flange, for which a linear variable displacement transducer (LVDT) with a stroke of 150 mm was used, as pictured in Figure 4-23. As there were strain gauges on the bottom flange (discussed later in this section), a thin plate was mounted to sit slightly below the bottom flange to provide a surface for the LVDT to bear on that would not interfere with the strain gauges. Longitudinal displacements at each end of the girder were measured using cable transducers. For ease, the cable transducers were mounted to the top roller plate; the actual longitudinal measurement at the bottom flange or centroid of the girder could then be calculated using principles of geometry.

All displacement and rotation instruments were calibrated before first use; displacement instruments were furthermore verified immediately before each test. Electrical signals from all aforementioned sensors were digitised using the HBM MGCplus data acquisition system and processed with the catmanAP V4.1.2 software to provide real-time updates of measurements at one second intervals. Live feedback of load, displacements, and rotations from the instrumentation was crucial for the successful completion of each test.

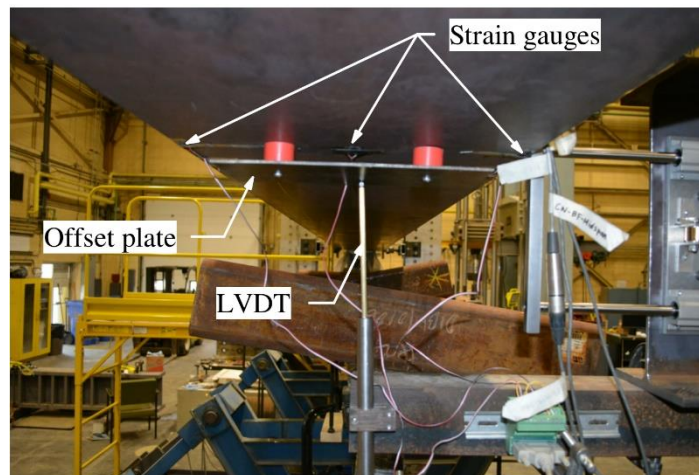


Figure 4-23: Vertical displacement measurement at mid-span

To understand the stresses at mid-span (where the girder is expected to yield) and determine the first point of yield, load-induced surface strains were measured. At the top flange, strains were measured using a Vic-3D 2010 digital imaging correlation system from Correlated Solutions Inc. The system can provide measurements of shape, displacement, and strain by tracking the relative movements of unique points in a speckle pattern. Points are tracked through simultaneous images taken by a pair of cameras focused on a common area of interest at set time intervals. An area covering the top flange width and a length of 600 mm was painted white then speckled with black dots to provide a high-contrast pattern with approximately 50% black and white coverage, as shown in Figure 4-24. At the bottom flange, strain gauges were used in lieu of optical strain imaging. Because the bottom flange is in tension, yielding is likely to occur at either the flange tips or the web–flange junction, whereas the compression (top) flange behaviour is not as easily predicted. Three strain gauges—one at each of the aforementioned yielding locations—were deemed adequate for characterising yielding behaviour of the bottom flange and are visible in Figure 4-23.

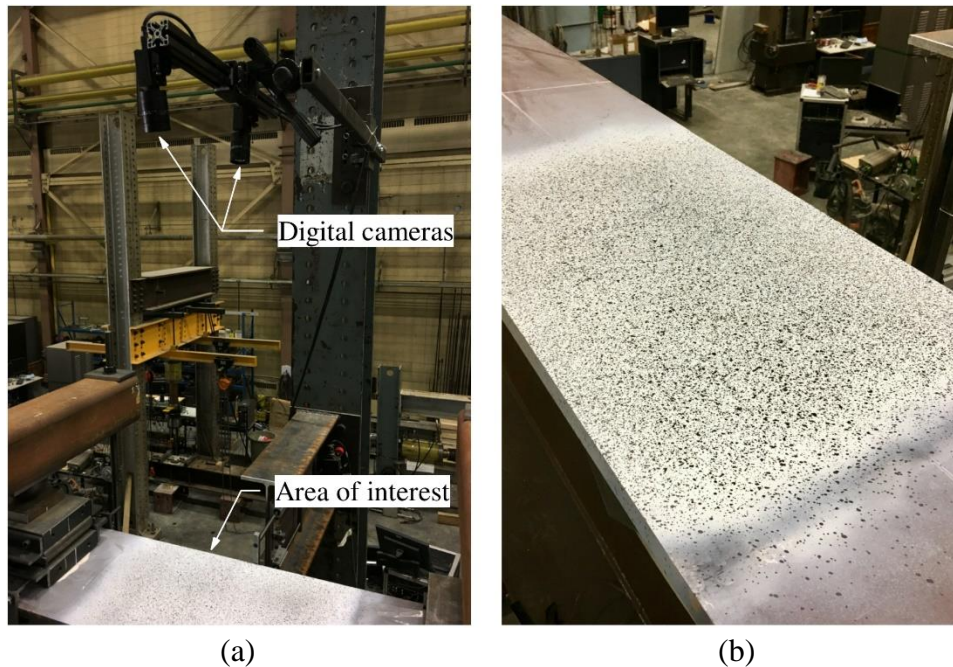


Figure 4-24: Optical strain imaging set-up (a) overview, and (b) typical speckled area of interest at mid-span

## 4.4 Test Procedure

The preparation for each individual test began with lifting and placing the test girder on the end supports with a crane. The lateral braces were then used to centre the bottom flange of the girder on the supports. With the girder centred at both ends and the bottom flange secured laterally, the girder web was plumbed using lateral braces to adjust the top flange. To ensure the bottom flange sat flush on the knife edge, a gypsum cement plaster (known commercially as Hydro-Stone®) was used. The girder was then aligned longitudinally so that the bearing stiffeners were centred above the end supports. At this time, the self-weight of the girder was recorded using the load cells at the end supports. Rollers were then lifted and positioned on the top flange of the girder at the eight load points, again using Hydro-Stone® to create flush contact between the roller and girder. Crosshairs were marked on the girder beforehand to indicate the location of each load point and were used to align the rollers. The remainder of the load collars were then sequentially lifted into place. Squareness of the load box was achieved by ensuring the distances between the ends of the top and bottom HSS were equal. To ensure the collar did not impose an applied load on the girder, the nuts that connect the bottom HSS with the threaded rods were barely snug. The system self-weight was then recorded to account for dead load from the rollers and collars.

As pin connections were used between the GLS, hydraulic actuator, and load collar, a method for keeping the mechanisms vertical and stable (when there is no load in the system) was required. A simple solution was devised, where timber pieces on either side of the tension rod were clamped to the GLS (visible in Figure 4-18). During the set-up process, it was also important to keep the GLS stable and centred for safety and alignment purposes. A turnbuckle system was welded to each GLS for this reason, as shown in Figure 4-25; the turnbuckle adjusts the lateral position while also preventing any slight lateral momentum that may cause the apparatus to sway suddenly from its centred position. Both the turnbuckles and timber pieces were removed at 10% of the predicted buckling load for each test, which was considered a large enough force to keep the gravity load mechanism vertical but small enough that lateral girder movement was insignificant.

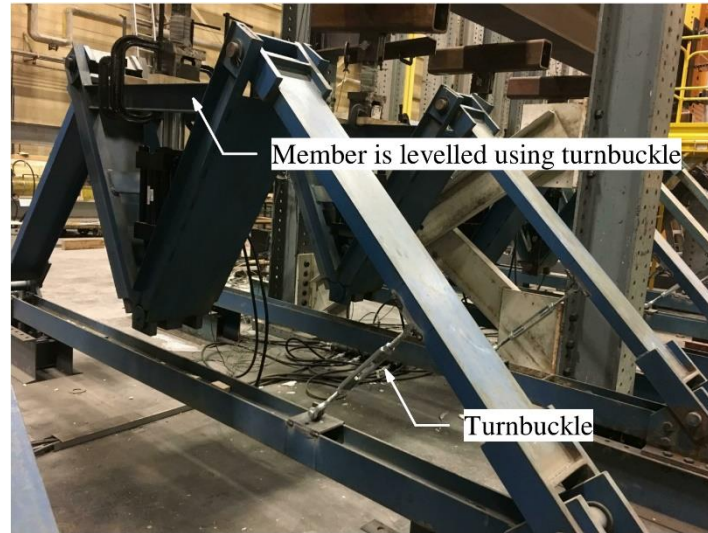


Figure 4-25: Turnbuckle system for each GLS

The loading was controlled manually, with a loading rate of 0.5 to 1 kN/s of the total applied load. However, a pseudo-displacement-controlled method was implemented near the onset of buckling. By monitoring the load vs. lateral displacement graph, buckling could be anticipated. When lateral displacements began to increase noticeably, the operator of the hydraulic system slowed the loading rate. Once the lateral displacement curve began to plateau, this signalled the buckling point and the load was held steady to allow the girder to further deform. At this point, the hydraulic system was configured to allow pressure to be very slowly released from the system (to decrease the applied load) as the girder's load capacity decreased. Once the desired amount of post-buckling response was attained, unloading began—this typically corresponded to reaching the maximum allowed top flange rotation of  $9^\circ$  or a lateral displacement of approximately 80 mm. When approximately 10% of the buckling load remained in the system, the load was held steady to re-install the turnbuckles and timber pieces, after which the system was fully unloaded.

Given the scale of the test and unpredictable nature of stability testing, safety measures—in addition to those considered during test set-up design—were of foremost importance. A safety hazard and risk assessment report was completed for all laboratory tasks related to testing, including preparation of the test girders and set-up of the test bed. During testing, no one was allowed near the set-up (aside from those removing turnbuckles and timber pieces at the beginning

of the test and replacing them towards the end). Caution tape was used to cordon off the test area and a Plexiglas® shield separated the test set-up and the hydraulic control system (where the operator presided and observers were stationed).

## 5 RESULTS AND DISCUSSION

This chapter presents the results of the experimental testing programme described in Chapter 4, with the overall aim of improving the understanding of lateral–torsional buckling (LTB) behaviour in modern welded girders. The obtained capacities and displacement behaviour of the test girders are analysed and influential parameters identified in the test specimen selection criterion are considered in the discussion. The measured residual stress distributions, combined with surface strain measurements, are used to examine the stresses at mid-span throughout the test. The experimental results are then compared to predictions from design provisions, with a primary focus on CSA S16-14 (CSA 2014a). The findings are used to discuss the adequacy of the Canadian provisions for LTB resistance and potential experimental errors are acknowledged.

Though the test matrix considers 11 specimens, only seven tests were completed for this research project due to time constraints; the results are included in this report. The seven completed tests comprise the G6 and G8 girder series, which were all Class 1/2 sections. The remaining four test girders, all of Class 3, will be tested in the I.F. Morrison Structural Engineering Laboratory at the University of Alberta and presented in a future report.

### 5.1 Girder Capacity Results

The overall girder behaviour observed was consistent with typical LTB failures. Prior to reaching the buckling load, there was generally little lateral displacement and cross-section rotation. Upon buckling, the girder’s strength slowly decreased as top flange lateral displacement and rotation increased steadily. Girders were unloaded after approximately 80 mm of lateral displacement or 9° of rotation; sufficient post-buckling behaviour was recorded at these displacements for all tested girders. Table 5-1 summarises the maximum loads and moments obtained from the tests as well as the normalised moment capacities. Figure 5-1 presents the obtained moment resistances versus slenderness ratio; a horizontal line at an  $M_{\max}/M_p$  value of 0.67 marks the boundary between elastic and inelastic LTB, per CSA S16-14’s definition. The points at which the maxima occur are considered the buckling points and therefore the presented values are the buckling loads and moments of each girder. The reported load was determined by averaging the eight readings from

the load cells located at each load point; the differences between load readings were typically no more than 2 kN. The reported maximum moment considers these differences and is calculated from the actual shear diagram for each test. The self-weight of the girder and the eight load collars (which weighed approximately 11.8 kN) were also accounted for in the moment resistances reported in Table 5-1. To calculate the plastic moment, actual cross-section dimensions and yield stresses (flange and web differentiated) were used. The test capacities are herein discussed in relation to the obtained range of inelastic behaviour, geometric properties, and effect of cutting method, which were considered in the test specimen selection criteria. The effect of section class will be examined upon completion of the Class 3 sections (i.e., the G9 series).

Table 5-1: Summary of girder capacities from experimental testing

Specimen ID	Maximum Load, $P_{\max}$ (kN)	Maximum Moment, $M_{\max}$ (kN·m)	$M_{\max}/M_p$
G6-470-32-2-p	277	2756	0.85
G6-430-32-1-p	236	2349	0.78
G6-430-32-1-f	237	2359	0.79
G6-300-32-1-p	132	1327	0.62
G8-430-25-2-p	188	1877	0.52
G8-390-32-2-p	263	2619	0.67
G8-390-25-2-p	188	1869	0.56

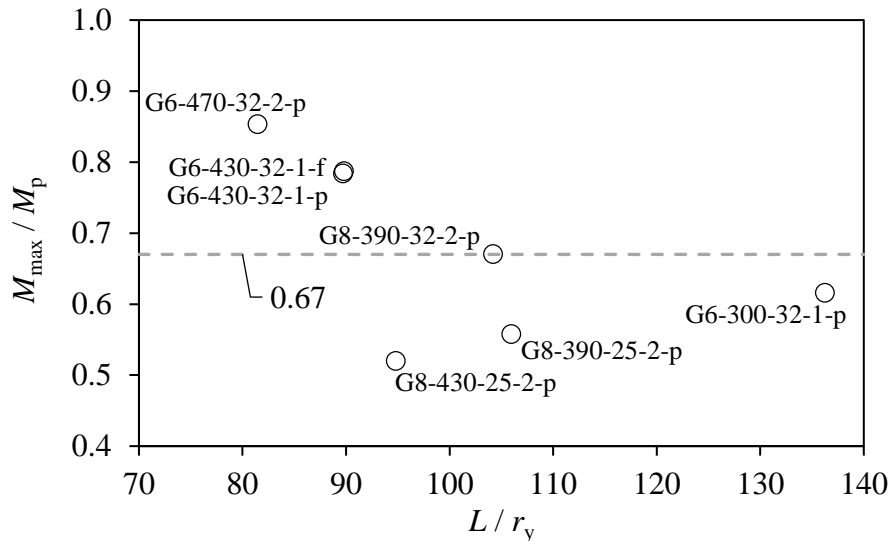


Figure 5-1: Moment resistance vs. slenderness ratio

### 5.1.1 Obtained Range of Inelastic Behaviour

The test girders were selected to cover the entire spectrum of inelastic behaviour, with an expected  $M_{max}/M_p$  range of 0.69 to 0.92. However, the actual range obtained was considerably lower and fell between 0.52 and 0.85. A large contributing factor was the load height effect; as girders were loaded 178 mm above the top flange, there was a significant destabilising torque that reduced LTB resistance. At the time of test specimen design, the loading configuration was not finalised and the load height effect was not anticipated to be as significant as it was. As a result, it appears that only four of the tested specimens were in the inelastic range defined by CSA S16-14 of  $0.67 < M_{max}/M_p < 1.0$ ; the remaining three specimens are classified as elastic LTB, as their  $M_{max}/M_p$  value fell below 0.67. While these limits give general guidelines of LTB behaviour, further analysis of the stresses in the girders is required to assess whether inelastic LTB occurred and is discussed in Section 5.3.

### 5.1.2 Effect of Geometric Properties

During test matrix development, cross-sectional properties were considered by examining the effect of cross-section dimensions—flange width, flange thickness, section depth, and web thickness—on LTB resistance. This was a simplistic approach suitable for selecting test

specimens, but analysis of the test results must consider that changing cross-section dimensions also affects other cross-sectional properties, such as  $I_y$ ,  $C_w$ , and  $J$ . Also, as LTB is a complex behaviour, it is difficult to decouple and assess the effect of a single cross-section parameter on LTB resistance. Therefore, parameters that encapsulate critical properties for defining LTB resistance should instead be considered for the analysis. The selected parameters were  $EI_y GJ$  and  $\left(\frac{\pi E}{L}\right)^2 I_y C_w$ , which are representative of the St. Venant torsional stiffness and warping stiffness, respectively; the influence of weak axis flexural stiffness ( $EI_y$ ) is also included in both parameters. As these parameters are derived from the theoretical critical buckling moment,  $M_{cr}$ , they are known to affect LTB resistance, albeit in the elastic domain.

Figure 5-2 and Figure 5-3 show relationships between moment resistance and the selected stiffness parameters. For the G6 series, increasing St. Venant torsional stiffness and warping stiffness were both found to increase moment resistance, which is consistent with expectations; moreover, the relationship is approximately linear. However, in the G8 series, clear trends were not observed. Though G8-430-25-2-p had the largest warping stiffness in the G8 series, it exhibited the lowest  $M_{max}/M_p$  value; the trend, however, for the St. Venant stiffness parameter is similar to that of the G6 series with the G8-430-25-2-p capacity still slightly low. The low  $M_{max}/M_p$  of this girder may be attributed to relatively large initial geometric imperfections, as discussed in Section 5.2.2.2.

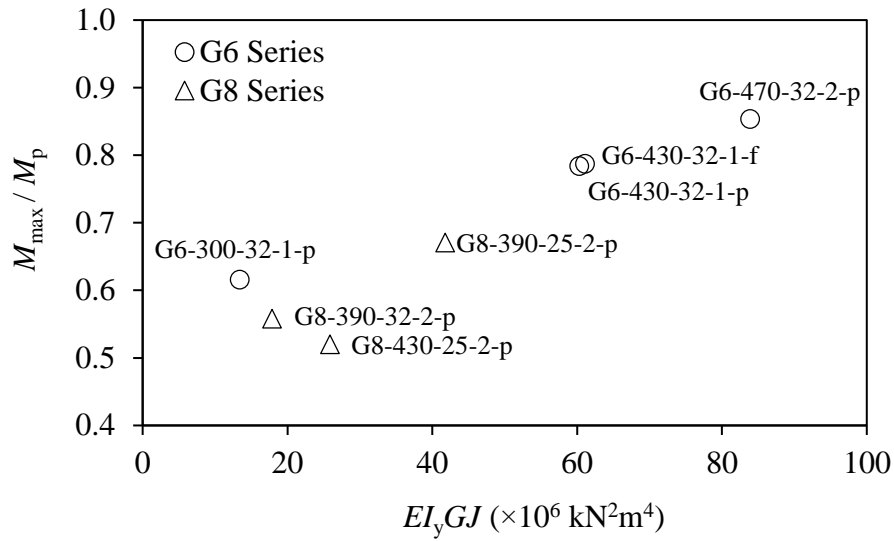


Figure 5-2: Moment resistance vs. St. Venant torsional stiffness

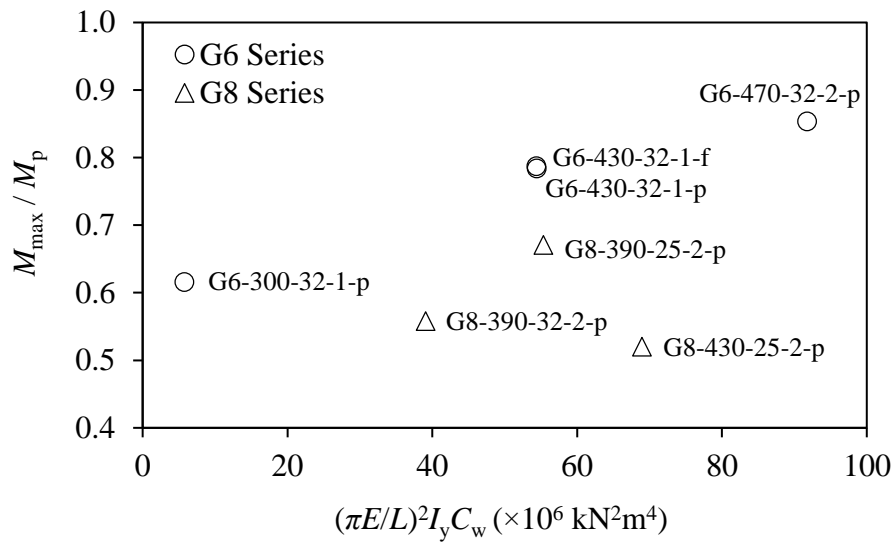


Figure 5-3: Moment resistance vs. warping stiffness

### 5.1.3 *Effect of Cutting Method and Residual Stresses*

The effect of cutting method can be examined by comparing G6-430-32-1-p and G6-430-32-1-f, which have identical nominal cross-section dimensions, but the former was plasma-cut and the latter flame-cut. Their experimental moment resistances were almost identical—within 0.5%—which indicates that the cutting method did not have an observable effect on LTB resistance. To understand these results, the measured residual stresses, as presented in in Section 3.4, must be considered. The mean residual stresses measured at the flange tips were -23 MPa and 10 MPa for G6-430-32-1-p and G6-430-32-1-f, respectively, where positive denotes tension and negative compression. In Chernenko and Kennedy’s (1991) simplified model for flame-cut girders, tensile residual stresses of  $0.7F_y$  are predicted at the flange tips, which corresponds to 243 MPa (using the measured flange yield stress) and is significantly larger than the measured residual stress of 10 MPa for G6-430-32-1-f. Well-established residual stress models for plasma-cut girders are not available, but previous research has indicated that plasma-cutting results in tensile stresses at the flange tips (Arasaratnam 2005), which is contrary to the compressive stresses observed in G6-430-32-1-p. However, for both G6-430-32-1-f and G6-430-32-1-p, the measured stresses are considered small and likely not significant enough to cause a marked difference in LTB resistance between them, which may explain the nearly identical experimental capacities.

While cutting methods that induce significant heat are expected to result in tensile residual stresses at the cut edges, the subsequent welding process alters the residual stress distribution further. Specifically, the welding results in a tensile stress spike at the web–flange junction, which must be compensated by compressive regions in the other portions of the plate. It is likely that the plasma-cut flange plates initially had tensile stresses at the cut edges but were altered to compressive stresses by the welding process to equilibrate stresses in the section. For the flame-cut girder, a similar explanation can be used, though small tensile residual stresses were observed instead of compressive ones. As flame-cutting typically results in larger tensile stresses at the flange tips than plasma-cutting (Arasaratnam 2005), it is reasonable that alteration of stresses due to welding could result in small tensile stresses at the flange tips. This would suggest that the model by Chernenko and Kennedy (1991) over-predicts the beneficial effect of tensile flange tips in flame-cut girders for modern welded steel girders studied here.

The small stress values observed at the flange tips could also be attributed to the width of the strips used in the sectioning method. Yang et al. (2018) measured residual stresses for flame-cut steel plates and used sectioning strips of 11 mm wide near the cut edges; they obtained tensile stresses ranging from  $0.25F_y$  to  $0.45F_y$ . In comparison, the measured values from Unsworth et al. (2019) using 30 mm strips correspond to  $0.03F_y$ . As the mean stress is measured in each strip, it is possible that the 30 mm width was too large to capture the tension residual stress spike at the flange tips (i.e., the strip may have included compressive stresses as well). There are ongoing discussions to potentially reduce the width of the sectioning strips near the flange tips for the remaining test specimens to assess this effect. However, even if the peak stress is higher than that measured, the width of the tension zone would be narrow (less than one-half of the strip width due to the steeper stress gradient near the tip) and may not have a large effect on LTB capacity.

## 5.2 Girder Displacement Results

Girder displacement behaviour is a crucial aspect of LTB; during the tests, displacements were measured at mid-span—where first yield was expected to occur—and at the end supports. The sign convention for imperfection measurements was similarly used for displacement measurements during the test and the cardinal directions as they relate to the tested configuration were employed for reference, as shown in Figure 5-4. While the sign convention is useful for understanding the directions of movements, absolute values were used for mean calculations, ranges, and other applicable contexts, where magnitude is of concern rather than direction. The sign convention is:

- positive vertical displacement is downward;
- positive lateral displacement is eastward;
- positive cross-section rotation occurs when the top flange displaces towards the east (counter-clockwise rotation if the observer is standing at the north end of the girder and looking south); and
- positive longitudinal displacement at the ends is away from the girder centreline (i.e., axial extension).

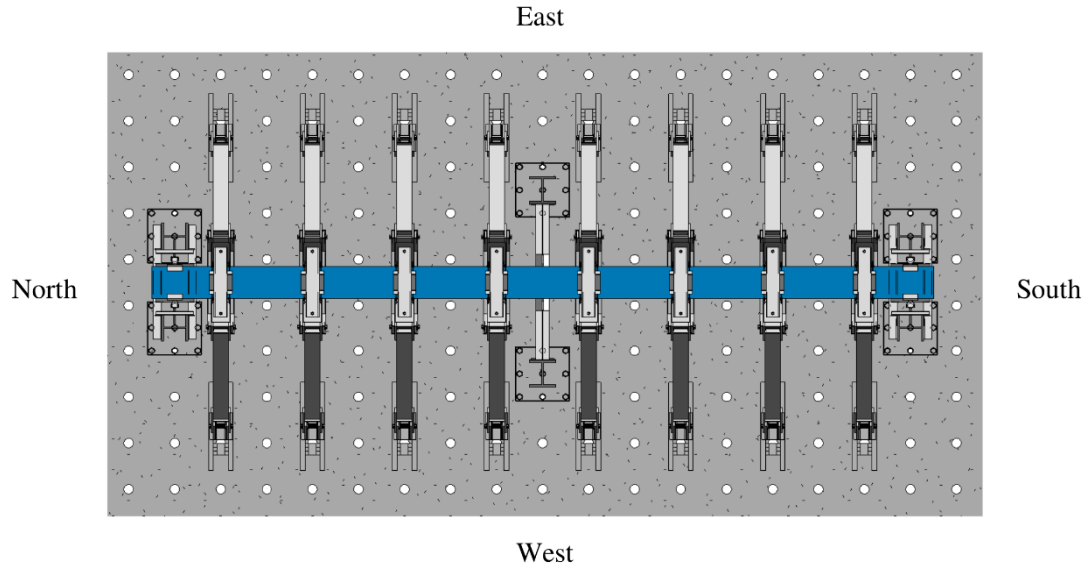


Figure 5-4: Cardinal directions of the test set-up (plan view)

Table 5-2 and Table 5-3 summarise the displacements observed at buckling and at ultimate, respectively, where ultimate is defined as the maximum attained lateral displacement (i.e., at the end of the test, immediately before unloading—these values cannot be compared to one another directly, although they are typically consistent with a cross-sectional rotation of about  $9^\circ$ ). This section discusses general observations of girder displacement during the tests, as well as the effect of geometric properties and initial geometric imperfections on displacement behaviour.

Table 5-2: Summary of mid-span displacements at buckling

Specimen ID	Vertical Displacement, $\delta_v$ (mm)	Lateral Displacement, $\delta_h$		Twist			Longitudinal Displacement	
		Top Flange	Bottom Flange	Top Flange	Web	Bottom Flange	North	South
		(mm)	(mm)	(°)	(°)	(°)	(mm)	(mm)
G6-470-32-2-p	62.1	13.6	-0.5	1.4	1.5	1.2	5.3	6.2
G6-430-32-1-p	57.7	16.6	-1.5	2.0	1.9	1.4	1.8	9.1
G6-430-32-1-f	55.3	-8.5	0.8	0.9	1.0	0.8	3.4	6.1
G6-300-32-1-p	43.6	-6.1	0.7	-0.8	-0.7	-0.6	3.3	4.7
G8-430-25-2-p	31.3	39.6	-3.4	3.1	3.2	2.8	5.0	1.9
G8-390-32-2-p	38.9	-10.6	4.8	-1.2	-1.2	-0.9	-0.3	9.5
G8-390-25-2-p	32.8	-22.2	4.4	-1.9	-2.0	-1.7	1.3	6.4

Table 5-3: Summary of mid-span displacements at ultimate

Specimen ID	Vertical Displacement, $\delta_v$ (mm)	Lateral Displacement, $\delta_h$		Twist			Longitudinal Displacement	
		Top Flange	Bottom Flange	Top Flange	Web	Bottom Flange	North	South
		(mm)	(mm)	(°)	(°)	(°)	(mm)	(mm)
G6-470-32-2-p	61.3	69.5	-1.7	7.0	7.5	6.1	4.8	5.8
G6-430-32-1-p	59.0	83.5	-1.0	8.5	9.0	7.2	0.9	9.0
G6-430-32-1-f	54.1	-72.6	0.9	7.3	7.6	6.2	3.0	5.4
G6-300-32-1-p	42.4	-81.1	-9.8	-7.1	-7.4	-6.5	3.3	4.5
G8-430-25-2-p	34.2	85.9	-8.7	7.2	7.2	6.2	4.9	1.9
G8-390-32-2-p	37.6	-111.2	7.2	-8.7	-9.5	-7.5	-1.5	9.1
G8-390-25-2-p	32.3	-79.7	9.5	-6.7	-6.8	-5.8	0.8	6.2

### 5.2.1 Global Displacement Response and Observations

During the tests, the ends of the test girders generally displaced away from the centreline, except for G8-390-32-2-p, which saw the entire girder move southward. Rollers were used at both end supports to allow symmetrical bending about the girder centreline but the resulting longitudinal displacements were often larger at one end than the other, as was the case for G6-430-32-1-p, which exhibited 9.1 mm of movement at the south end but only 1.8 mm at the north end at buckling. The maximum recorded longitudinal displacement was 9.5 mm, which was well within the  $\pm 65$  mm displacement capacity of the end support rollers. From buckling to ultimate, lateral buckling of the girder was the predominant behaviour (rather than major-axis bending), which caused the girder ends to move slightly towards the girder centreline, thereby resulting in a mean longitudinal shortening of 0.4 mm.

The amount of top flange lateral displacement at buckling ranged from 6.1 mm to 39.6 mm, while vertical displacements ranged from 31.3 mm to 62.1 mm. For all girders except G8-430-25-2-p, the amount of vertical displacement was greater than the lateral displacement of the top flange at buckling. From buckling to ultimate, vertical displacements either increased or decreased slightly, in the range of 0.8 to 2.9 mm. In contrast, the top flange lateral displacements increased steadily post-buckling and would have continued to increase had unloading not begun at approximately 80 mm of lateral displacement. However, in the case of G8-390-32-2-p, there was a sudden and large jump in lateral displacement in the post-buckling region, which resulted in an ultimate lateral displacement of 111 mm. The post-buckling lateral displacements were well-controlled for all other test girders. The majority of lateral movement was concentrated in the top flange, with the bottom flange moving very little during the tests—up to 4.8 mm at buckling and 9.8 mm at ultimate. The bottom flange generally displaced in the direction opposite that of the top flange.

The rotations of the top flange, web, and bottom flange at mid-span were also recorded. At buckling, the top flange and web rotations were within  $0.1^\circ$  of each other for all girders and ranged from  $0.7^\circ$  to  $3.2^\circ$ . In comparison, the bottom flange exhibited rotations up to  $0.6^\circ$  less than the top flange and web, which indicates non-rigid body (distortional) rotation. At ultimate, these differences increased; the greatest amount of rotation was observed in the web, followed by the

top flange, and lastly the bottom flange. The bottom flange rotations were found to be up to  $1.9^\circ$  less than the web rotations. However, the differences in measured rotations were not significant and cross-section distortion was not noticeable during visual examinations of the buckled girders. While the test girder cross-sections may not strictly have undergone rigid body rotation, the differences between top flange, web, and bottom flange rotations are likely not significant enough—especially at buckling—to be categorised as distortional buckling.

### 5.2.2 *Lateral and Vertical Displacements at Buckling*

The following subsections explore the observed relationship of geometric properties and initial geometric imperfections on lateral and vertical displacements at buckling. From the preliminary pre-test numerical models, a parameter characterising the displacement response of the test girders was defined as the ratio of top flange lateral displacement to vertical displacement at buckling ( $\delta_h/\delta_v$ ). This parameter is used again here, as it is (inversely) indicative of lateral stiffness in a member. The greater the value of  $\delta_h/\delta_v$ , the larger the lateral displacement at buckling (relative to vertical displacement) and the smaller the slope of the load–lateral displacement curve leading up to buckling, which is indicative of low lateral stiffness. Figure 5-5 and Figure 5-6 show the load–displacement behaviour of G6-300-32-1-p and G8-430-25-2-p, respectively, where the former exhibited the smallest  $\delta_h/\delta_v$  and the latter displayed the largest. The lateral displacements presented in load–displacement curves, such as in Figure 5-5 and Figure 5-6, always refer to the top flange. Load–displacement curves for the remaining test girders can be found in Appendix E.

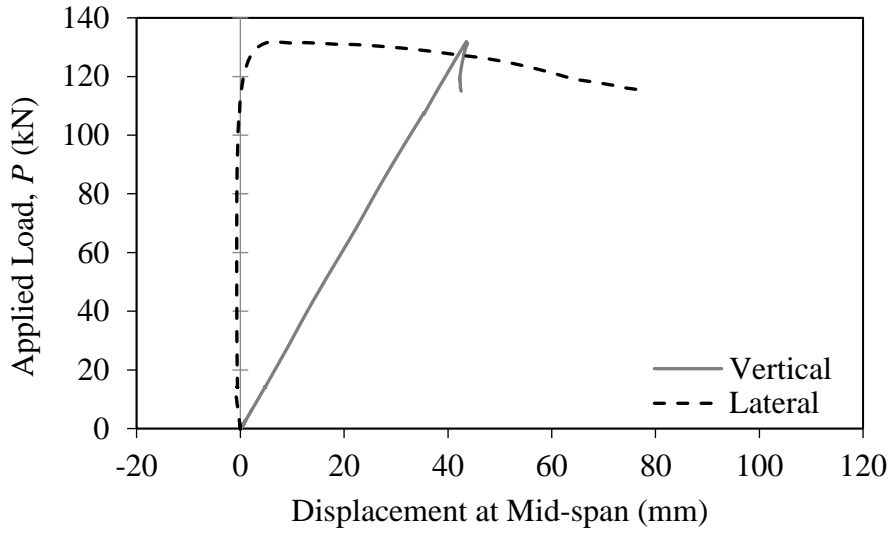


Figure 5-5: Load–displacement response of G6-300-32-1-p

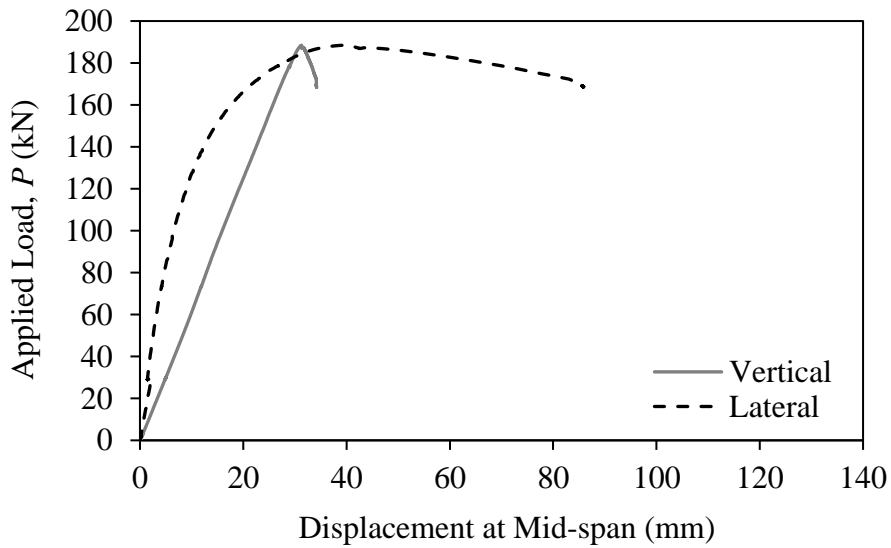


Figure 5-6: Load–displacement response of G8-430-25-2-p

### 5.2.2.1 Effect of Geometric Properties

Results of the numerical simulations indicated that  $\delta_h/\delta_v$  may be related to the geometric properties of slenderness ratio ( $L/r_y$ ) and moment of inertia about the weak axis ( $I_y$ ), where increasing  $L/r_y$  and decreasing  $I_y$  resulted in larger  $\delta_h/\delta_v$ . However, these relationships were not observed in the

test results. Though G6-300-32-1-p had the largest  $L/r_y$  and lowest  $I_y$ , it exhibited the smallest  $\delta_h/\delta_v$ . In contrast, G8-430-25-2-p had  $L/r_y$  and  $I_y$  values close to the mean yet displayed the largest  $\delta_h/\delta_v$ . The obtained  $\delta_h/\delta_v$  values were also compared with the previously identified stiffness parameters,  $EI_yGJ$  and  $\left(\frac{\pi E}{L}\right)^2 I_y C_w$ , but no definitive trends could be observed. This is likely because cross-sectional properties are not the only parameters affecting lateral stiffness of a member. Rather, the initial geometric imperfections may have been more influential, as discussed in the subsequent section.

#### 5.2.2.2 *Effect of Initial Geometric Imperfections*

The initial geometric imperfections that are most influential in LTB resistance are top flange lateral out-of-straightness (sweep) and twist. Camber is not expected to have a significant effect on moment resistance, nor is sweep of the bottom flange, as it is in tension. Table 5-4 provides a summary of the measured sweep and twist in relation to the mid-span lateral displacements of the top flange at buckling. Sweep and twist were measured at equally spaced stations along the girder; the reported values for each girder correspond to the maximum sweep or twist measured among the stations, which may not necessarily have occurred at mid-span. The salient observations are as follows:

- G6-430-32-1-p had initial measured sweep and twist values in opposite directions; during the test the top flange translated in the same direction as the initial twist, which suggests twist is the dominant imperfection. However, the maximum initial sweep value was not measured at mid-span, whereas maximum initial twist was.
- G6-300-32-1-p eventually buckled in the opposite direction of its initial measured sweep and twist, though its load–displacement response from Figure 5-5 shows that it initially displaced in the same direction as its sweep and twist. The sweep shape was in single curvature.
- G8-430-25-2-p exhibited the greatest lateral displacement at buckling and had the largest measured sweep and twist imperfections.
- Even though G8-390-32-2-p had a larger measured twist than G8-390-25-2-p, the latter had significantly larger lateral displacement at buckling. Sweep values were the same

between the two members and were the smallest measured in the girders tested; the sweep shapes were both in single curvature.

- G8-390-25-2-p exhibited the lowest sweep and twist values of the specimens tested, yet it had the second largest lateral displacement at buckling. It was also the only specimen where the measured initial twist changed direction, with  $-0.2^\circ$  measured at mid-span and  $0.2^\circ$  measured at the next station.

Table 5-4: Measured initial geometric imperfections and top flange lateral displacement at buckling

Specimen ID	Top Flange Lateral Displacement, $\delta_h$ (mm)	Top Flange Sweep (mm)	Twist ( $^\circ$ )
G6-470-32-2-p	13.6	1.5	0.4
G6-430-32-1-p	16.6	-2.0	0.6
G6-430-32-1-f	-8.5	-3.0	-0.3
G6-300-32-1-p	-6.1	3.0	0.4
G8-430-25-2-p	39.6	7.0	1.3
G8-390-32-2-p	-10.6	-1.0	-1.1
G8-390-25-2-p	-22.2	-1.0	$\pm 0.2$

The behaviour of G8-390-32-2-p was further investigated as it exhibited little lateral displacement at buckling despite having a relatively large value of twist (albeit a small value of top flange sweep). Figure 5-7 shows the top and bottom flange load–displacement response of G8-390-32-2-p. The bottom flange displaced in the opposite direction of the top flange, which is typical of the girders tested. However, the bottom flange began to deflect early in the test, while the slope of the top flange curve remained almost perfectly vertical. At buckling, the ratio of bottom-to-top-flange lateral displacement was  $-0.46$ . In comparison, the remaining six girders had a mean bottom-to-top-flange displacement ratio of  $-0.10$  at buckling. Moreover, G8-390-32-2-p had the largest measured bottom flange initial sweep of  $L/900$ . Though tension flange

imperfections are not expected to have a significant influence on LTB resistance, it is possible that they may affect the displacement behaviour of the member. In the case of G8-390-32-2-p, the large twist value may have had a bigger impact on the bottom flange displacement (i.e., greater displacements than typical) than the top flange.

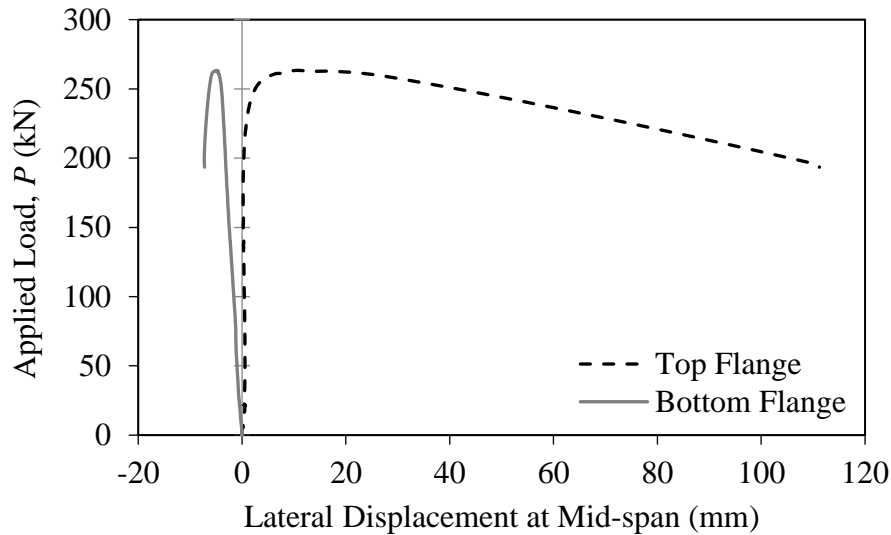


Figure 5-7: Top and bottom flange load–displacement response of G8-390-32-2-p

In the numerical simulations, the predicted  $\delta_h/\delta_v$  values ranged from 0.4 to 3.2. However, the obtained top flange lateral displacements at buckling were much lower than predicted, while the vertical displacements were comparable to the finite element predictions, which resulted in considerably lower  $\delta_h/\delta_v$  values of 0.1 to 1.3. The difference in predicted and obtained  $\delta_h/\delta_v$  may be attributed to the amplitude of initial geometric imperfections. The numerical model assumed a top flange sweep of  $L/1000$ , but the mean measured sweep of  $L/5500$  was notably smaller, which would increase the load–lateral displacement slope and decrease the expected lateral displacement at buckling.

However, a definitive relationship between initial geometric imperfections and displacement behaviour of the test girders was not observed. Increasing initial top flange sweep and twist did not necessarily increase top flange lateral displacement and  $\delta_h/\delta_v$ . Yet the fact that the girder with the largest measured geometric imperfections also exhibited the largest  $\delta_h/\delta_v$  suggests there is a

relationship between lateral stability and initial imperfections, as expected. Furthermore, the G8 series indicated a larger variation in  $\delta_h/\delta_v$  (0.27 to 1.27) compared to the G6 series (0.14 to 0.22), which indicates that variability in lateral stability may increase in deeper sections.

### 5.3 Flange Stress Analysis

LTB can be classified as inelastic if the net stress (i.e., including residual stresses) of the compression flange equals or exceeds the yield stress (Nethercot 1974). Though yielding of the tension flange at the web–flange junction may have already occurred, this does not qualify the girder as effectively inelastic, as lateral stability does not significantly decrease from its elastic value until the compression flange begins to yield (Nethercot 1974). Following this definition, the surface strains measured at the top (compression) flange using the digital imaging correlation system were used in conjunction with the measured residual stresses to determine whether inelastic LTB occurred. The post-processing area of interest was divided into 30 mm wide strips, as shown in Figure 5-8, to match the width of the sectioning strips for residual stress measurement. Though the point of first yield should theoretically occur at mid-span (the location of the maximum moment), the true location of first yield inevitably varies, and strips of 600 mm length were chosen to account for this variability. The mean strain along the longitudinal direction of the girder was extracted for each strip for the test duration and converted to an equivalent stress value. In Figure 5-8, the contours depict longitudinal surface strains at buckling and do not include strains from residual stresses. Therefore, the calculated stresses must be combined with the corresponding residual stress measurements to determine the actual stress in each strip. Inelastic LTB is deemed to have occurred if any of the strips reach the flange yield stress (from material testing results) prior to the buckling load.

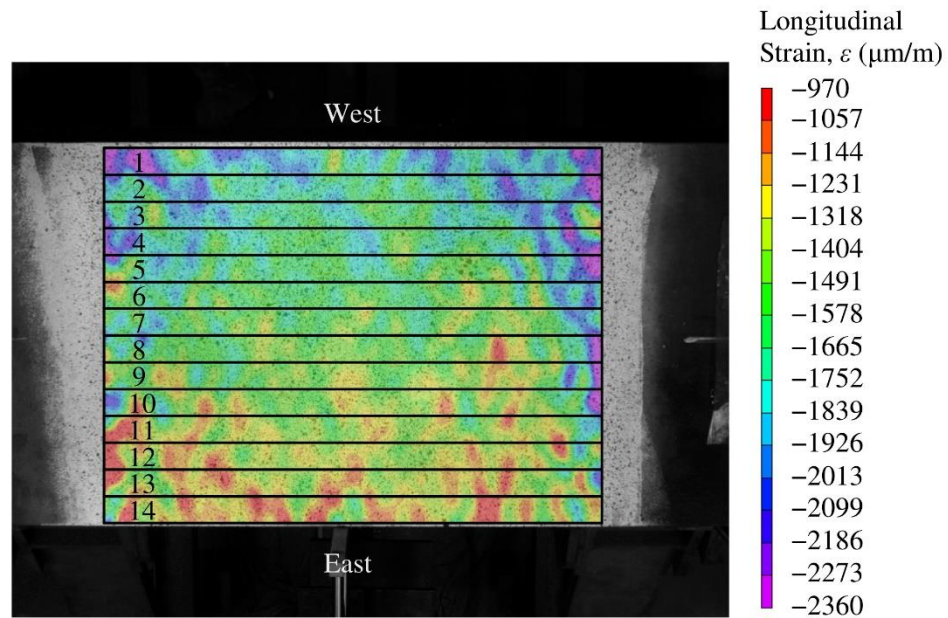


Figure 5-8: Area of interest from digital imaging correlation divided into 30 mm × 600 mm strips; contours represent longitudinal strains of G6-430-32-1-p at buckling

As the measured residual stresses varied considerably between the exterior and interior faces of the top flange, both faces were considered in the flange stress analysis. The measured exterior residual stresses were used with measurements from the digital imaging correlation system, which recorded strains on the exterior face of the top flange. To determine the corresponding strains at the interior face, the section curvature relationship,  $\phi_c = \varepsilon/c$ , was used, where  $\varepsilon$  is strain and  $c$  is the distance from the extreme fibre to the neutral axis. Assuming the neutral axis always passes through the centroid,  $c$  is taken as half the girder depth and  $\varepsilon$  is taken as the strain at the exterior face (from the digital imaging correlation system) to determine  $\phi_c$  for each strip. Using the calculated  $\phi_c$ , the strains at the interior face can be determined using geometry, as shown in Figure 5-9. The calculated interior strains were then used with the measured residual stresses on the interior face. It must be noted that, in reality, the neutral axis does not always pass through the centroid, as residual stresses cause unsymmetrical yielding of the cross-section. This assumption was used to approximate the stresses on the interior face but classification of elastic or inelastic LTB was based on whether the exterior strips yielded.

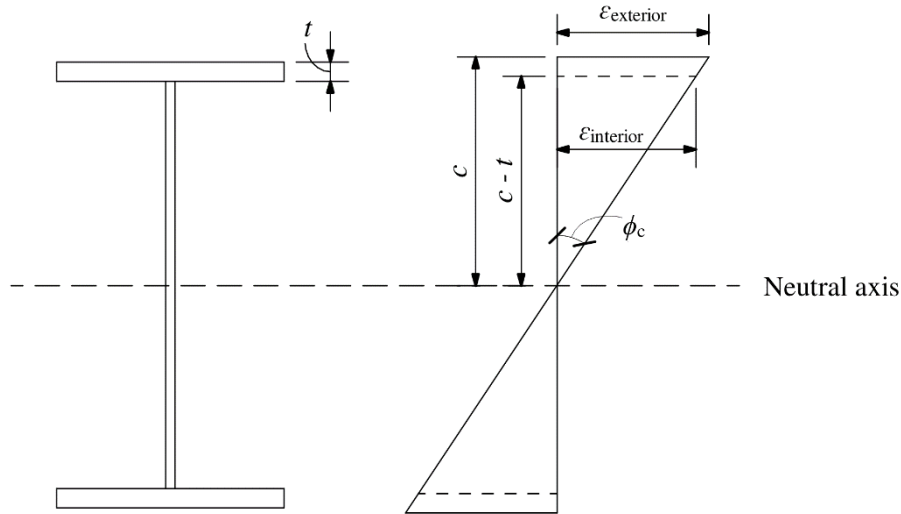


Figure 5-9: Section curvature relationship to determine stresses at exterior and interior faces of the top flange

Stress analysis was performed on four of the seven test girders, as residual stress measurements were available for only four sections. Figure 5-10 to Figure 5-13 show the net longitudinal stress distributions across the top (compression) flanges at buckling for the analysed sections, where positive stress corresponds to tension and negative stress indicates compression. The plotted stresses have been normalised by the yield stress of the flange and the strip number convention follows Figure 5-8, with strip numbers increasing from west to east. In examining the stress distributions, one side of the flange typically displayed lower compressive stresses than the other, which was found to be related to the direction of lateral buckling. For example, if the top flange of girder displaces towards the east, as in the case of G8-430-25-2-p, the compressive stresses are lower in the east portion of the flange. To explain this relationship, the top flange can be thought of as a member undergoing major-axis flexural bending, where the east side is in “tension” and the west side is in compression, as shown in Figure 5-14. As the top flange is always in compression (due to major-axis bending from the applied loads), the “tension” portion on the east side is manifested as lower compressive stresses. Conversely, the west side sees greater compressive stress values.

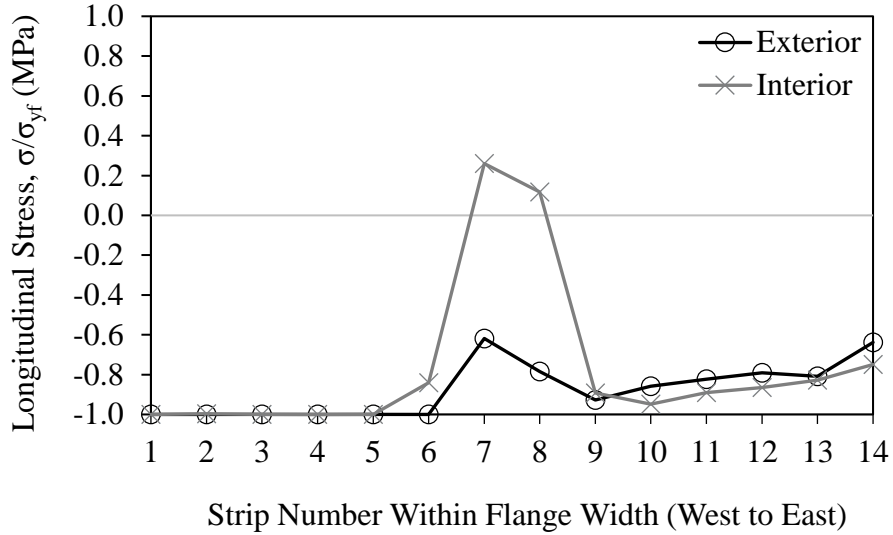


Figure 5-10: Top flange stress distribution at buckling of G6-430-32-1-p

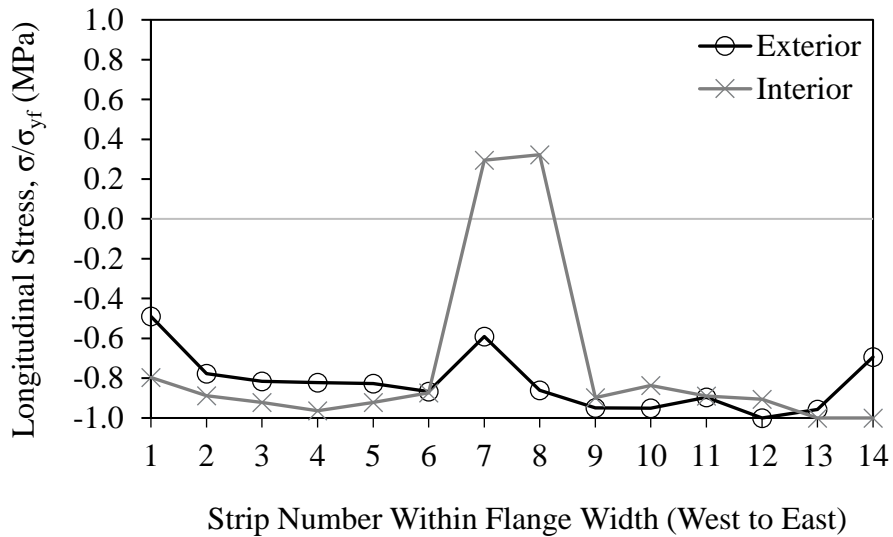


Figure 5-11: Top flange stress distribution at buckling of G6-430-32-1-f

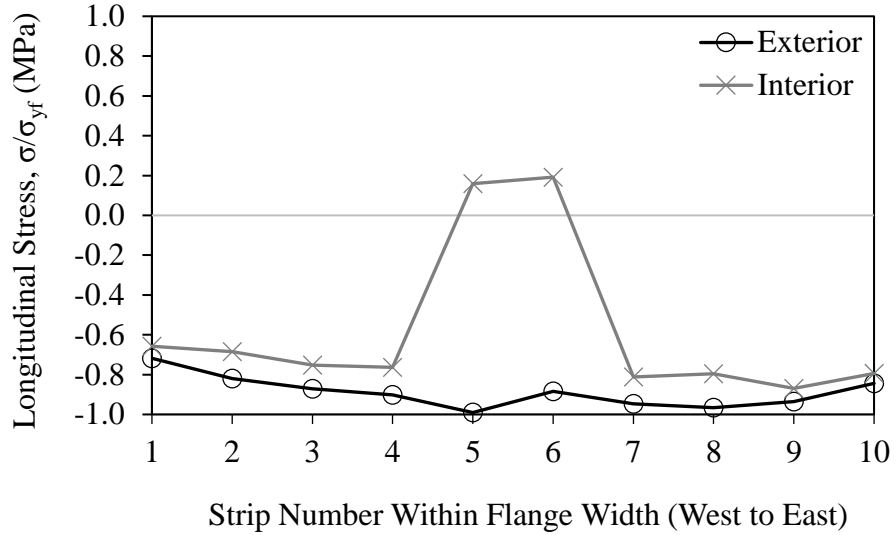


Figure 5-12: Top flange stress distribution at buckling of G6-300-32-1-p

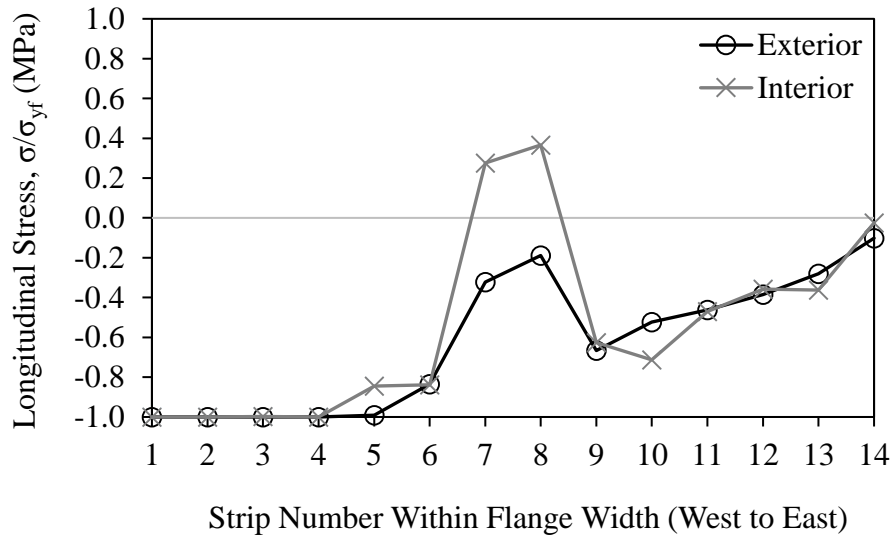


Figure 5-13: Top flange stress distribution at buckling of G8-430-25-2-p

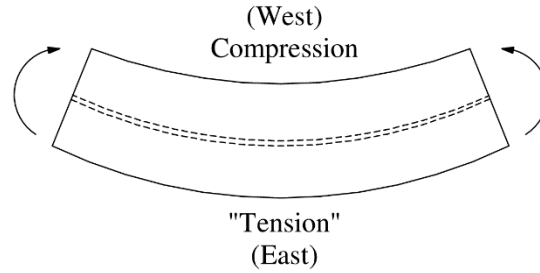


Figure 5-14: Plan view of top flange undergoing minor-axis bending

Of the analysed girders, G6-430-32-1-p/f and G8-430-25-2-p all exhibited flexural yielding at the time of buckling, whereas G6-300-32-1-p did not, which means the former failed in inelastic LTB and the latter in elastic LTB. Though G8-430-25-2-p had an experimental  $M_{\max}/M_p$  value of 0.52, which falls in CSA S16-14's definition of elastic LTB, it was deemed an inelastic LTB failure through the flange stress analysis. Moreover, G8-430-25-2-p had a lower  $M_{\max}/M_p$  than G6-300-32-1-p's value of 0.62, yet G6-300-32-1-p was determined to have failed in elastic LTB. In the case of G6-430-32-1-f, the  $M_{\max}/M_p$  from test results was 0.79, which indicates that it is well within the inelastic LTB region specific by CSA S16-14. However, the stress analysis suggests that it is on the boundary between elastic and inelastic LTB, as only one strip yielded (on the exterior face) at the buckling load. These results indicate that  $M_{\max}/M_p$  may not be the best parameter to delineate the boundary between elastic and inelastic LTB behaviour. Stress analysis of the remaining three girders, particularly G8-390-32-2-p and G8-390-25-2-p, will provide valuable insight into this observation.

## 5.4 Comparison of Experimental Results with Design Equations

In this section, the results obtained from physical testing are compared with predictions from design equations, with a focus on evaluating the adequacy of the CSA S16-14 provisions. The analysis is separated into two parts, as two sets of predicted resistances are considered—one set for shear centre loading and the other for top flange loading. To obtain the top flange resistances, load height adjustment equations were applied to the shear centre resistances.

Though the test girders were loaded above the shear centre in the experimental programme, the comparison with shear centre resistances is important, as the design equations were initially developed for shear centre loading. While the capacity predictions themselves would not be expected to be accurate, this allows trends between test results and predicted resistances to be observed without additional variability that may arise from the load height adjustment equations.

#### 5.4.1 Predicted Capacities – Shear Centre Loading

Table 5-5 provides a comparison of the moment resistances obtained from test results and predicted resistances from CSA S16-14, AISC 360-16 (AISC 2016), and the equation proposed by MacPhedran and Grondin (2011). The predicted resistances from design equations assume shear centre loading, whereas the test configuration loaded girders 178 mm above the top surface of the top flange. A resistance factor of 1.0 was used for all design equations; plastic moment capacity was determined using actual cross-section dimensions and actual yield stresses (flange and web differentiated); the actual elastic modulus of the flange was used (as the flange provides the majority of the bending stiffness); and moment gradient factors—for the actual bending moment diagram of each test—were calculated using the CSA S16-14 provisions. In Table 5-5, test-to-predicted ratios greater than 1.0 and positive percent difference values indicate the design equations are conservative (even if loading is applied above the top flange). Figure 5-15 presents the moment resistances from test results and the design equations. Specimen identifications are labelled immediately beside the respective test result; MG represents resistances calculated using the MacPhedran and Grondin (2011) equation; SC and ATF represent shear centre and above top flange loading, respectively.

Table 5-5: Comparison of moment resistances from experimental results and design provisions

Specimen ID	Test	CSA S16-14			AISC 360-16			MacPhedran & Grondin		
	Moment, $M_{max}$ (kN·m)	Moment, $M_{max}$ (kN·m)	Test-to- predicted	% Diff.	Moment, $M_{max}$ (kN·m)	Test-to- predicted	% Diff.	Moment, $M_{max}$ (kN·m)	Test-to- predicted	% Diff.
G6-470-32-2-p	2756	3018	0.91	-9.5	3112	0.91	-12.9	2641	1.04	4.2
G6-430-32-1-p	2349	2705	0.87	-15.2	2784	0.87	-18.5	2336	1.01	0.6
G6-430-32-1-f	2359	2706	0.87	-14.7	2786	0.87	-18.1	2337	1.01	0.9
G6-300-32-1-p	1327	1539	0.86	-16.0	1574	0.86	-18.6	1259	1.05	5.1
G8-430-25-2-p	1877	2968	0.63	-58.1	3000	0.63	-59.8	2485	0.76	-32.4
G8-390-32-2-p	2619	3123	0.84	-19.2	3174	0.84	-21.2	2595	1.01	0.9
G8-390-25-2-p	1869	2538	0.74	-35.8	2577	0.74	-37.9	2088	0.90	-11.7

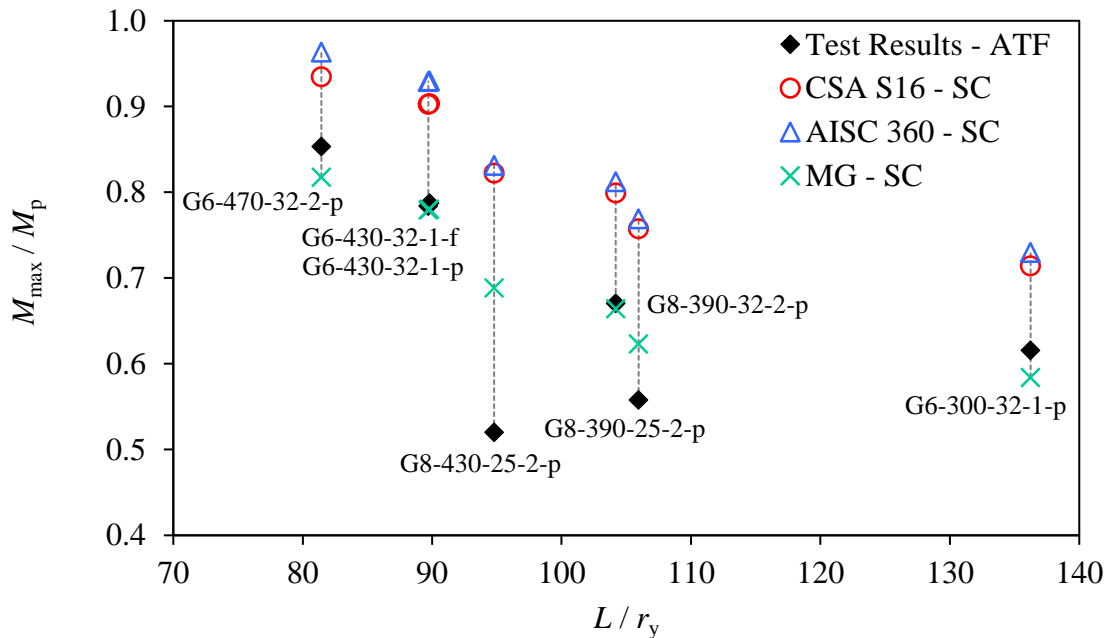


Figure 5-15: Moment resistances from test results and design equations

None of three design equations reflects the disruption of the smooth trend by G8-430-25-2-p and G8-390-25-2-p. To investigate potential reasons behind this observation, the displacements at buckling and initial geometric imperfections of the test girders are examined.

#### 5.4.1.1 Effect of Lateral and Vertical Displacements at Buckling

Of the specimens tested, G8-430-25-2-p had the largest ratio of mid-span lateral-to-vertical displacement at buckling ( $\delta_h/\delta_v$ ), followed by G8-390-25-2-p. Figure 5-16 depicts the relationship between the test-to-predicted ratios of the three design equations and the obtained  $\delta_h/\delta_v$  for the seven tested girders; the two girders in question are labelled for reference. The plot shows a linear relationship between the variables, where the larger the ratio of  $\delta_h/\delta_v$ , the larger the over-prediction by the three design equations. This suggests that  $\delta_h/\delta_v$  is an influential parameter in LTB resistance and that the LTB resistance of girders with large ratios of  $\delta_h/\delta_v$  may not be well predicted by the design equations. Though the chosen parameter is indicative of lateral stiffness, it is more of a response than a defined section or member property. Therefore, the effects of initial geometric imperfections—known to contribute to the response ratio  $\delta_h/\delta_v$ —are examined further.

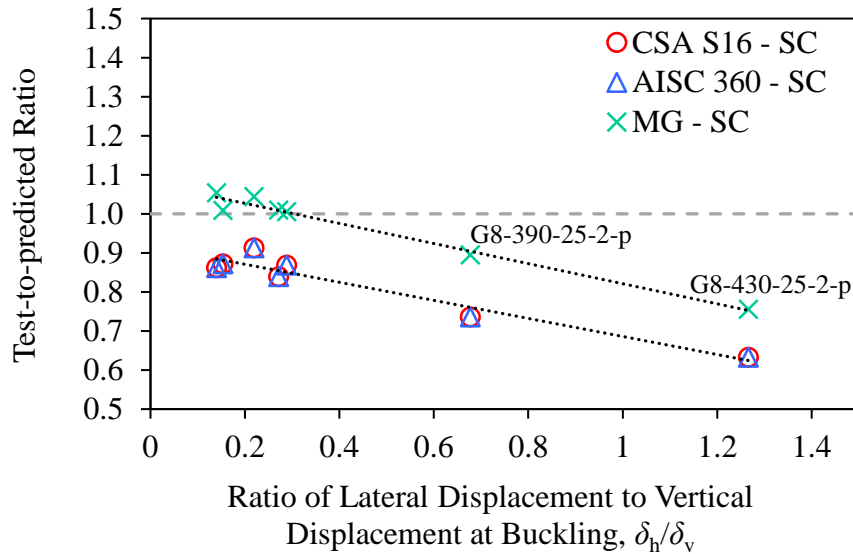


Figure 5-16: Relationship between test-to-predicted ratio and  $\delta_h/\delta_v$

#### 5.4.1.2 Effect of Initial Geometric Imperfections

While the effect of initial geometric imperfections on girder displacement behaviour was discussed in Section 5.2.2.2, their influence on LTB behaviour is expanded upon here—with reference to predicted LTB resistances—to examine reasons behind the atypical behaviour of G8-430-25-2-p and G8-390-25-2-p. Figure 5-17 and Figure 5-18 show the relationship between the test-to-predicted ratios and measured sweep and twist, respectively. As initial geometric imperfections are known to reduce LTB resistance, it is congruent for test-to-predicted ratios to decrease with increasing measured geometric imperfections, but no discernible trends are observed. For example, G8-390-25-2-p had the second lowest test-to-predicted ratio but exhibited the least amount of top flange sweep and twist.

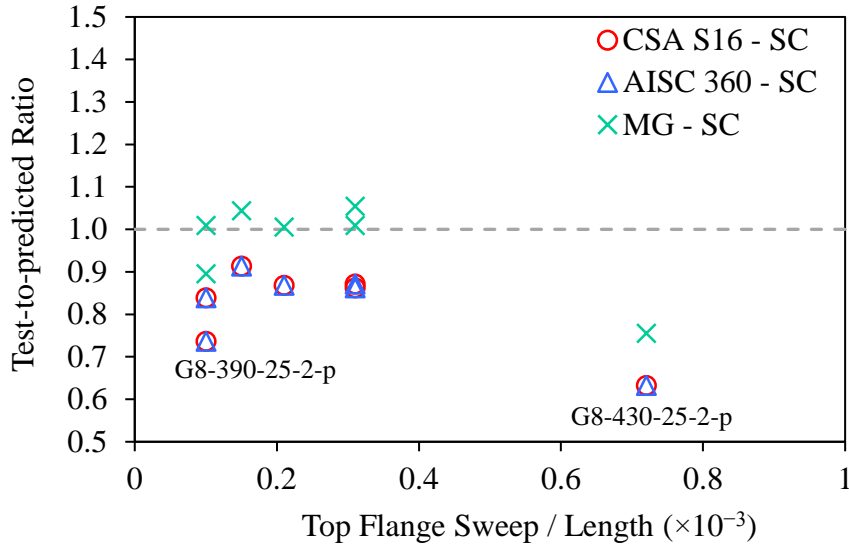


Figure 5-17: Relationship between test-to-predicted ratio and initial top flange sweep

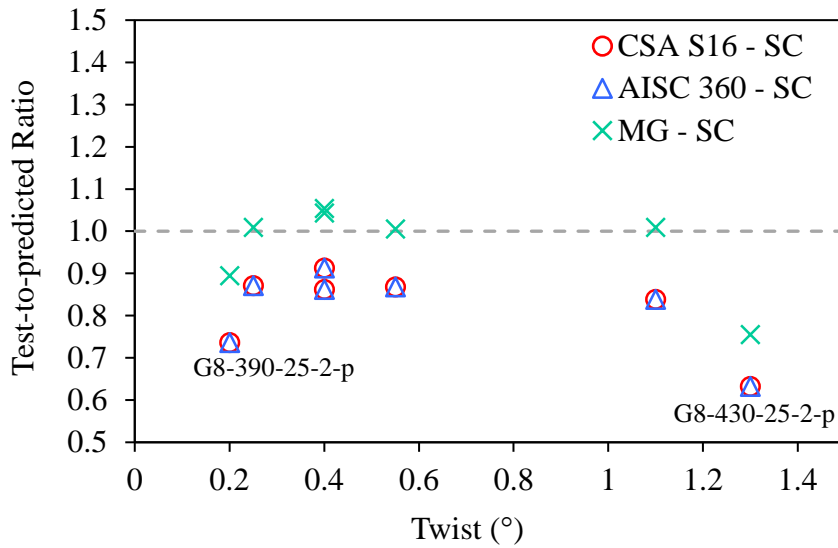


Figure 5-18: Relationship between test-to-predicted ratio and initial twist

While the effect of initial top flange sweep and twist on LTB resistance is generally unclear, G8-430-25-2-p—the member with the largest measured top flange sweep and twist—was also the most over-predicted by the design equations. This indicates that a relationship does exist between the magnitude of initial geometric imperfections and the adequacy of design equations in predicting LTB resistance. Therefore, for both girder displacement behaviour (as discussed in

Section 5.2.2.2) and predicted LTB resistance, initial geometric imperfections appear to have an influential effect, but a clear relationship cannot be discerned. Future test results from the remaining four girders will provide an increased database for drawing conclusions regarding the initial geometric imperfections.

#### 5.4.2 Predicted Capacities – Top Flange Loading

This section applies a load height modification to the predicted capacities and compares the adjusted resistances to the test results. As CSA S16-14 is the focus of the research, the analysis of load height effect is only completed for the predicted resistances from CSA S16-14.

To adjust the CSA S16-14 predictions for load height, three approaches were used. The three methods were introduced in Section 2.2.3 and are summarised here. The first method, as prescribed by CSA S16-14, is to assume a moment gradient factor of 1.0 and an unbraced length of  $1.2L$ ; this modification is intended for cases of top flange loading (Wong et al. 2015) and for that case provides a lower bound capacity. Another method from the *SSRC Guide* (Galambos 1998)—based on the research by Nethercot and Rockey (1971)—calculates a modified moment gradient that accounts for load height, denoted by  $\omega_2^*$ . This method, as shown in Equation 5-1, is intended for loading applied anywhere (vertically) on the cross-section. Lastly, Helwig et al. (1997) proposed a simplification to Equation 5-1 by setting  $B$  equal to 1.4, as shown in Equation 5-2; it is applicable for loading applied anywhere on the cross-section. The three methods are used to adjust the CSA S16-14 predicted resistances to reflect top flange loading, but none of the methods purports to consider loading above the top flange, as it is an uncommon loading scenario in practice. Because the test configuration applies loads 178 mm above the top flange, the load height effect is likely even larger than predicted by the three approaches, which is considered when interpreting the results.

$$\omega_2^* = AB^{2y/d} = \omega_2 \left[ 1 - 0.154 \left( \frac{\pi}{L} \sqrt{\frac{EC_w}{GJ}} \right)^2 + 0.535 \left( \frac{\pi}{L} \sqrt{\frac{EC_w}{GJ}} \right) \right]^{2y/d} \quad 5-1$$

$$\omega_2^* = \omega_2(1.4^{2y/d}) \quad 5-2$$

To gauge the accuracy of the load height adjustment modifications, they were first used to predict the capacities of the welded girders tested by Fukumoto and Itoh (1981), which were loaded at the top flange. The predicted load capacities using the load height adjustments are compared with test results in Table 5-6. As with the shear centre loading analysis, positive percent difference values indicate the load height adjustments are conservative and underestimate the member capacity. The results show that the CSA S16-14 method tends to underestimate member capacity, the SSRC method either underestimates or overestimates member capacity, while the Helwig et. al approach tends to overestimate member capacity. Kabir and Bhowmick (2016), however, compared  $\omega_2^*$  values from the Helwig et al. approach to those from numerical simulations (back-calculated from moment resistance, as discussed in Section 2.4.3), and found the Helwig et al. approach to be conservative. The variability of the results suggests that the three adjustment methods may not rigorously characterise load height effects, which should be considered when using them to adjust predicted member capacities for the test girders in this study.

Table 5-6: Percent difference between test capacities of Fukumoto and Itoh (1981) and CSA S16-14 predictions with load height modifications

	Maximum Load (kN)	Percent Difference		
		CSA S16-14	SSRC	Helwig et al.
D-series	149.8	-0.6	-5.8	-9.5
E-series	88.2	18.5	4.7	-0.6

The moment resistances from test results and from the adjusted CSA S16-14 predictions are shown in Figure 5-19 and Table 5-7. In Figure 5-19, TF and ATF represent top flange and above top flange loading, respectively. The mean percent differences between test results and the adjusted predictions are 1.0%, -3.9%, and 7.0% for the CSA S16-14, SSRC, and Helwig et al. methods, respectively. All three approaches overestimate the capacity of G8-430-25-2-p by a significant margin of 19 to 29%. In contrast, the capacity of G6-300-32-1-p is underestimated by 7 to 28%.

As the load height adjustment methods have been shown to both overestimate and underestimate member resistances, it is difficult to conclude whether differences between the test results and adjusted CSA S16-14 predictions are due to inadequacies in CSA S16-14 or due to inaccurate considerations of the load height effect. However, a holistic approach that considers the observations from preceding sections can be used to draw general conclusions regarding the adequacy of CSA S16-14 in characterising LTB resistance in modern welded girders.

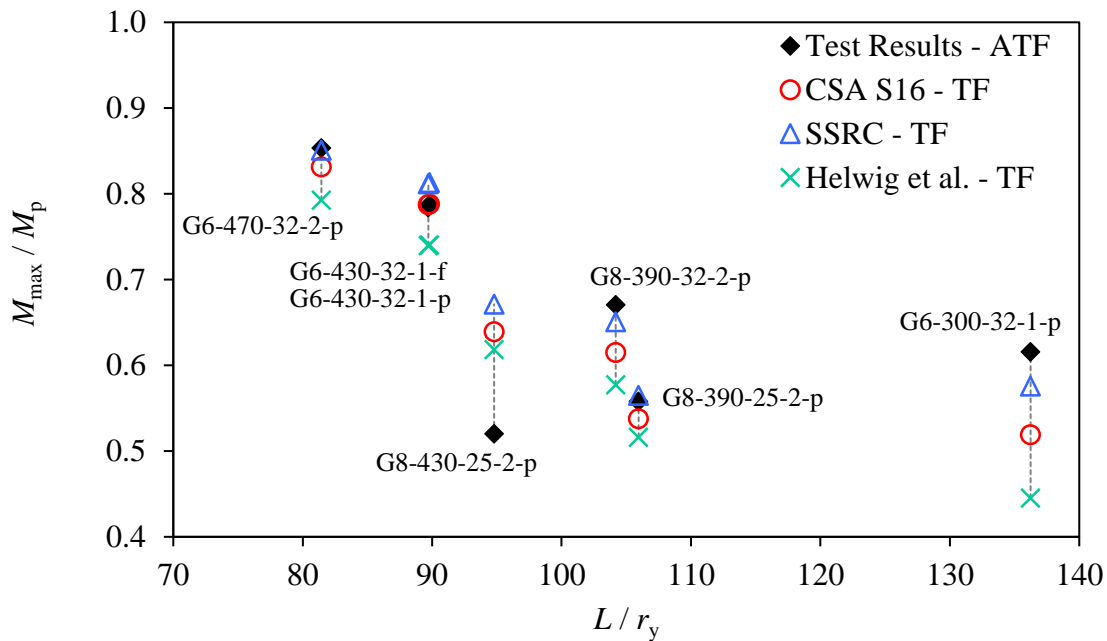


Figure 5-19: Moment resistances from test results and design equations, adjusted for top flange loading

Table 5-7: Comparison of moment resistances from experimental results and CSA S16-14 predictions with load height modifications

Specimen ID	Test ATF	CSA S16-14		SSRC		Helwig et al.	
	Moment, $M_{max}$ (kN·m)	Moment, $M_{max}$ (kN·m)	% Diff.	Moment, $M_{max}$ (kN·m)	% Diff.	Moment, $M_{max}$ (kN·m)	% Diff.
G6-470-32-2-p	2756	2684	2.6	2747	0.3	2559	7.2
G6-430-32-1-p	2349	2358	-0.4	2432	-3.5	2216	5.7
G6-430-32-1-f	2359	2361	-0.1	2435	-3.2	2217	6.0
G6-300-32-1-p	1327	1119	15.7	1241	6.5	959	27.7
G8-430-25-2-p	1877	2306	-22.9	2422	-29.0	2230	-18.8
G8-390-32-2-p	2619	2402	8.3	2543	2.9	2255	13.9
G8-390-25-2-p	1869	1801	3.6	1892	-1.2	1728	7.5

Loading 178 mm above the top flange means the test capacities are likely lower than if it were top flange loading, which is what the three load height adjustment methods were intended for. Therefore, over-predictions in the adjusted resistances do not necessarily mean that CSA S16-14 is unconservative. However, the additional 178 mm is not expected to cause reductions of the magnitude required to explain the 19 to 29% over-prediction in capacity for G8-430-25-2-p, which suggests that CSA S16-14 is likely giving an unconservative estimate of its LTB resistance. Moreover, G8-430-25-2-p has been noted for having the largest measured top flange sweep and twist (though all its initial geometric imperfections were within tolerance). It also exhibited the largest  $\delta_h/\delta_v$ , which indicates low lateral stiffness compared to the other test girders. All these factors considered, an over-prediction in resistance by CSA S16-14 is probable.

In the case of G6-300-32-1-p, the three load height adjustment methods were overly conservative in predicting its moment resistance. Again, the measured geometric imperfections and displacement behaviour must be considered. Its top flange sweep of  $L/3300$  and twist of  $0.4^\circ$  were near the mean values of  $L/5500$  and  $0.6^\circ$ , respectively, but G6-300-32-1-p eventually buckled in the opposite direction of its initial geometric imperfections. It had the lowest  $\delta_h/\delta_v$ , which indicates that its lateral stiffness was high compared to the other test girders, and its load–displacement curve was akin to a member with negligible imperfections. All these factors considered, it is likely that CSA S16-14 underestimated the resistance of G6-300-32-1-p (and not because of inaccuracies in the load height adjustment).

G8-430-25-2-p and G6-300-32-1-p aside, it appears that the resistances adjusted for load height are similar to the obtained test results, which suggests that CSA S16-14 gives adequate predictions of LTB capacity for the remaining five test girders. Aside from G8-430-25-2-p, the largest over-prediction observed was 3.5%, for G6-430-32-1-p. While some of the adjusted resistances were found to underestimate the true LTB resistance of the test girders, this is of less concern when evaluating the adequacy of CSA S16-14.

## 5.5 Experimental Errors

During the large-scale testing, various factors may have contributed to experimental errors and are categorised into: errors in load measurement instrumentation, unintentional eccentricity in loading, and unintended or insufficient restraint in test set-up.

Load was recorded using Strainsert load cells at the end supports and fabricated load cells at each load point. For the duration of all the tests, the eight fabricated load cells gave similar readings, typically within 2 kN of each other. This indicates they were behaving as designed, as the load is theoretically identical at each load point. While it is possible that the accuracy of the fabricated load cells contributed to the small differences in measured load, a more likely reason is that the applied loads were actually not identical at the eight points. In a perfect system, the eight hydraulic actuators should apply identical forces as they were linked to a single hydraulic manifold and control system. However, the hoses connecting the actuators to the manifold varied in length, where the actuators near the girder mid-span had the shortest hoses and those near the end supports had the longest hoses. As the oil in the hydraulic system must travel farther to reach the actuators near the ends, the result can be a slightly lower load reading, with the difference gradually attenuating. The individual load readings were generally congruent with this explanation, with higher loads near mid-span and lower readings away from mid-span. To minimise errors from non-identical applied loads, a slow loading rate of 0.5 to 1 kN/s was used to allow time for the oil to equalise throughout the system.

The Strainsert load cells proved to be less reliable in recording load. Though all load cells were calibrated prior to testing, the total load measured by the Strainsert load cells began to differ from the total load calculated from summing the eight load readings at the load points. While slight differences between the two methods of obtaining total load may be expected due to frictional losses, the observed difference was up to 10% for the first test (G6-430-32-1-f). Moreover, given the symmetry of the loading configuration and test set-up, similar readings from the Strainsert load cells at each support were expected, but were not the case observed for the first test, as the north load cell differed from the south load cell by up to 16%. After the first test, the Strainsert load cells

were recalibrated per the nominal manufacturer specifications and the difference in total load readings was reduced to 5%.

Another possible error arose from unintended eccentricities in loading, which can occur if the rotational hemisphere in the load collar is not centred on the flange width. To minimise load eccentricities, the load collar was centred by ensuring the distance between the threaded rod and flange tip on both sides was equal, as shown in Figure 5-20. As the hemisphere is bolted to the centre of the top HSS, this effectively centres the hemisphere on the flange width.

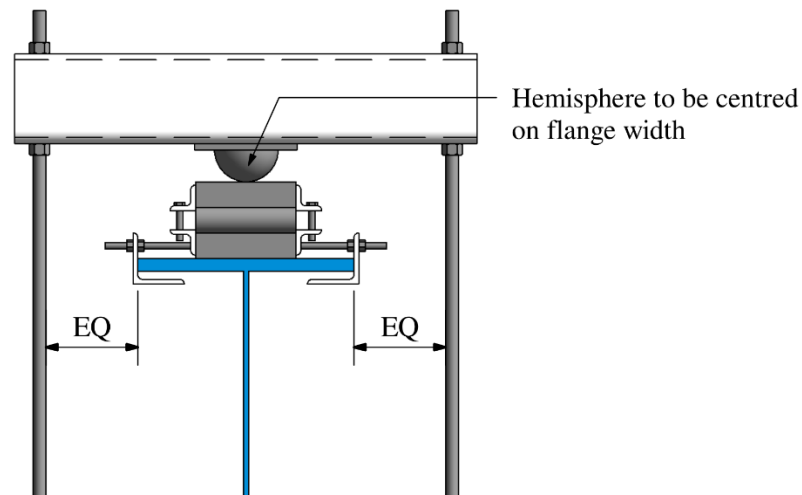


Figure 5-20: Centring of rotational hemisphere on flange width

Lateral restraint is also important to consider for experimental error. Errors can arise if the lateral bracing at the supports were not sufficiently strong and stiff to create the torsionally pinned end condition or, conversely, if the test set-up restrained the lateral movement of the girder at any points besides at the ends. The lateral braces at the end supports were designed using the AISC 360-16 provisions. To understand the conservatism of the AISC 360-16 brace design forces, the required brace strength was also approximated by  $0.02A_c\sigma_{yf}$ , where  $A_c$  is the compression flange area,  $\sigma_{yf}$  is the flange yield stress, and 0.02 is a common ratio of brace force to flange force. The  $0.02A_c\sigma_{yf}$  is considered conservative as it assumes a fully plastic compression flange and resulted in a required brace strength of 115 kN, which is comparable to the 117 kN predicted by the AISC 360-16 method and suggests that the AISC 360-16 provisions are conservative. The required brace strength was further analysed in the preliminary pre-test numerical models, which predicted

maximum lateral forces of 46 kN at the flanges and indicates the designed lateral brace strength of 117 kN is sufficient. Aside from the end supports, the only lateral restraint potentially exerted on the test girders would come from the gravity load simulators, which could result in higher recorded moment resistances. As the elastic LTB region is well-understood and adequately predicted, moment resistances of test girders that exhibited elastic behaviour (only G6-300-32-1-p for the time being) could be used to compare against the theoretical elastic LTB resistance to ensure there are no additional restraints from the gravity load simulators. However, this requires the load height effect to be rigorously accounted for.

## 5.6 Discussion on the Adequacy of CSA S16-14

From the results of the experimental programme, the adjusted CSA S16-14 predictions (to account for top flange loading) appear to give reasonable predictions for five of the test girders but significantly overestimated the strength of one girder and underestimated another. While these results suggest that the Canadian provisions are generally adequate, it is important to explore the circumstances behind these predictions, especially as previous researchers (Kabir and Bhowmick 2016; MacPhedran and Grondin 2011) have suggested that CSA S16-14 overestimates LTB resistance in welded girders.

In this experimental programme, the mean recorded top flange sweep was  $L/5500$ , which is considerably smaller than the assumed initial imperfection of  $L/1000$  used in Kabir and Bhowmick's (2016) numerical simulations. In the same study, Kabir and Bhowmick (2016) concluded that CSA S16-14 may over-predict LTB resistance by as much as 37% when using mill plate residual stress distributions measured at Lehigh University, which had compressive residual stresses of  $0.25F_y$  at the flange tips. However, the mean compressive residual stress at the flange tips measured for the test girders in this study was  $0.03F_y$ , which is considerably lower than the Lehigh distribution and may have contributed to higher obtained moment resistances. MacPhedran and Grondin (2011) also indicated that CSA S16-14 may overestimate the capacity of welded girders in the inelastic LTB region. However, the database of tests used in their analysis were primarily from 1970s. As welded girder fabrication has been significantly updated, the test girders in this study may have inherently higher resistances than equivalent sections fabricated in the

1970s, primarily due to more favourable residual stress distributions as well as lesser initial geometric imperfections. In other words, improvement in fabrication processes may result in higher LTB resistance for welded steel girders.

However, this is not to suggest that the Canadian provisions are wholly adequate for predicting LTB resistance in modern welded girders. The results of the study indicated variable LTB behaviour in the test girders. For the girder with a sweep value of  $L/1400$  and twist of  $1.3^\circ$ , which are within the tolerances prescribed by CSA W59-13 (CSA 2013a) and G40.20-13 (CSA 2013b), CSA S16-14 appeared to significantly over-predict its moment resistance. Moreover, the obtained mean sweep of  $L/5500$  is considerably lower than the tolerance limit of  $L/1000$ . For larger girders used in practical applications, the propensity for initial geometric imperfections is likely to increase, and it is possible that CSA S16-14 may over-predict their capacity. The future experimental tests of the deeper G9 girders may shed light on this.

While the girder with the largest sweep and twist was also the most over-predicted by CSA S16-14, there was no definite trend observed between initial geometric imperfections and LTB resistance, which echoes the observations from Fukumoto et al. (1980) and Fukumoto and Itoh (1981). However, this does not mean that geometric imperfections do not affect LTB, especially as numerical simulations have shown there is a relationship between the two (Boissonnade and Somja 2012). The only parameter that exhibited an observable trend with predicted LTB resistance was  $\delta_h/\delta_v$ , which is a displacement response that is indicative of lateral stiffness. Increasing  $\delta_h/\delta_v$  was found to increase the over-prediction in resistance, which suggests that moment resistance predictions by CSA S16-14 are influenced by the extent of lateral displacement at buckling. Though the factors affecting  $\delta_h/\delta_v$  are difficult to define, it appears to be related to not only geometric properties considered in the CSA S16-14 design equations, but also initial geometric imperfections such as compression flange sweep and twist.

## 6 CONCLUSIONS AND RECOMMENDATIONS

### 6.1 Summary

Lateral–torsional buckling (LTB) is a stability-related failure mode of unbraced or insufficiently braced steel girders under flexural bending. In Canada, LTB resistance for steel beams is determined in accordance with the steel design standard, CSA S16-14. In recent years, concerns have been raised regarding the adequacy of the CSA S16-14 provisions to predict the LTB resistance of welded girders accurately, particularly in the inelastic LTB region. The focus on welded girders stems from the welding itself, as it results in residual stress distributions that may cause welded sections to be more susceptible to LTB than rolled sections. While numerical studies have suggested a need to update the provisions, the physical testing data used for these studies are dated and may no longer be representative of modern welded girders.

In response to the lack of up-to-date physical testing, a large-scale experimental programme was developed to examine the adequacy of the CSA S16-14 provisions. The study consisted of 11 welded girders with unbraced spans of 32 ft—all predicted to fail in inelastic LTB. Girders were simply-supported in-plane and torsionally pinned, with eight vertical loads applied to simulate a uniformly distributed load. The research methodology was separated into four major parts: development the test specimen matrix, design of the test set-up, completion of physical testing, and analysis of test results.

As part of test matrix development, parameters that may affect LTB were identified and considered when selecting test girders. The final matrix was determined based on geometric variability, aspect ratio, range of inelastic LTB behaviour, section class, and plate cutting method. Adherence to fabrication processes typical of industry-standard welded girders was maintained as much as possible during production of the test girders. In the test set-up design, preliminary pre-test numerical simulations were performed for the test girders to anticipate their strength as well as expected displacements, which were used to ensure the test set-up could accommodate the full range of anticipated movements. This was particularly important for the gravity load application mechanism, which was designed to maintain continuous vertical load application even as the test girder swayed laterally and twisted. Prior to testing, initial geometric imperfections were measured

for each test girder; residual stresses of the girders were also measured in a companion research project.

Seven physical tests were performed and residual stresses were measured for four girders, with the remaining girder tests and residual stress measurements to be completed in subsequent research projects. Results of the large-scale tests were separated into two main categories for analysis: girder capacity and girder displacement. Within each category, the effect of relevant parameters, such as initial geometric imperfections, residual stresses, and geometric properties, were considered. To determine whether inelastic LTB occurred, the measured residual stresses were used in combination with mid-span surface strain measurements to analyse the stress distribution of the top flange at buckling. Finally, the test results were compared against the predicted moment resistances of three design equations, with a primary focus on CSA S16-14. The predicted resistances from CSA S16-14 were furthermore adjusted to account for load height effects due to point loads being above the shear centre. The results of the analyses were used to perform an evaluation of the CSA S16-14 provisions for LTB resistance.

## 6.2 Conclusions

The conclusions drawn from this research are:

- In numerical simulations of LTB, assuming an initial lateral out-of-straightness of  $L/1000$  is likely too severe, as this is the permissible limit and not a representative value (the mean measured top flange lateral out-of-straightness value in the current research was  $L/5500$ ).
- Flange stress analysis was used to determine whether inelastic LTB occurred in four of the test girders (as only four sets of residual stress distributions were available). The results of the analysis showed that three girders failed in inelastic LTB and one failed in elastic LTB, despite the prediction by the current code, where inelastic LTB was expected for all tested girders.
- The ratio  $M_{\max}/M_p$  may not be an accurate parameter for delimiting the boundary between elastic and inelastic LTB behaviour, as the flange stress analysis indicated G8-430-25-2-p failed in inelastic LTB but its  $M_{\max}/M_p$  ratio fell within the CSA S16-14 specified elastic range.

- The plasma-cut residual stress distributions resulted in compressive stresses at the flange tips, while tensile stresses were measured at the flange tips in the flame-cut girder. In both cases, the measured stresses were small.
- The observed effect of plasma- versus flame-cutting on LTB resistance was insignificant. However, the small measured residual stresses at the compression flange tips may have attributed to the near-identical resistances obtained.
- The CSA S16-14 predictions, adjusted to account for load height, match reasonably with the test results for girders with initial lateral out-of-straightness values less than  $L/3300$ .
- Initial geometric imperfections appear to influence girder displacement behaviour and LTB resistance, but the observed relationships did not follow a discernible trend.
- The ratio of lateral-to-vertical displacement at buckling ( $\delta_h/\delta_v$ ) is a girder response that is indicative the member's lateral stiffness. Though the factors affecting  $\delta_h/\delta_v$  are difficult to define, the results suggest that it may be related to initial geometric imperfections, as the girder with the largest initial top flange sweep and twist also exhibited the largest  $\delta_h/\delta_v$ .
- The extent to which CSA S16-14 over-predicts member resistance increases as  $\delta_h/\delta_v$  increases, which indicates that CSA S16-14's predictions are affected by the displacement response at buckling.

### 6.3 Recommendations for Further Research

The current research improves the understanding of LTB behaviour in modern welded girders through an experimental testing programme. However, further study of the following subjects would be beneficial for evaluating the adequacy of the CSA S16-14 provisions for LTB resistance more comprehensively:

- The effect of loading above the top flange was approximated using three methods from the literature, but a more rigorous approach is recommended by means of detailed numerical simulations of the test girders, with load height, measured residual stresses, measured geometric imperfections, and measured material properties considered in the model. Once the model is verified against test results, equivalent moment resistances for shear centre loading can be obtained, which can be used to compare against the CSA S16-14 provisions that similarly assume shear centre loading.

- The ratio of lateral-to-vertical displacement at buckling,  $\delta_h/\delta_v$ , appears to affect LTB resistance, but it is unclear what parameters affect  $\delta_h/\delta_v$  most. The test results indicate that it may be related to initial geometric imperfections, but further research is necessary.
- Further physical testing would be beneficial to the mandate of improving resistance characterisation of LTB in welded girders. Test specimens with larger aspect ratios ( $d/b$ ) are recommended, as well as sections with higher  $M/M_p$  ratios. Different loading configurations, such as bracing at the load point to remove the effect of load height, are also suggested. As LTB is a stability-related failure mode that is affected by numerous parameters, an increased number of up-to-date tests creates a larger database from which conclusions can be drawn.

## REFERENCES

- AASHTO. (2015). *AASHTO LRFD Bridge Design Specifications*. American Association of State Highway and Transportation Officials, Washington, DC.
- AISC. (2010). *ANSI/AISC 360-10 Specification for Structural Steel Buildings*. American Institute of Steel Construction, Chicago, IL.
- AISC. (2016). *ANSI/AISC 360-16 Specification for Structural Steel Buildings*. American Institute of Steel Construction, Chicago, IL.
- Alberta Transportation. (2017). *Standard Specifications for Bridge Construction*. Bridge Engineering Technical Standards Branch, Alberta Transportation, Edmonton, AB.
- Alpsten, G. A., and Tall, L. (1970). “Residual Stresses in Heavy Welded Shapes.” *Welding Journal*, 49(3), 93–105.
- Arasaratnam, P. (2005). “Characteristics and Behavior of Plasma Cut-Welded H-Shaped Steel Columns.” M.ASc. Thesis, McMaster University.
- ASTM International. (2018). *A370-18 Standard Test Methods and Definitions for Mechanical Testing of Steel Products*. West Conshohocken, PA.
- AWS. (2010). *Structural Welding Code–Steel, AWS D1.1/D1.1M*. American Welding Society Committee on Structural Welding.
- AWS. (2015). *Structural Welding Code–Steel, AWS D1.1/ D1.1M*. American Welding Society Committee on Structural Welding.
- Baker, K. A., and Kennedy, D. J. L. (1984). “Resistance factors for laterally unsupported steel beams and biaxially loaded steel beam columns.” *Canadian Journal of Civil Engineering*, 11(4), 1008–1019.
- Ballio, G., and Mazzolani, F. (1983). *Theory and design of steel structures*. Chapman and Hall, New York, NY.
- Boissonnade, N., and Somja, H. (2012). “Influence of Imperfections in FEM Modeling of Lateral Torsional Buckling Influence of Imperfections in FEM Modeling of Lateral Torsional Buckling.” *Annual Stability Conference*, Structural Stability Research Council, Grapevine, TX, 1–15.

- CEN. (2005). *Eurocode 3: Design of steel structures - Part 1-1: General rules and rules for buildings, EN 1993-1-1:2005:E*. European Committee for Standardization, Brussels, Belgium.
- Chernenko, D. E., and Kennedy, D. J. L. (1991). “An analysis of the performance of welded wide flange columns.” *Canadian Journal of Civil Engineering*, 18(4), 537–555.
- CISC. (2014). *Handbook of Steel Construction*. Canadian Institute of Steel Construction, Markham, ON.
- CSA. (2001). *CSA S16-01 Design of Steel Structures*. Canadian Standards Association, Toronto, ON.
- CSA. (2009). *CSA S16-09 Design of Steel Structures*. Canadian Standards Association, Toronto, ON.
- CSA. (2013a). *W59-13 Welded steel construction (metal arc welding)*. Canadian Standards Association, Mississauga, ON.
- CSA. (2013b). *CSA G40.20-13/G40.21-13 General requirements for rolled or welded structural quality steel/Structural quality steel*. Canadian Standards Association, Mississauga, ON.
- CSA. (2014a). *CSA S16-14 Design of Steel Structures*. Canadian Standards Association, Toronto, ON.
- CSA. (2014b). *CSA S6-14 Canadian Highway Bridge Design Code*. Canadian Standards Association, Mississauga, ON.
- CSI. (2015). “SAP2000 v14.” Computers and Structures, Inc., Walnut Creek, CA.
- Dassault Systèmes. (2010). *Abaqus Analysis User’s Manual (6.14)*. Providence, RI.
- Dassault Systèmes. (2014). “Abaqus Version 6.14.” Dassault Systèmes Simulia Corp., Providence, RI.
- Dibley, J. E. (1969). “Lateral torsional buckling of I-sections in Grade 55 steel.” *Proceedings of the Institution of Civil Engineers*, 43(4), 599–627.
- Driver, R. G., Kulak, G. L., Elwi, A. E., and Kennedy, D. J. L. (1997). “Seismic behaviour of steel plate shear walls.” Structural Engineering Report No. 215, University of Alberta, Edmonton, AB.

- Dux, P. F., and Kitipornchai, S. (1983). “Inelastic Beam Buckling Experiments.” *Journal of Constructional Steel Research*, 3(1), 3–9.
- Essa, H. S., and Kennedy, D. J. L. (1993). *Distortional Buckling of Steel Beams*. Structural Engineering Report No. 185, University of Alberta, Edmonton, AB.
- European Convention for Constructional Steelwork. (1977). *Second International Colloquium on Stability 1976/77: Introductory Report*. Tokyo, Liege, Washington.
- Fukumoto, Y. (1976). *Lateral buckling of welded beams and girders in HT 80 steel*. IABSE Congress Report, Zürich, Switzerland.
- Fukumoto, Y., and Itoh, Y. (1981). “Statistical study of experiments on welded beams.” *ASCE Journal of Structural Division*, 107(1), 89–103.
- Fukumoto, Y., Itoh, Y., and Kubo, M. (1980). “Strength variation of laterally unsupported beams.” *ASCE Journal of Structural Division*, 106((ST1)), 165–181.
- Fukumoto, Y., and Kubo, M. (1977). “An experimental review of lateral buckling of beams and girders.” *International Colloquium on Stability of Structures Under Static and Dynamic Loads*, American Society of Civil Engineers, Washington, DC, 541–562.
- Galambos, T. V. (1998). *Guide to stability design criteria for metal structures*. 5th Ed., John Wiley & Sons, Inc., New York.
- Galambos, T. V., and Ketter, R. L. (1959). “Columns under combined bending and thrust.” *Journal of the Engineering Mechanics Division*, 85(2), 134–152.
- Greiner, R., and Kaim, P. (2001). *Comparison of LT-buckling design curves with test results*. ECCS TC8, Report 23. European Convention for Constructional Steelwork, Brussels, Belgium.
- Greiner, R., Salzgeber, G., and Ofner, R. (2001). *New lateral torsional buckling curves  $\kappa_{LT}$  - numerical simulations and design formulae*. ECCS TC8, Report 30. European Convention for Constructional Steelwork, Brussels, Belgium.
- Helwig, T. A., Frank, K. H., and Yura, J. A. (1997). “Lateral-Torsional Buckling of Singly Symmetric I-Beams.” *Journal of Structural Engineering American Society of Civil Engineers*, 123(2), 1172–1179.
- Kabir, I., and Bhowmick, A. K. (2018). “Lateral torsional buckling of welded wide flange beams

- under constant moment.” *Canadian Journal of Civil Engineering*, 45(2018), 766–779.
- Kabir, M. I., and Bhowmick, A. K. (2016). “Lateral torsional buckling of welded wide flange beams.” M.ASc. Thesis, Concordia University.
- Kim, Y. D. (2010). “Behavior and design of metal building frames using general prismatic and web-tapered steel I-section members.” Doctoral Dissertation, Georgia Institute of Technology.
- MacPhedran, I., and Grondin, G. Y. (2011). “A simple steel beam design curve.” *Canadian Journal of Civil Engineering*, 38(2), 141–153.
- Mathworks. (2017). “MATLAB R2017a.” The MathWorks Inc., Natick, MA.
- McFalls, R. K., and Tall, L. (1970). “A Study of Welded Columns Manufactured from Flame-Cut Plates.” *AWS Welding Journal*, 49(4), 141s-153s.
- Nethercot, D. A. (1974). “Residual stresses and their influence upon the lateral buckling of rolled steel beams.” *The Structural Engineer*, 52(3), 89–96.
- Nethercot, D. A., and Rockey, K. C. (1971). “A unified approach to the elastic lateral buckling of beams.” *The Structural Engineer*, 49(7), 321–330.
- Pekoz, T., Bjorhovde, R., Errera, S. J., Johnston, B. G., Sherman, D. R., and Tall, L. (1981). “Determination of Residual Stresses in Structural Shapes.” *Experimental Mechanics*, 5(3), 4–7.
- Richter, J. F. (1998). “Flexural capacity of slender web plate girders.” M.Sc. Thesis, University of Texas.
- Standards Australia. (1998). *AS 4100-1998 Steel Structures*. SAI Global Limited, Sydney, Australia.
- Subramanian, L., and White, D. W. (2017). “Resolving the disconnects between lateral torsional buckling experimental tests, test simulations and design strength equations.” *Journal of Constructional Steel Research*, Elsevier Ltd, 128, 321–334.
- Tall, L. (1966). *Welded built-up columns*. Fritz Engineering Laboratory Report No. 249.29, Lehigh University, Bethlehem, PA.
- Timoshenko, S. P., and Gere, J. M. (1961). *Theory of elastic stability*. McGraw-Hill, New York.

- Unsworth, D. R., Driver, R. G., and Li, L. (2019). *Characterization of Residual Stresses in Modern Welded Girders*. Steel Centre Engineering Report No. 014, University of Alberta, Edmonton, AB.
- White, D. W. (2008). “Unified Flexural Resistance Equations for Stability Design of Steel I-Section Members: Overview.” *Journal of Structural Engineering American Society of Civil Engineers*, 134(9), 1405–1424.
- White, D. W., and Jung, S. K. (2004). *Unified flexural resistance equations for stability design of steel I-section Members – Uniform Bending Tests*. Structural Engineering, Mechanics and Materials Report No. 04-28, Georgia Institute of Technology, Atlanta, GA.
- Wong-Chung, A. D., and Kitipornchai, S. (1987). “Partially braced inelastic beam buckling experiments.” *Journal of Constructional Steel Research*, 7(3), 189–211.
- Wong, E., Driver, R. G., and Heal, T. W. (2015). “Simplified approach to estimating the elastic lateral–torsional buckling capacity of steel beams with top-flange loading.” *Canadian Journal of Civil Engineering*, 138(February), 130–138.
- Yang, B., Zhu, Q., Nie, S., Elchalakani, M., and Xiong, G. (2018). “Experimental and model investigation on residual stresses in Q460GJ thick-walled I-shaped sections.” *Journal of Constructional Steel Research*, Elsevier Ltd, 145(June 2018), 489–503.
- Yarimci, E., Yura, J. A., and Lu, L. W. (1967). “Techniques for testing structures permitted to sway.” *Experimental Mechanics*, (August 1967), 321–331.
- Ziemian, R. D. (2010). *Guide to Stability Design Criteria for Metal Structures*. 6th Ed., John Wiley & Sons, Inc., Hoboken, NJ.

## Appendix A: Test Girder Drawings

DWG SHEET LIST

S.0	TITLE PAGE & GENERAL NOTES
S.1	SP1 - PLASMA CUT
S.2.1	SP2 - PLASMA CUT
S.2.2	SP2 - FLAME CUT
S.3	SP3 - PLASMA CUT
S.4	SP4 - PLASMA CUT
S.5	SP5 - PLASMA CUT
S.6	SP6 - PLASMA CUT
S.7.1	SP7 - PLASMA CUT
S.7.2	SP7 - FLAME CUT
S.8	SP8 - FLAME CUT
S.9	SP9 - FLAME CUT

**GENERAL NOTES**

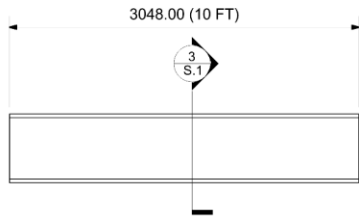
- ALL DIMENSIONS ARE IN MILLIMETERS UNLESS NOTED OTHERWISE (UNO).
- ALL DRAWINGS TO BE PLOTTED ON 11" X 17" PAPER.
- DO NOT SCALE DRAWINGS. FOR ANY CLARIFICATIONS, CONTACT:  
  
 DIMPLE JI  
 (780) 668-8637  
 XLJI@UALBERTA.CA  
  
 ROBERT DRIVER  
 RDRIVER@UALBERTA.CA  
  
 ALI IMANPOUR  
 IMANPOUR@UALBERTA.CA
- SHOP DRAWINGS SHALL BE PROVIDED FOR REVIEW PRIOR TO FABRICATION.
- G40.21 350W TO BE USED FOR ALL STEEL.
- PROVIDE A COPY OF MILL TEST REPORT FOR ALL STRUCTURAL STEEL USED IN DWGS S.1 TO S.9.
- PROVIDE A COPY OF WELDING PROCEDURE DATASHEET FOR ALL TEST GIRDERS IN DWGS S.1 TO S.9.
- ALL WELDS TO USE MATCHING ELECTRODE FOR G40.21 350W.
- ALL WELDS TO BE CONTINUOUS.
- CUTTING METHOD (PLASMA OR FLAME CUT) FOR INDIVIDUAL PLATES IS SPECIFIED IN EACH DWG SHEET.
- TEST GIRDERS SHALL ONLY COMPRISE CONTINUOUS PLATES; NO SHOP SPLICES ARE PERMITTED.
- DIMENSIONAL TOLERANCES SHALL MEET ALL REQUIREMENTS OF W59-13.
- DEVIATION FROM STRAIGHTNESS FOR 10363.20 MM (34 FT) LONG GIRDERS SHOULD NOT EXCEED L/1000 MM FOR WEBS AND FLANGES. RECORD OUT-OF-STRAIGHTNESS VALUES FOR ALL 10363.20 MM (34 FT) GIRDERS. SHOULD OUT-OF-STRAIGHTNESS EXCEED L/1000 MM, THE STRAIGHTENING PROCEDURE FOR EACH GIRDER MUST BE DOCUMENTED.
- UNIVERSITY OF ALBERTA STUDENT (CONTACT INFORMATION BELOW) TO BE PRESENT TO DOCUMENT STEPS OF GIRDER ASSEMBLY. THIS INCLUDES: WEB TO FLANGE WELD, WELD SEQUENCE, AND WELD DIRECTION.  
  
 DANIEL UNSWORTH  
 (780) 222-9123  
 DRUNSWOR@UALBERTA.CA
- ONE 4" X 20" PIECE FOR EACH PLATE THICKNESS (0.375", 0.5", 1", AND 1.25") TO BE CUT AND SHIPPED WITH GIRDERS. ROLLING DIRECTION TO BE MARKED PRIOR TO CUTTING. LONG DIMENSION TO BE PARALLEL TO ROLLING DIRECTION.



University of Alberta  
The Steel Centre  
LTB Test Girders

TITLE PAGE & GENERAL NOTES	
Date	01/05/2017
Drawn by	DJ
Checked by	AI, RGD, DU
Scale	
S.0	SHEET 1 of 12

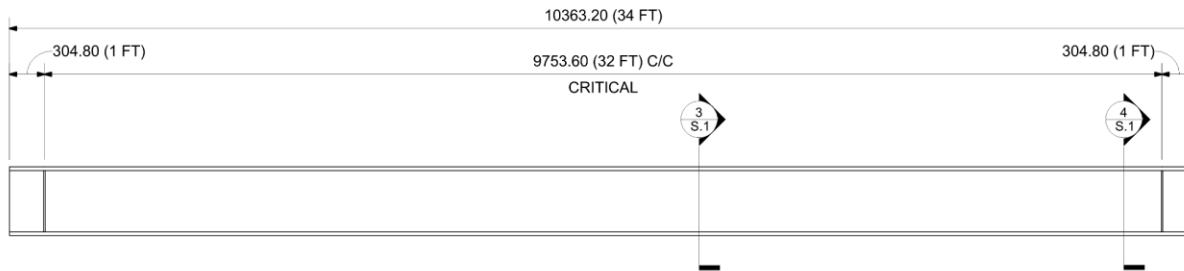
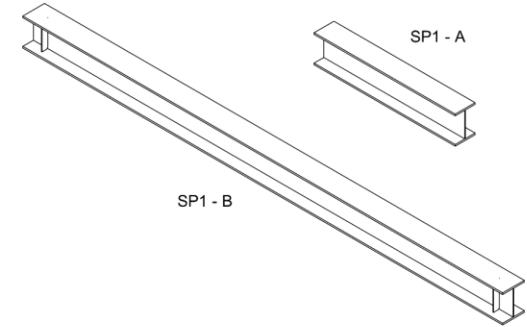
2018-03-23 2:30:57 PM



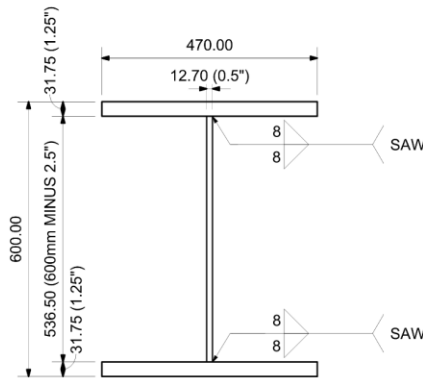
1 SP1 - A  
1:40

**NOTES**

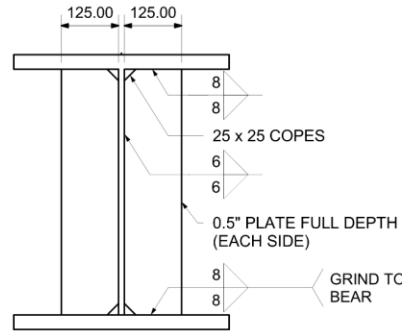
1. ALL INDIVIDUAL PLATES TO BE PLASMA CUT.
2. THE FLANGE PLATES OF SP1-A AND SP1-B TO BE CUT FROM A SINGLE STEEL PLATE. WEB PLATES ALSO TO BE CUT FROM A SINGLE STEEL PLATE.
3. WELDING METHOD AND WELDING PROCEDURE TO REMAIN CONSTANT BETWEEN SP1-A AND SP1-B.
4. ALL STIFFENERS TO BE WELDED ON BOTH SIDES.
5. USE CONTINUOUS SUBMERGED ARC WELDING (SAW) FOR WEB TO FLANGE WELDS.
6. UNIVERSITY OF ALBERTA STUDENT, DANIEL UNSWORTH, TO BE PRESENT DURING WEB TO FLANGE WELDING.



2 SP1 - B  
1:40



3 STEEL SECTION  
1:10



4 BEARING STIFFENER DETAILS (TYP)  
1:10



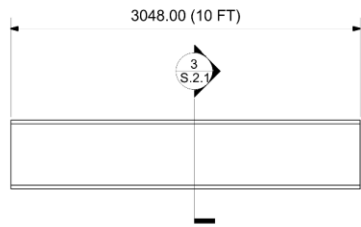
University of Alberta  
The Steel Centre  
LTB Test Girders

SP1 - PLASMA CUT  
1 REQUIRED

Date	01/05/2017
Drawn by	DJ
Checked by	AI, RGD
Scale	As indicated

S.1 SHEET  
2 of 12

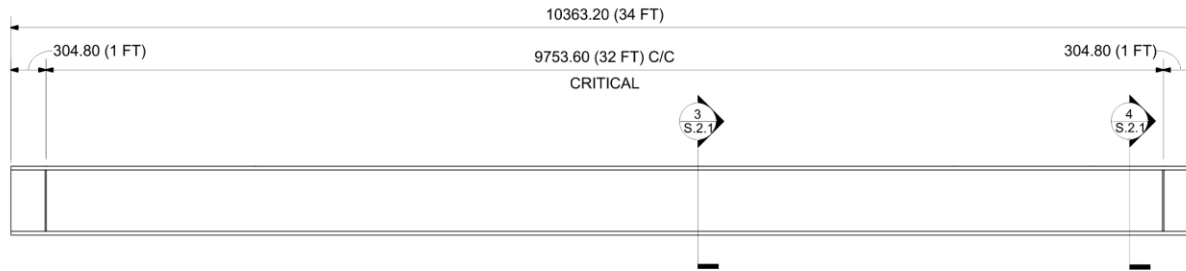
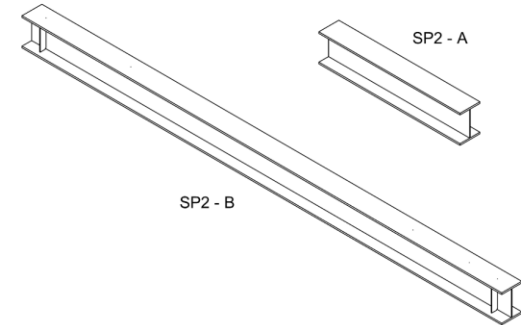
2018-03-23 2:30:58 PM



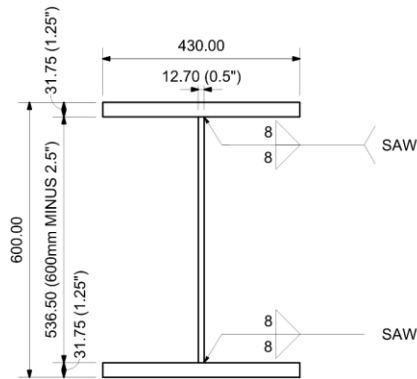
1 SP2 - A  
1 : 40

**NOTES**

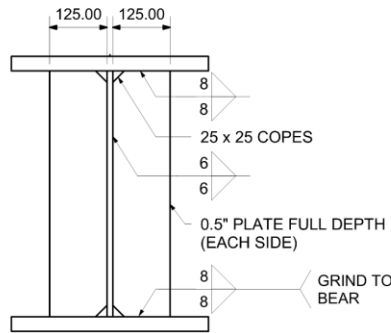
1. ALL INDIVIDUAL PLATES TO BE PLASMA CUT.
2. THE FLANGE PLATES OF SP2-A AND SP2-B TO BE CUT FROM A SINGLE STEEL PLATE. WEB PLATES ALSO TO BE CUT FROM A SINGLE STEEL PLATE.
3. WELDING METHOD AND WELDING PROCEDURE TO REMAIN CONSTANT BETWEEN SP2-A AND SP2-B.
4. ALL STIFFENERS TO BE WELDED ON BOTH SIDES.
5. USE CONTINUOUS SUBMERGED ARC WELDING (SAW) FOR WEB TO FLANGE WELDS.
6. UNIVERSITY OF ALBERTA STUDENT, DANIEL UNSWORTH, TO BE PRESENT DURING WEB TO FLANGE WELDING.



2 SP2 - B  
1 : 40



3 STEEL SECTION  
1 : 10



4 BEARING STIFFENER DETAILS (TYP)  
1 : 10



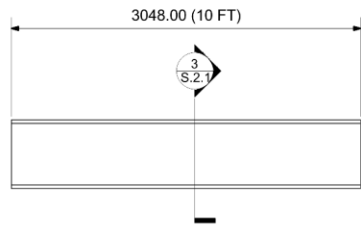
University of Alberta  
The Steel Centre  
LTB Test Girders

SP2 - PLASMA CUT  
1 REQUIRED

Date	01/05/2017
Drawn by	DJ
Checked by	AI, RGD
Scale	As indicated

S.2.1 SHEET  
3 of 12

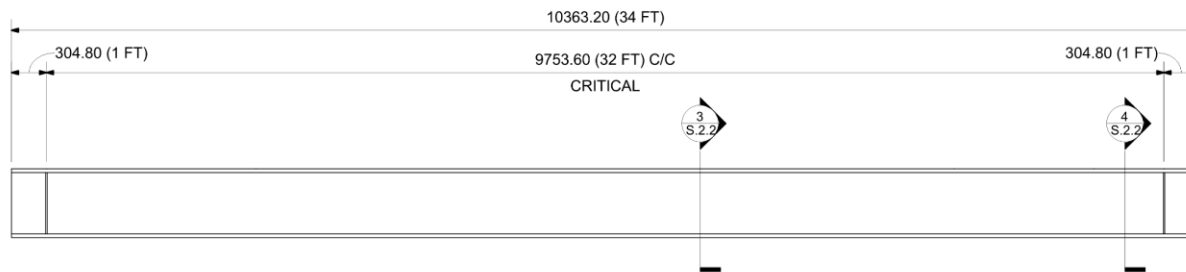
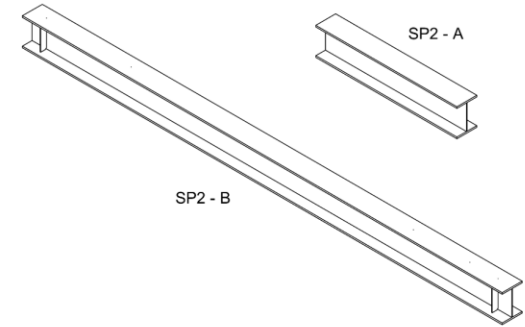
2018-03-23 2:30:56 PM



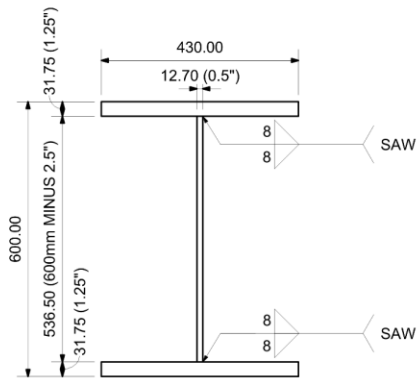
1 SP2 - A  
1 : 40

**NOTES**

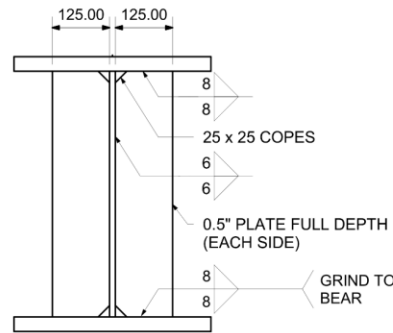
1. ALL INDIVIDUAL PLATES TO BE FLAME CUT.
2. THE FLANGE PLATES OF SP2-A AND SP2-B TO BE CUT FROM A SINGLE STEEL PLATE. WEB PLATES ALSO TO BE CUT FROM A SINGLE STEEL PLATE.
3. WELDING METHOD AND WELDING PROCEDURE TO REMAIN CONSTANT BETWEEN SP2-A AND SP2-B.
4. ALL STIFFENERS TO BE WELDED ON BOTH SIDES.
5. USE CONTINUOUS SUBMERGED ARC WELDING (SAW) FOR WEB TO FLANGE WELDS.
6. UNIVERSITY OF ALBERTA STUDENT, DANIEL UNSWORTH, TO BE PRESENT DURING WEB TO FLANGE WELDING.



2 SP2 - B  
1 : 40



3 STEEL SECTION  
1 : 10



4 BEARING STIFFENER DETAILS (TYP)  
1 : 10



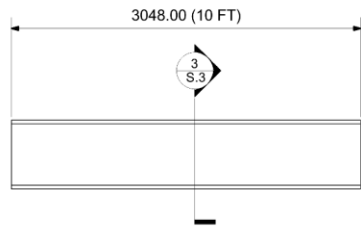
University of Alberta  
The Steel Centre  
LTB Test Girders

**SP2 - FLAME CUT  
1 REQUIRED**

Date	01/05/2017
Drawn by	DJ
Checked by	AI, RGD
Scale	As indicated

**S.2.2** SHEET  
4 of 12

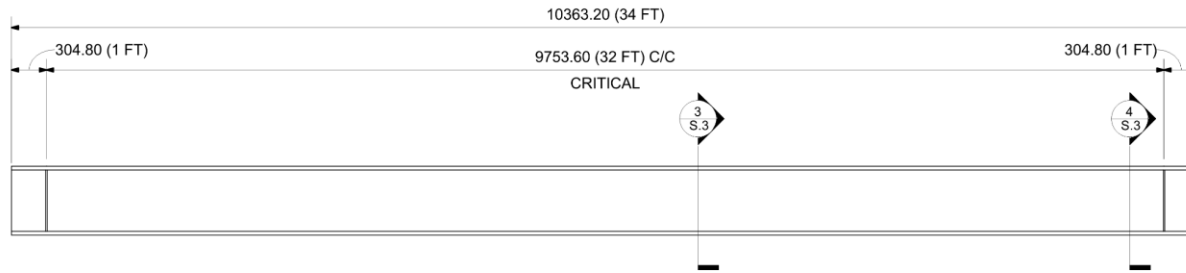
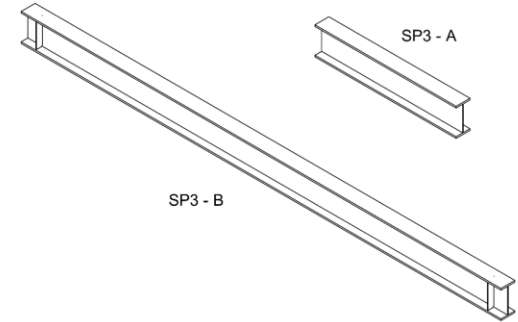
2018-03-23 2:30:59 PM



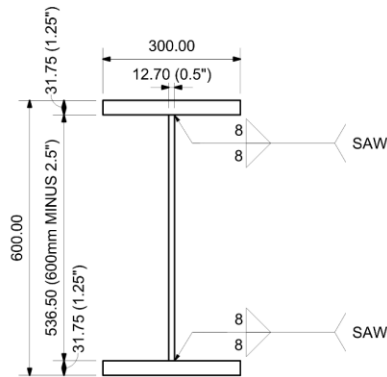
① SP3 - A  
1 : 40

**NOTES**

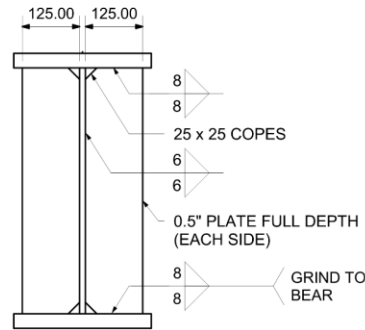
1. ALL INDIVIDUAL PLATES TO BE PLASMA CUT.
2. THE FLANGE PLATES OF SP3-A AND SP3-B TO BE CUT FROM A SINGLE STEEL PLATE. WEB PLATES ALSO TO BE CUT FROM A SINGLE STEEL PLATE.
3. WELDING METHOD AND WELDING PROCEDURE TO REMAIN CONSTANT BETWEEN SP3-A AND SP3-B.
4. ALL STIFFENERS TO BE WELDED ON BOTH SIDES.
5. USE CONTINUOUS SUBMERGED ARC WELDING (SAW) FOR WEB TO FLANGE WELDS.
6. UNIVERSITY OF ALBERTA STUDENT, DANIEL UNSWORTH, TO BE PRESENT DURING WEB TO FLANGE WELDING.



② SP3 - B  
1 : 40



③ STEEL SECTION  
1 : 10



④ BEARING STIFFENER DETAILS (TYP)  
1 : 10



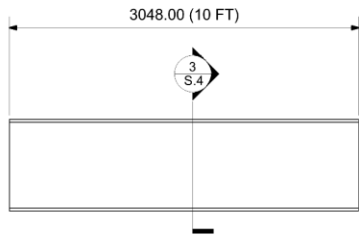
University of Alberta  
The Steel Centre  
LTB Test Girders

SP3 - PLASMA CUT  
1 REQUIRED

Date	01/05/2017
Drawn by	DJ
Checked by	AI, RGD
Scale	As indicated

**S.3** SHEET  
5 of 12

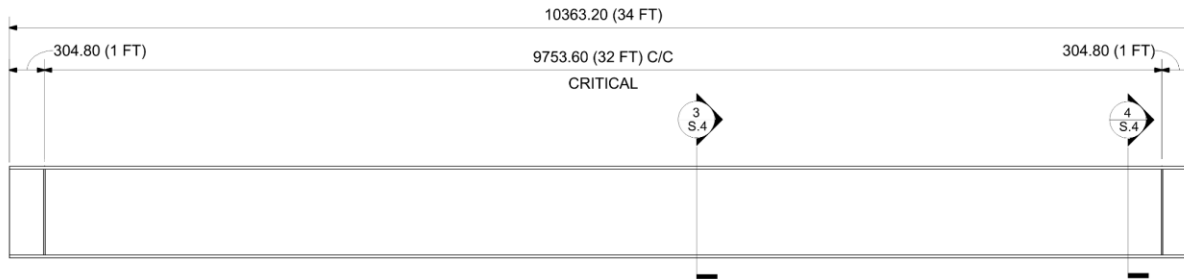
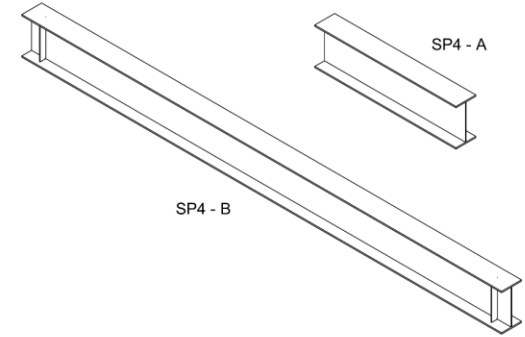
2018-03-23 2:30:59 PM



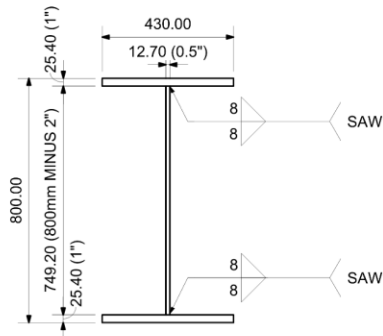
1 SP4 - A  
1:40

**NOTES**

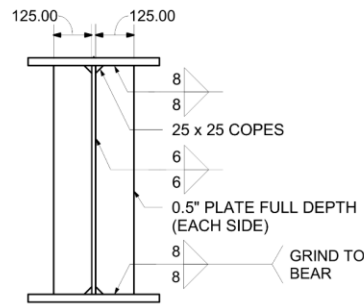
1. ALL INDIVIDUAL PLATES TO BE PLASMA CUT.
2. THE FLANGE PLATES OF SP4-A AND SP4-B TO BE CUT FROM A SINGLE STEEL PLATE. WEB PLATES ALSO TO BE CUT FROM A SINGLE STEEL PLATE.
3. WELDING METHOD AND WELDING PROCEDURE TO REMAIN CONSTANT BETWEEN SP4-A AND SP4-B.
4. ALL STIFFENERS TO BE WELDED ON BOTH SIDES.
5. USE CONTINUOUS SUBMERGED ARC WELDING (SAW) FOR WEB TO FLANGE WELDS.
6. UNIVERSITY OF ALBERTA STUDENT, DANIEL UNSWORTH, TO BE PRESENT DURING WEB TO FLANGE WELDING.



2 SP4 - B  
1:40



3 STEEL SECTION  
1:15



4 BEARING STIFFENER DETAILS (TYP)  
1:15



University of Alberta  
The Steel Centre  
LTB Test Girders

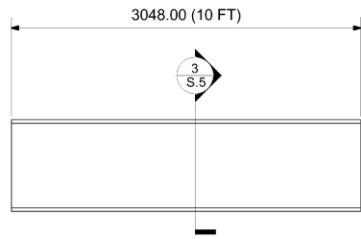
SP4 - PLASMA CUT  
1 REQUIRED

Date	01/05/2017
Drawn by	DJ
Checked by	AI, RGD
Scale	As indicated

**S.4**

SHEET  
6 of 12

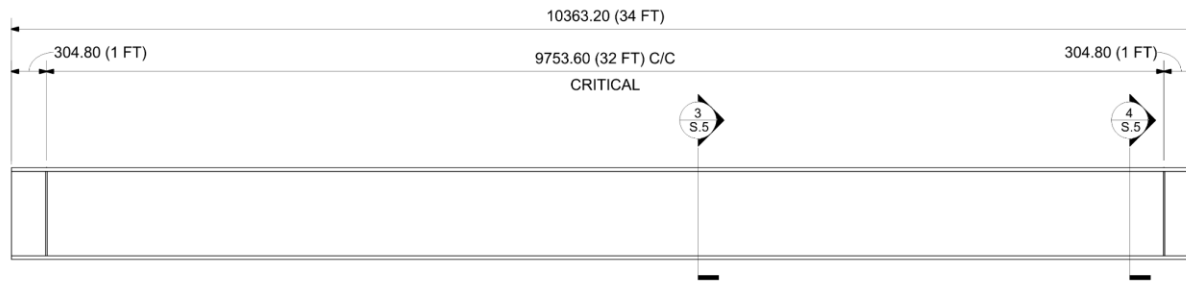
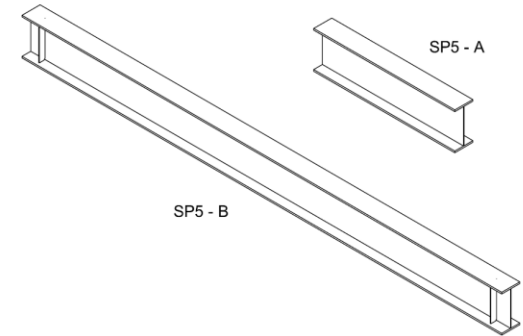
2018-03-23 2:30:59 PM



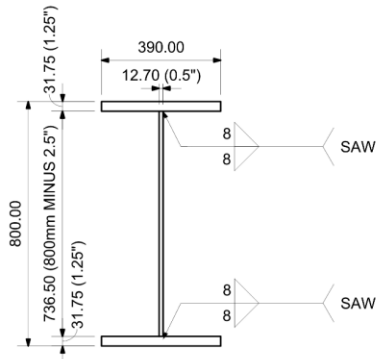
1 SP5 - A  
1 : 40

**NOTES**

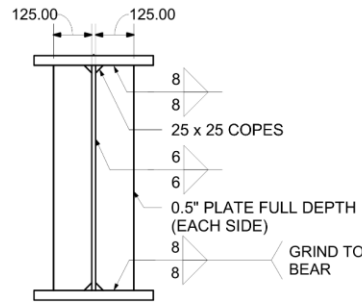
1. ALL INDIVIDUAL PLATES TO BE PLASMA CUT.
2. THE FLANGE PLATES OF SP5-A AND SP5-B TO BE CUT FROM A SINGLE STEEL PLATE. WEB PLATES ALSO TO BE CUT FROM A SINGLE STEEL PLATE.
3. WELDING METHOD AND WELDING PROCEDURE TO REMAIN CONSTANT BETWEEN SP5-A AND SP5-B.
4. ALL STIFFENERS TO BE WELDED ON BOTH SIDES.
5. USE CONTINUOUS SUBMERGED ARC WELDING (SAW) FOR WEB TO FLANGE WELDS.
6. UNIVERSITY OF ALBERTA STUDENT, DANIEL UNSWORTH, TO BE PRESENT DURING WEB TO FLANGE WELDING.



2 SP5 - B  
1 : 40



3 STEEL SECTION  
1 : 15



4 BEARING STIFFENER DETAILS (TYP)  
1 : 15



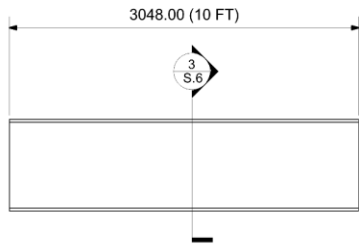
University of Alberta  
The Steel Centre  
LTB Test Girders

SP5 - PLASMA CUT  
1 REQUIRED

Date	01/05/2017
Drawn by	DJ
Checked by	AI, RGD
Scale	As indicated

**S.5** SHEET  
7 of 12

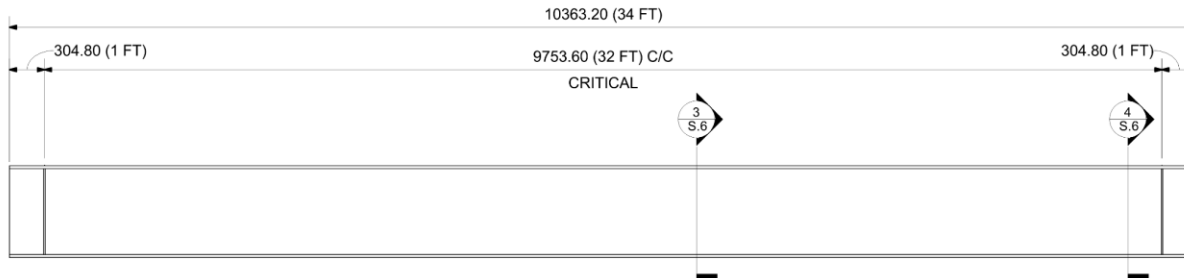
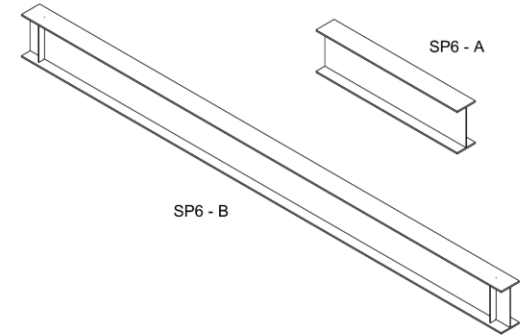
2018-03-23 2:31:00 PM



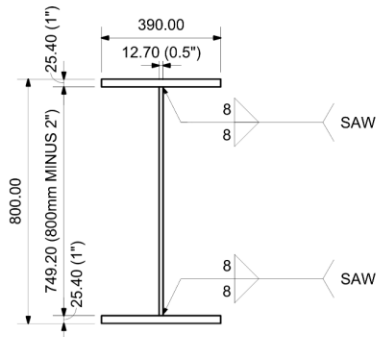
1 SP6 - A  
1 : 40

**NOTES**

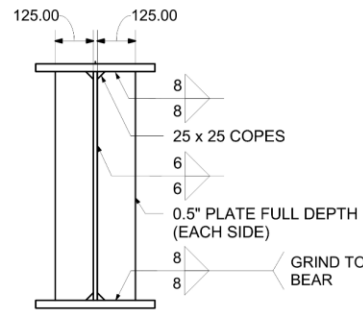
1. ALL INDIVIDUAL PLATES TO BE PLASMA CUT.
2. THE FLANGE PLATES OF SP6-A AND SP6-B TO BE CUT FROM A SINGLE STEEL PLATE. WEB PLATES ALSO TO BE CUT FROM A SINGLE STEEL PLATE.
3. WELDING METHOD AND WELDING PROCEDURE TO REMAIN CONSTANT BETWEEN SP6-A AND SP6-B.
4. ALL STIFFENERS TO BE WELDED ON BOTH SIDES.
5. USE CONTINUOUS SUBMERGED ARC WELDING (SAW) FOR WEB TO FLANGE WELDS.
6. UNIVERSITY OF ALBERTA STUDENT, DANIEL UNSWORTH, TO BE PRESENT DURING WEB TO FLANGE WELDING.



2 SP6 - B  
1 : 40



3 STEEL SECTION  
1 : 15



4 BEARING STIFFENER DETAILS (TYP)  
1 : 15



University of Alberta  
The Steel Centre  
LTB Test Girders

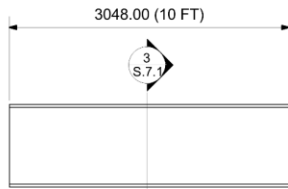
SP6 - PLASMA CUT  
1 REQUIRED

Date	01/05/2017
Drawn by	DJ
Checked by	AI, RGD
Scale	As indicated

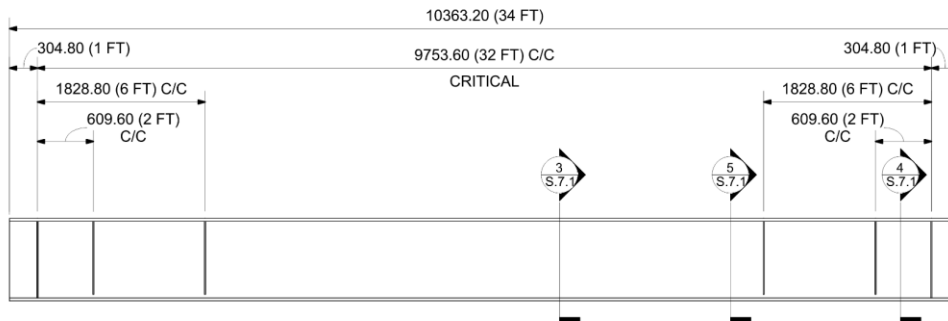
**S.6**

SHEET  
8 of 12

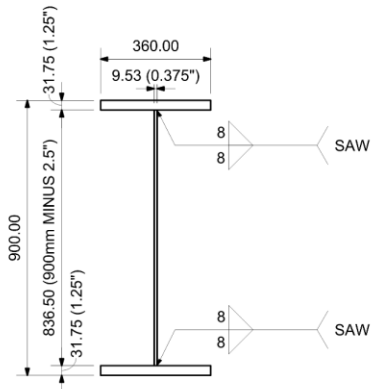
2018-03-23 2:31:00 PM



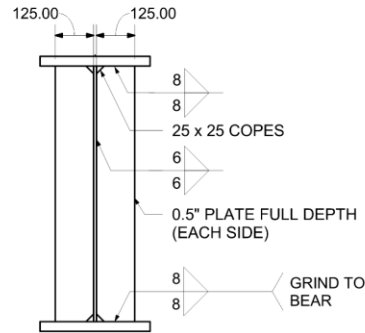
1 SP7 - A  
1 : 50



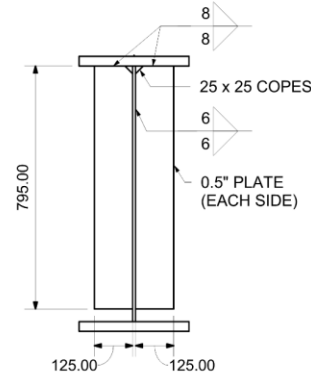
2 SP7 - B  
1 : 50



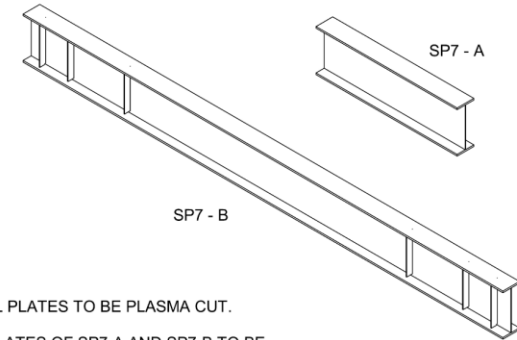
3 STEEL SECTION  
1 : 15



4 BEARING STIFFENER DETAILS (TYP)  
1 : 15



5 TRANSVERSE STIFFENER DETAILS (TYP)  
1 : 15



**NOTES**

1. ALL INDIVIDUAL PLATES TO BE PLASMA CUT.
2. THE FLANGE PLATES OF SP7-A AND SP7-B TO BE CUT FROM A SINGLE STEEL PLATE. WEB PLATES ALSO TO BE CUT FROM A SINGLE STEEL PLATE.
3. WELDING METHOD AND WELDING PROCEDURE TO REMAIN CONSTANT BETWEEN SP7-A AND SP7-B.
4. ALL STIFFENERS TO BE WELDED ON BOTH SIDES.
5. USE CONTINUOUS SUBMERGED ARC WELDING (SAW) FOR WEB TO FLANGE WELDS.
6. UNIVERSITY OF ALBERTA STUDENT, DANIEL UNSWORTH, TO BE PRESENT DURING WEB TO FLANGE WELDING.



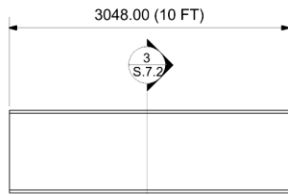
University of Alberta  
The Steel Centre  
LTB Test Girders

SP7 - PLASMA CUT  
1 REQUIRED

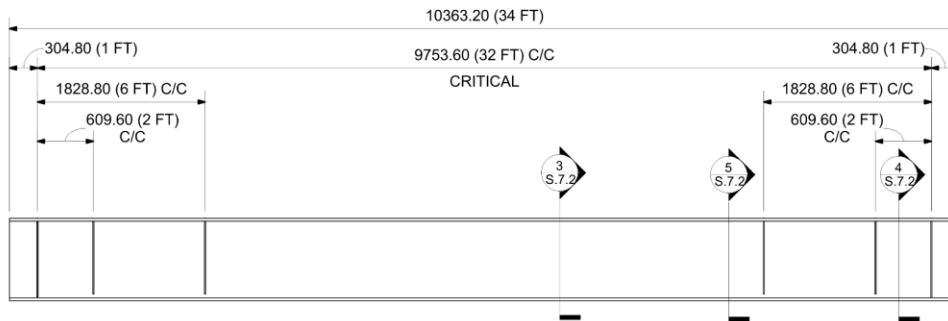
Date	01/05/2017
Drawn by	DJ
Checked by	AI, RGD
Scale	As indicated

**S.7.1** SHEET  
9 of 12

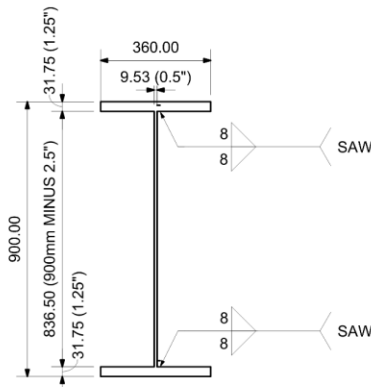
2018-03-23 2:31:01 PM



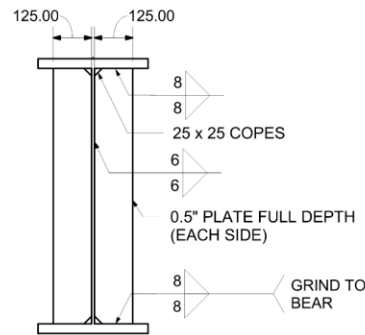
1 SP7 - A  
1: 50



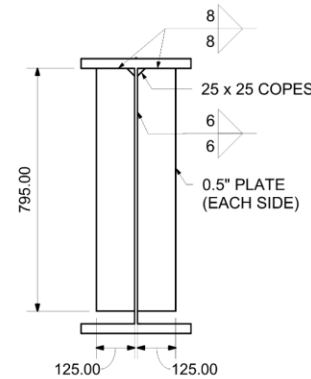
2 SP7 - B  
1: 50



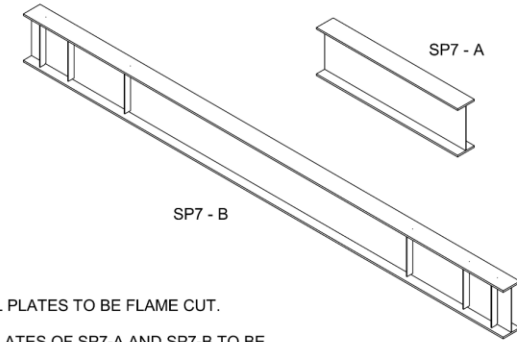
3 STEEL SECTION  
1: 15



4 BEARING STIFFENER DETAILS (TYP)  
1: 15



5 TRANSVERSE STIFFENER DETAILS (TYP)  
1: 15



**NOTES**

1. ALL INDIVIDUAL PLATES TO BE FLAME CUT.
2. THE FLANGE PLATES OF SP7-A AND SP7-B TO BE CUT FROM A SINGLE STEEL PLATE. WEB PLATES ALSO TO BE CUT FROM A SINGLE STEEL PLATE.
3. WELDING METHOD AND WELDING PROCEDURE TO REMAIN CONSTANT BETWEEN SP7-A AND SP7-B.
4. ALL STIFFENERS TO BE WELDED ON BOTH SIDES.
5. USE CONTINUOUS SUBMERGED ARC WELDING (SAW) FOR WEB TO FLANGE WELDS.
6. UNIVERSITY OF ALBERTA STUDENT, DANIEL UNSWORTH, TO BE PRESENT DURING WEB TO FLANGE WELDING.



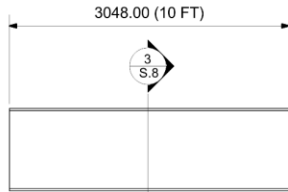
University of Alberta  
The Steel Centre  
LTB Test Girders

**SP7 - FLAME CUT  
1 REQUIRED**

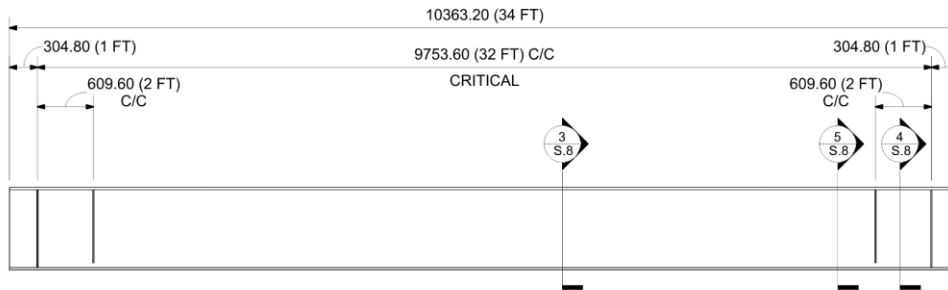
Date	01/05/2017
Drawn by	DJ
Checked by	AI, RGD
Scale	As indicated

**S.7.2** SHEET  
10 of 12

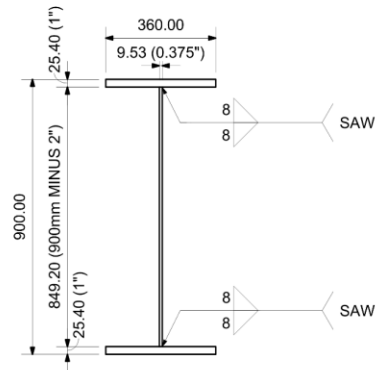
2018-09-23 2:31:01 PM



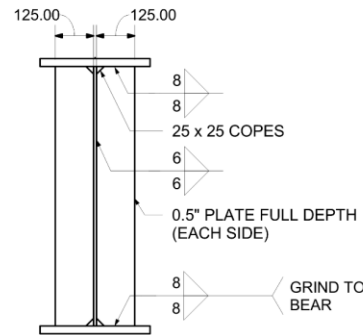
1 SP8 - A  
1 : 50



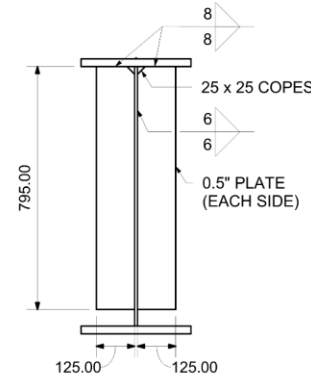
2 SP8 - B  
1 : 50



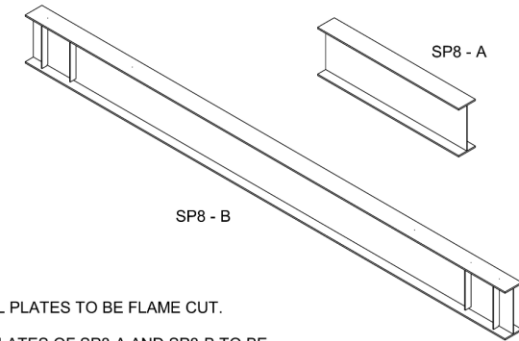
3 STEEL SECTION  
1 : 15



4 BEARING STIFFENER DETAILS (TYP)  
1 : 15



5 TRANSVERSE STIFFENER DETAILS (TYP)  
1 : 15



**NOTES**

1. ALL INDIVIDUAL PLATES TO BE FLAME CUT.
2. THE FLANGE PLATES OF SP8-A AND SP8-B TO BE CUT FROM A SINGLE STEEL PLATE. WEB PLATES ALSO TO BE CUT FROM A SINGLE STEEL PLATE.
3. WELDING METHOD AND WELDING PROCEDURE TO REMAIN CONSTANT BETWEEN SP8-A AND SP8-B.
4. ALL STIFFENERS TO BE WELDED ON BOTH SIDES.
5. USE CONTINUOUS SUBMERGED ARC WELDING (SAW) FOR WEB TO FLANGE WELDS.
6. UNIVERSITY OF ALBERTA STUDENT, DANIEL UNSWORTH, TO BE PRESENT DURING WEB TO FLANGE WELDING.



University of Alberta  
The Steel Centre  
LTB Test Girders

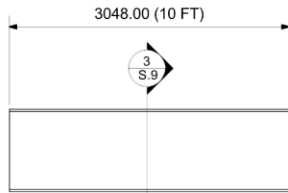
SP8 - FLAME CUT  
1 REQUIRED

Date	01/05/2017
Drawn by	DJ
Checked by	AI, RGD
Scale	As indicated

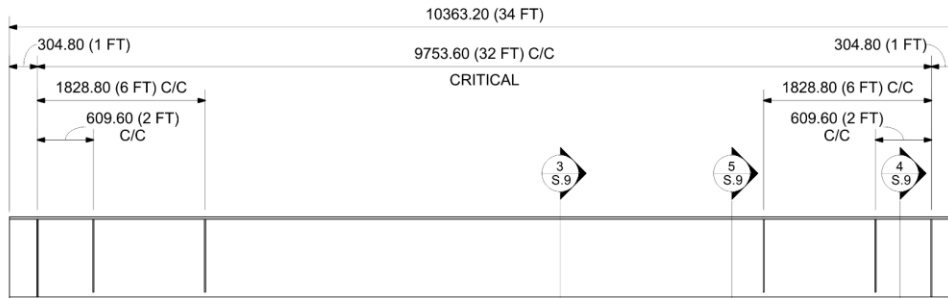
**S.8**

SHEET  
11 of 12

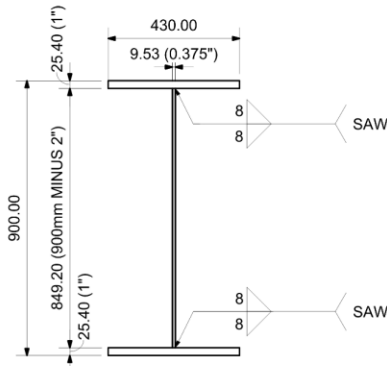
2018-03-23 2:31:01 PM



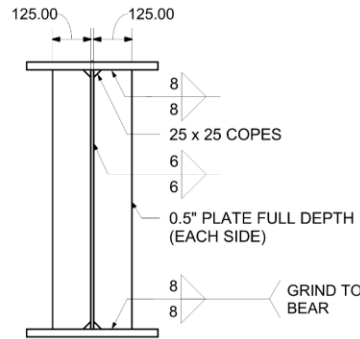
1 SP9 - A  
1: 50



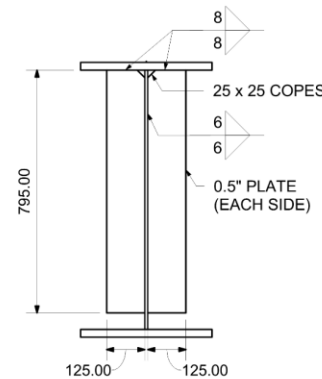
2 SP9 - B  
1: 50



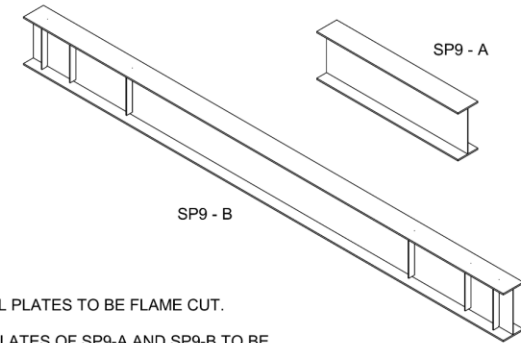
3 STEEL SECTION  
1: 15



4 BEARING STIFFENER DETAILS (TYP)  
1: 15



5 TRANSVERSE STIFFENER DETAILS (TYP)  
1: 15



**NOTES**

1. ALL INDIVIDUAL PLATES TO BE FLAME CUT.
2. THE FLANGE PLATES OF SP9-A AND SP9-B TO BE CUT FROM A SINGLE STEEL PLATE. WEB PLATES ALSO TO BE CUT FROM A SINGLE STEEL PLATE.
3. WELDING METHOD AND WELDING PROCEDURE TO REMAIN CONSTANT BETWEEN SP9-A AND SP9-B.
4. ALL STIFFENERS TO BE WELDED ON BOTH SIDES.
5. USE CONTINUOUS SUBMERGED ARC WELDING (SAW) FOR WEB TO FLANGE WELDS.
6. UNIVERSITY OF ALBERTA STUDENT, DANIEL UNSWORTH, TO BE PRESENT DURING WEB TO FLANGE WELDING.



University of Alberta  
The Steel Centre  
LTB Test Girders

SP9 - FLAME CUT  
1 REQUIRED

Date	01/05/2017
Drawn by	DJ
Checked by	AI, RGD
Scale	As indicated

**S.9**

SHEET  
12 of 12

2018-03-23 2:31:02 PM

## Appendix B: Measured Initial Geometric Imperfections

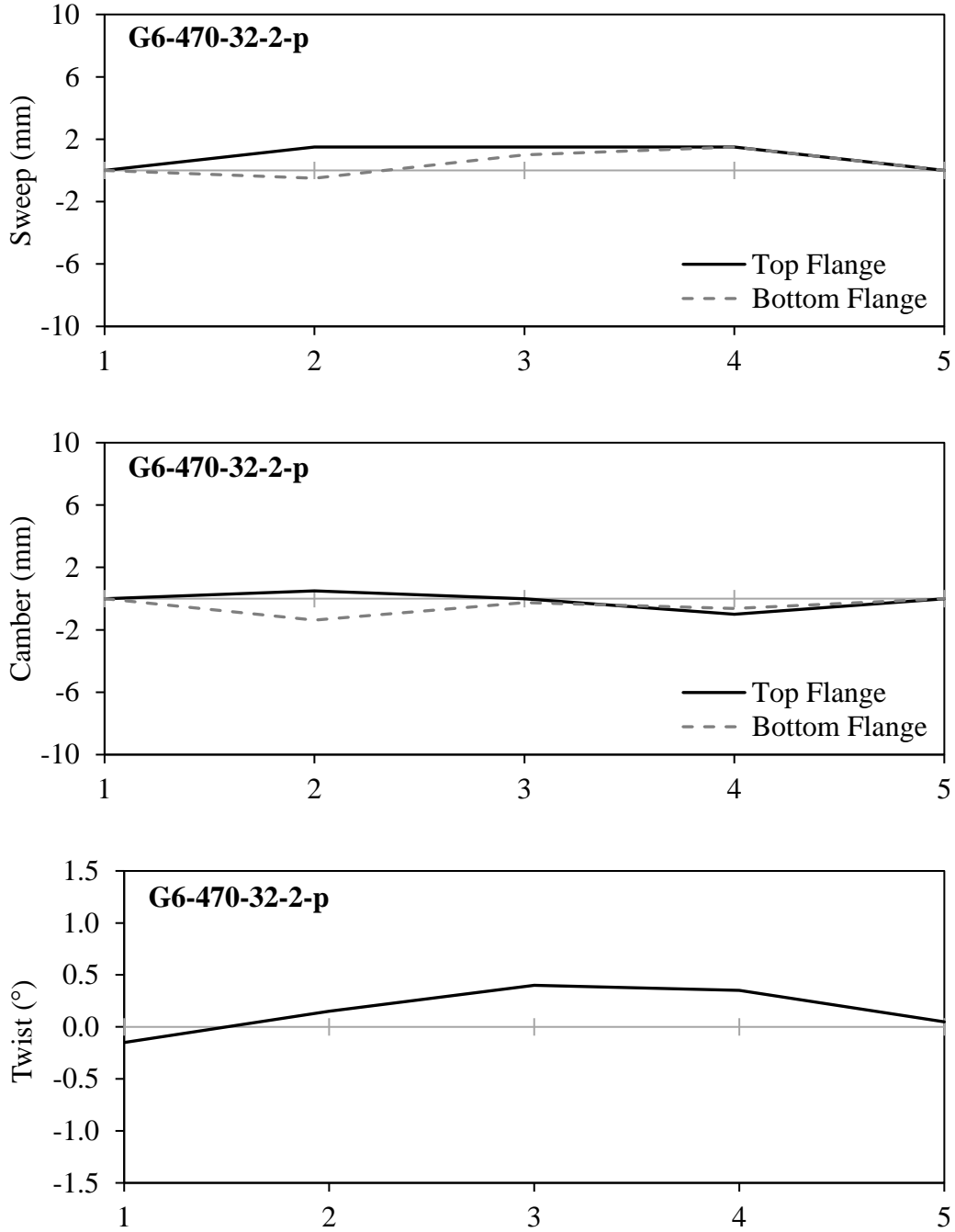


Figure B-1: Initial geometric imperfections of G6-470-32-2-p

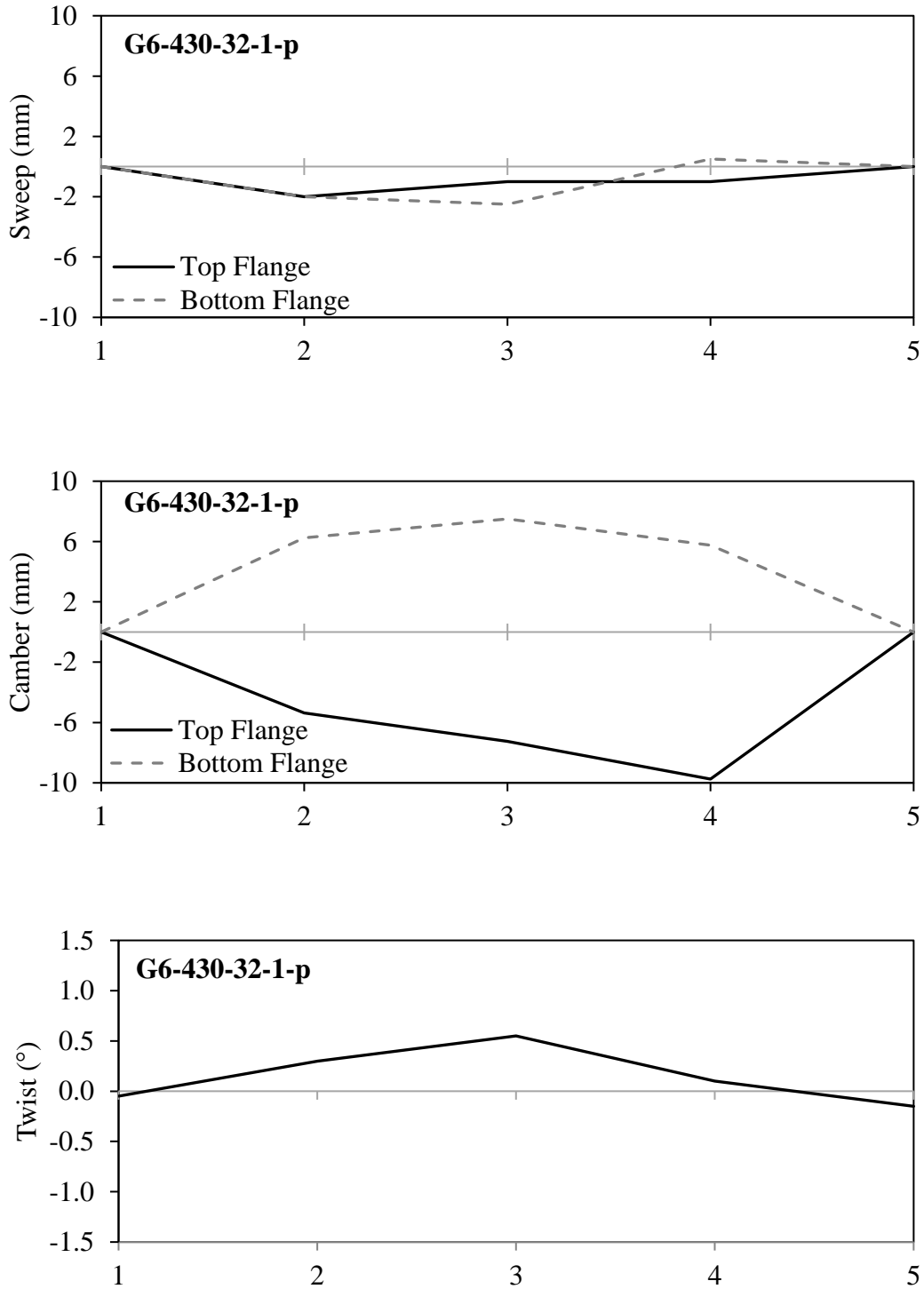


Figure B-2: Initial geometric imperfections of G6-430-32-1-p

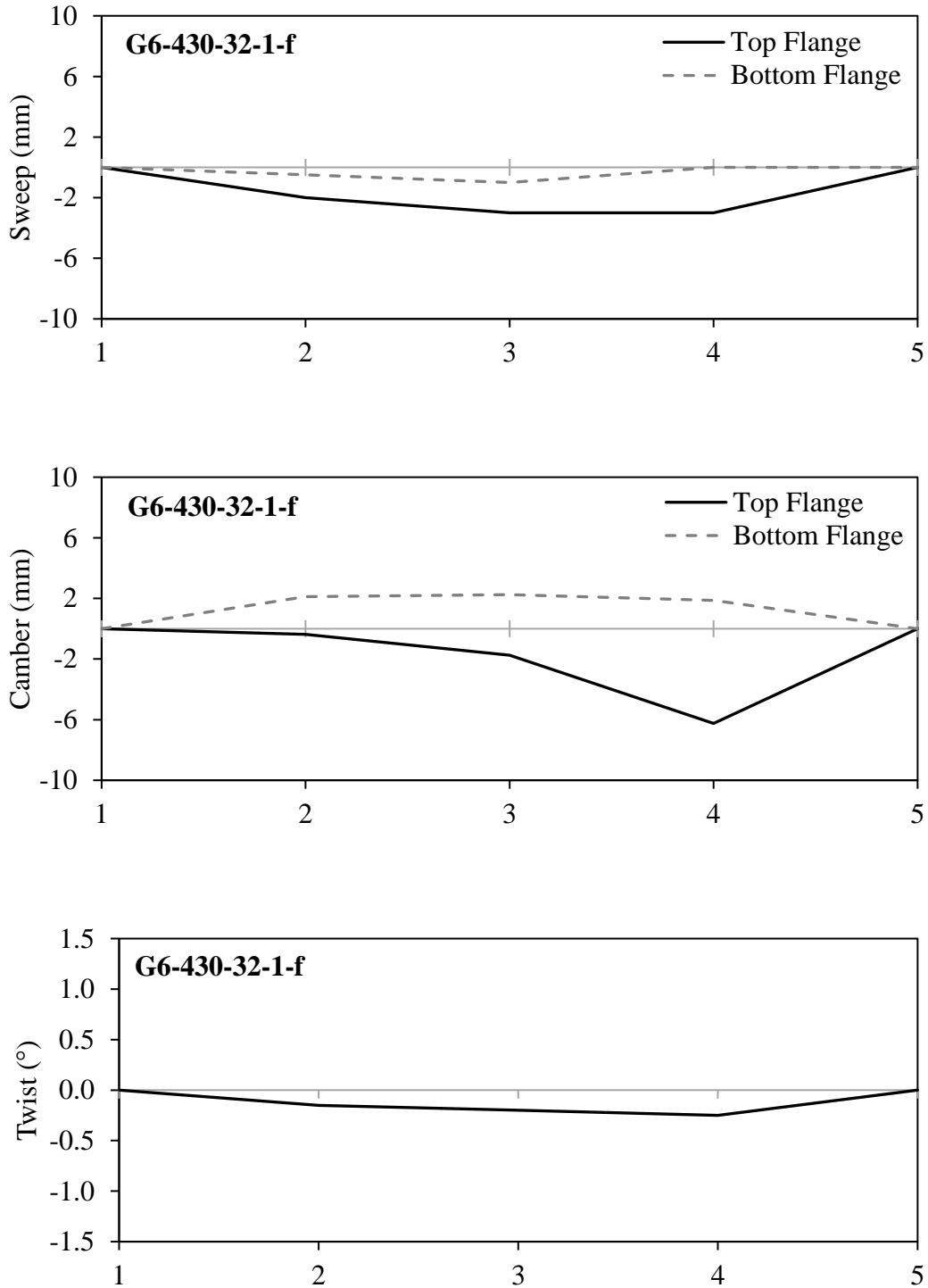


Figure B-3: Initial geometric imperfections of G6-430-32-1-f

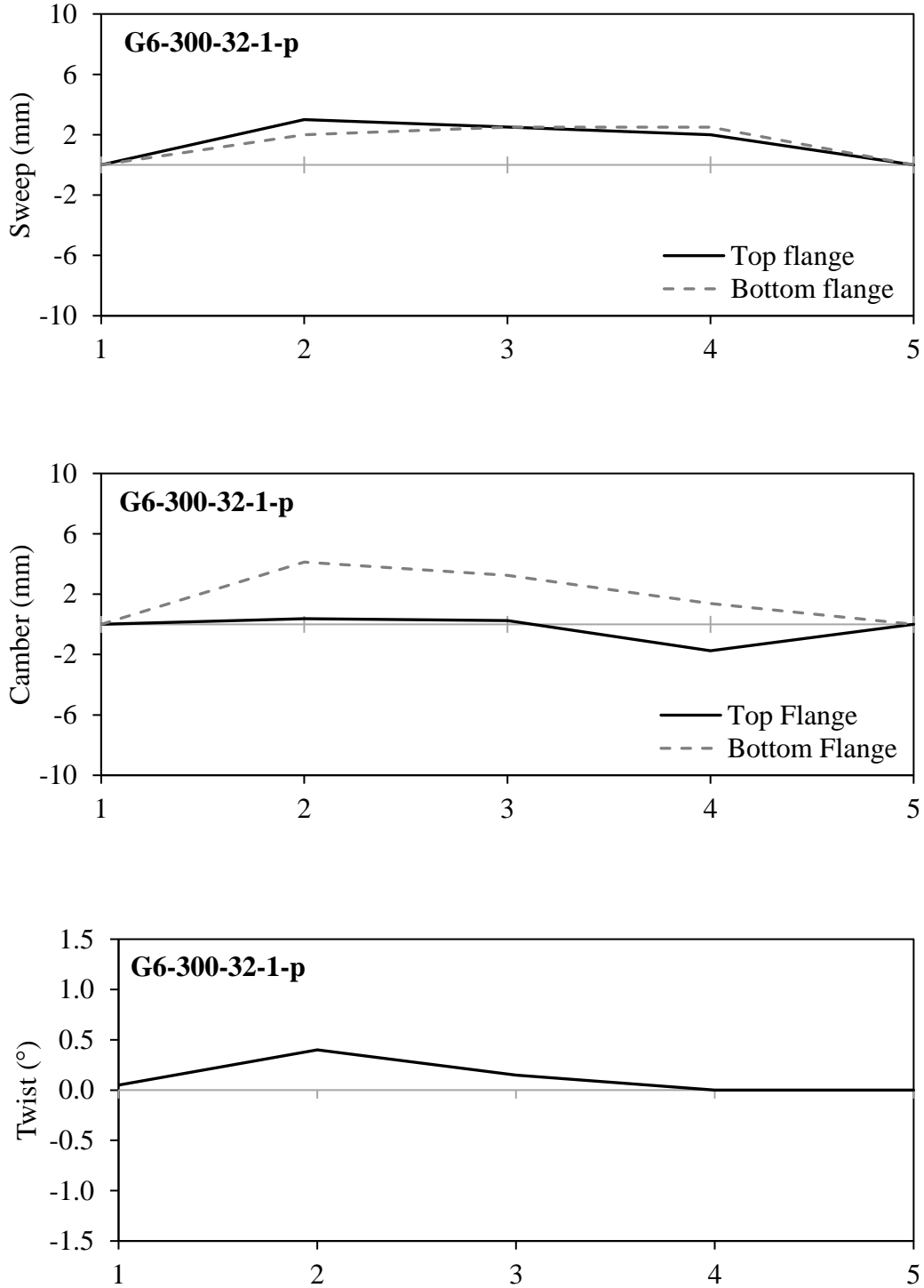


Figure B-4: Initial geometric imperfections of G6-300-32-1-p

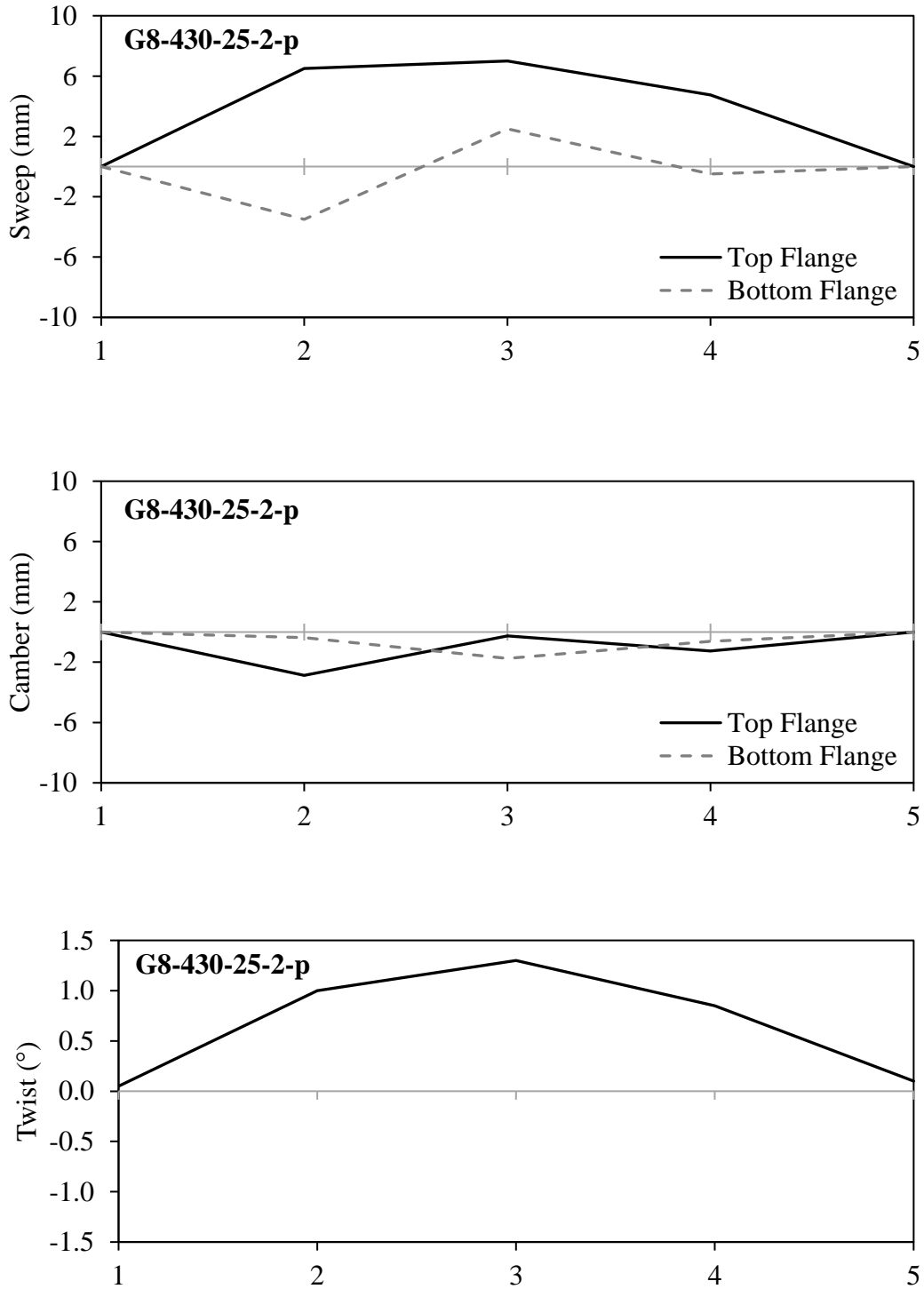


Figure B-5: Initial geometric imperfections of G8-430-25-2-p

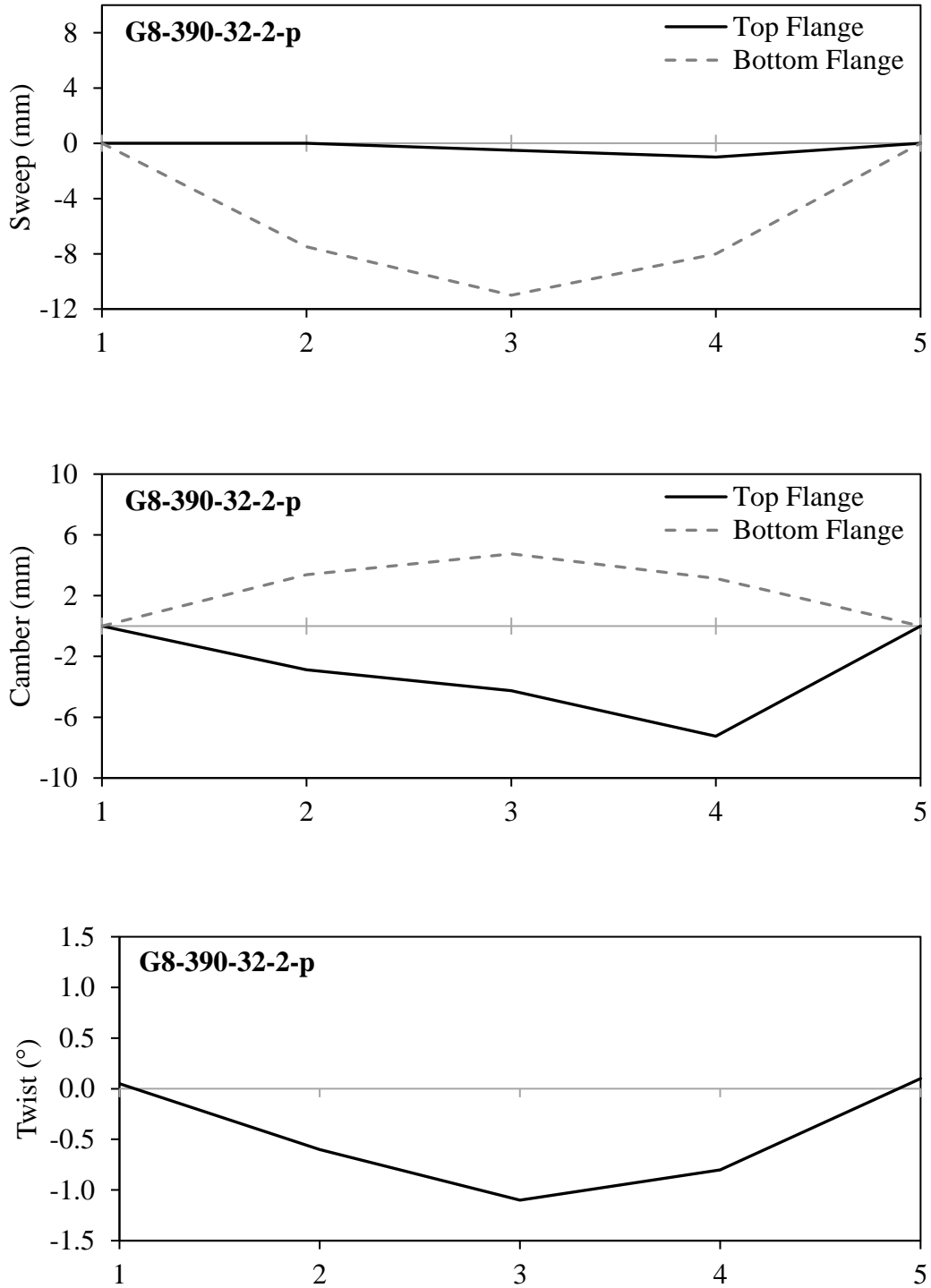


Figure B-6: Initial geometric imperfections of G8-390-32-2-p

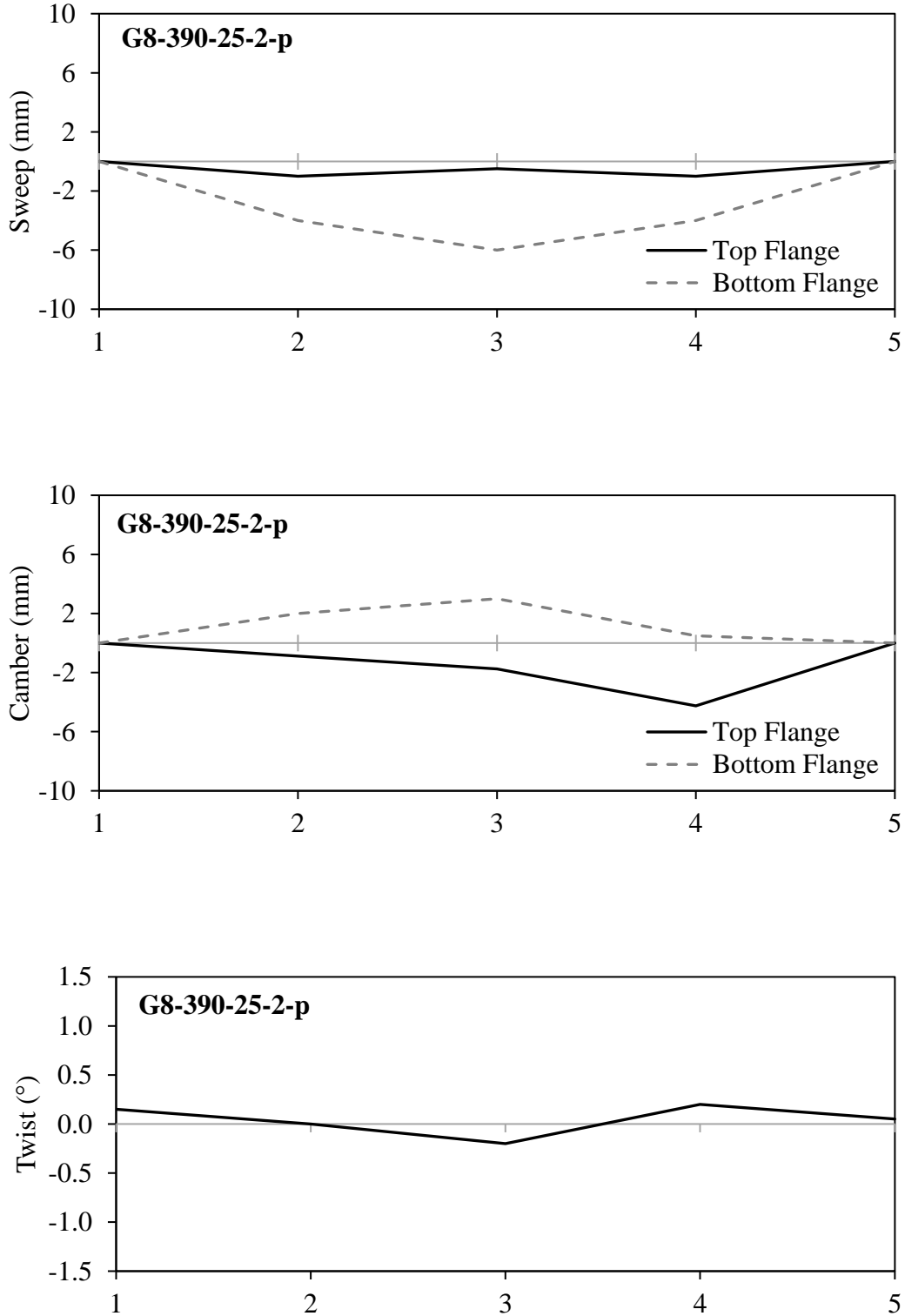


Figure B-7: Initial geometric imperfections of G8-390-25-2-

## Appendix C: Material Test Results

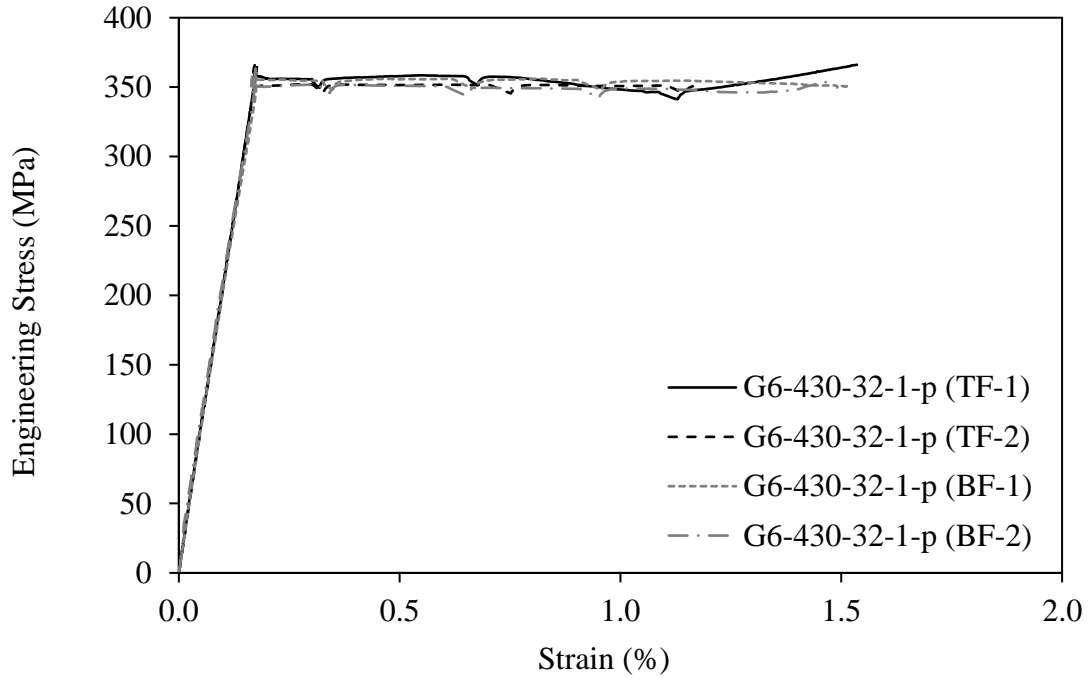


Figure C-1: Engineering stress–strain response of 31.8 mm (1.25 in.) thick coupons in the longitudinal direction

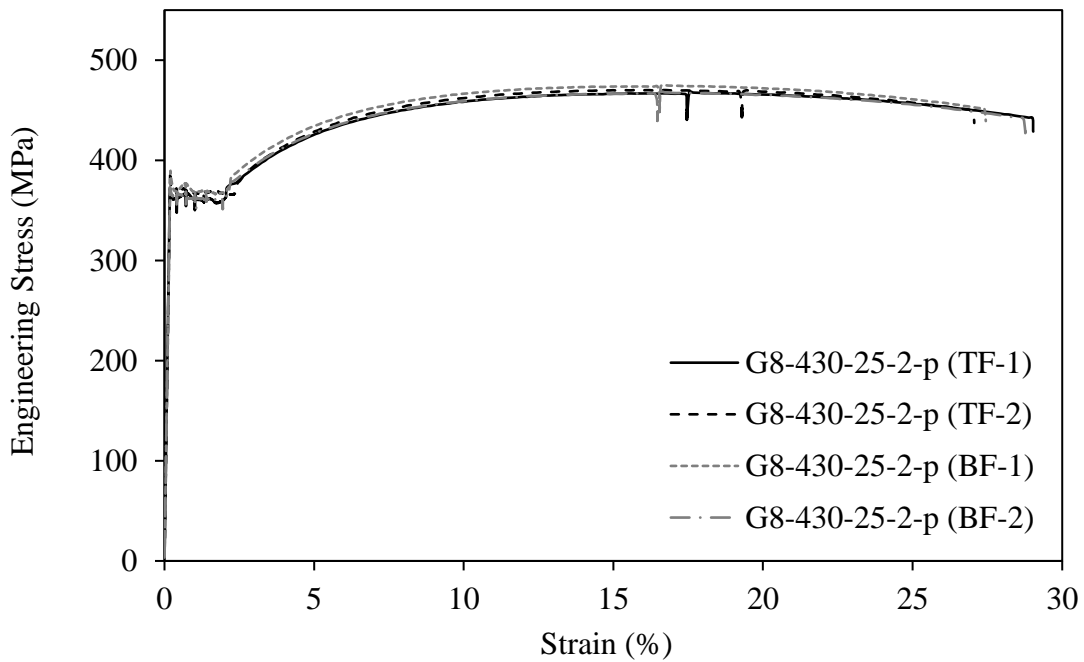


Figure C-2: Engineering stress–strain response of 25.4 mm (1 in.) thick coupons in the longitudinal direction

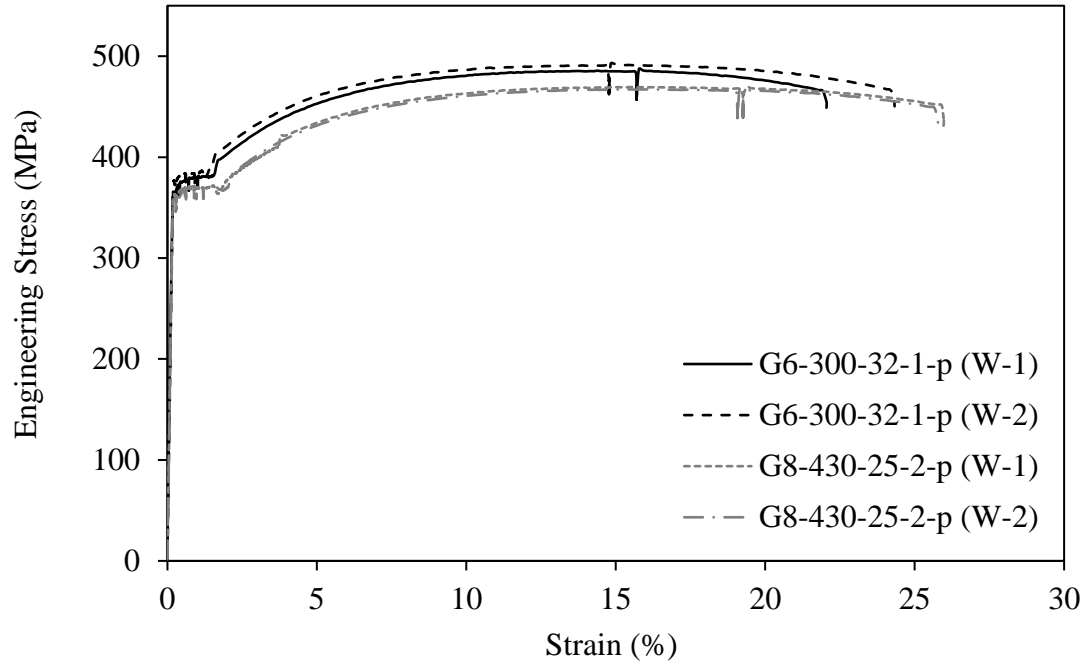


Figure C-3: Engineering stress–strain response of 12.7 mm (0.5 in.) thick coupons in the longitudinal direction

## Appendix D: Numerical Analysis Load–Displacement Curves

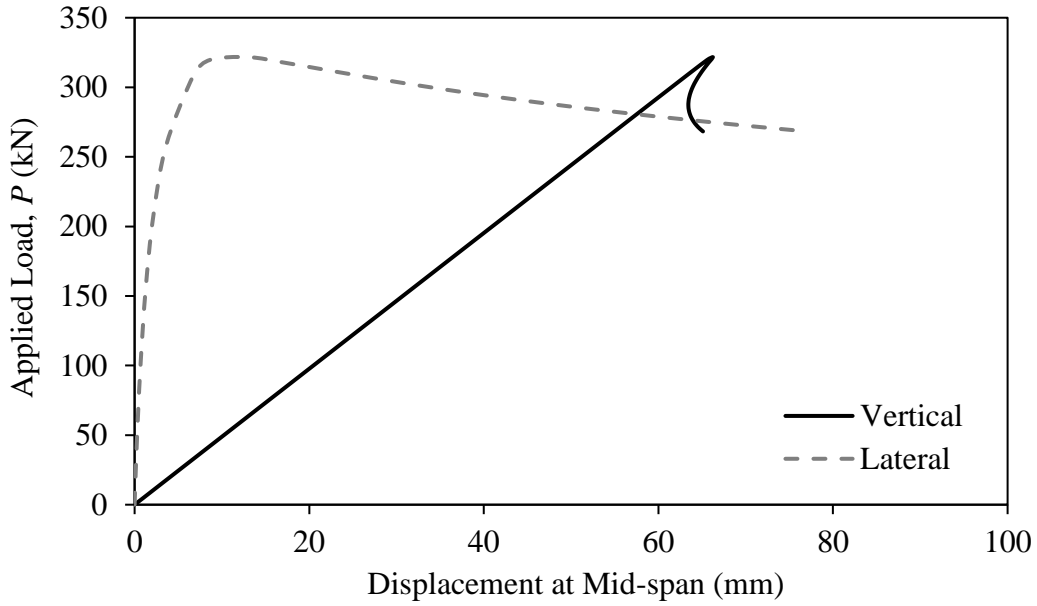


Figure D-1: Predicted load–displacement response of G6-470-32-2-p

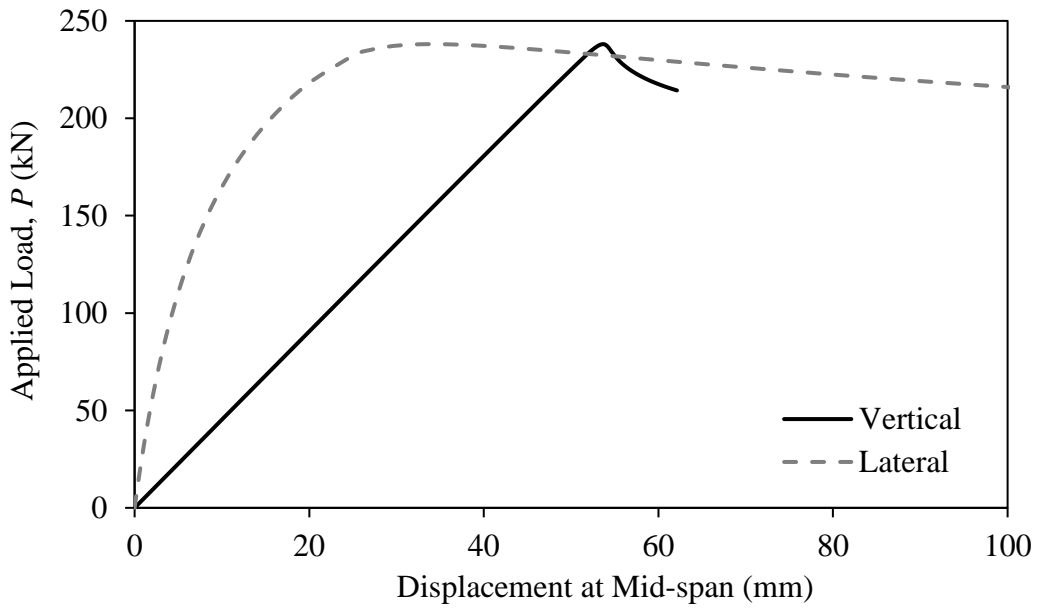


Figure D-2: Predicted load–displacement response of G6-430-32-1-p/f

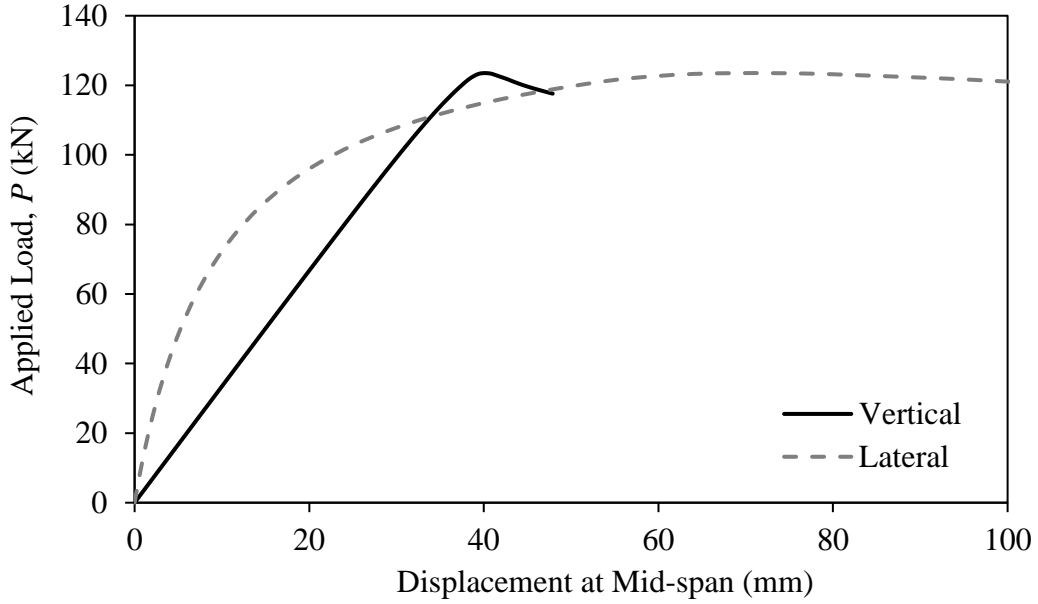


Figure D-3: Predicted load–displacement response of G6-300-32-1-p

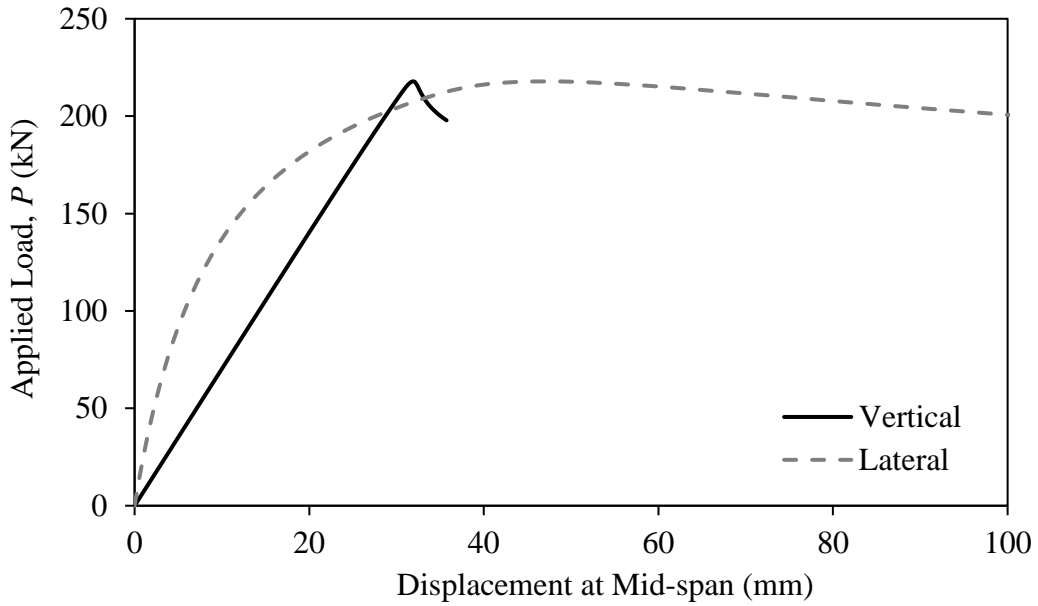


Figure D-4: Predicted load–displacement response of G8-430-25-2-p

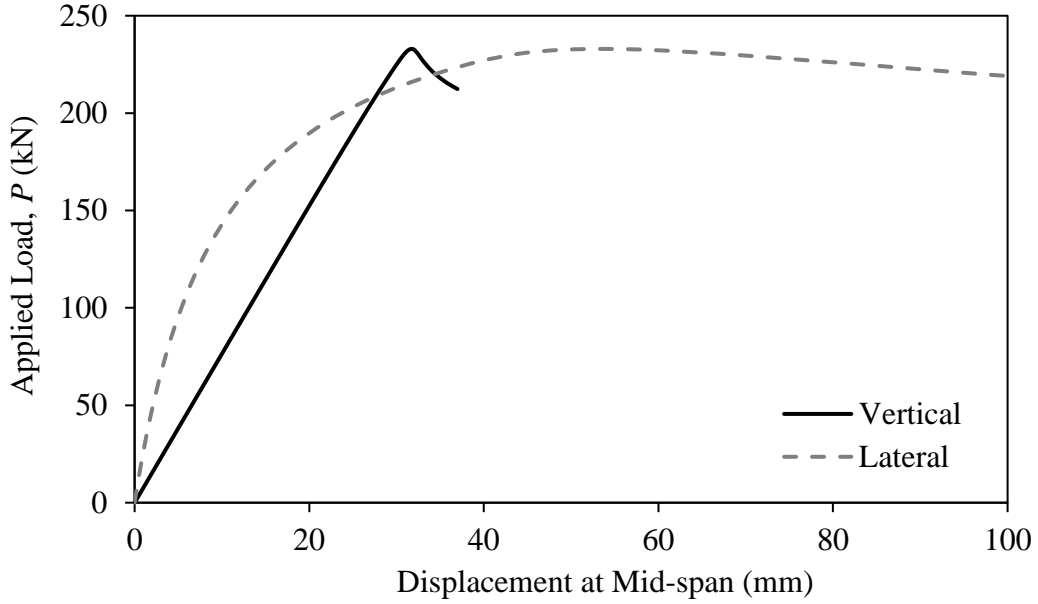


Figure D-5: Predicted load–displacement response of G8-390-32-2-p

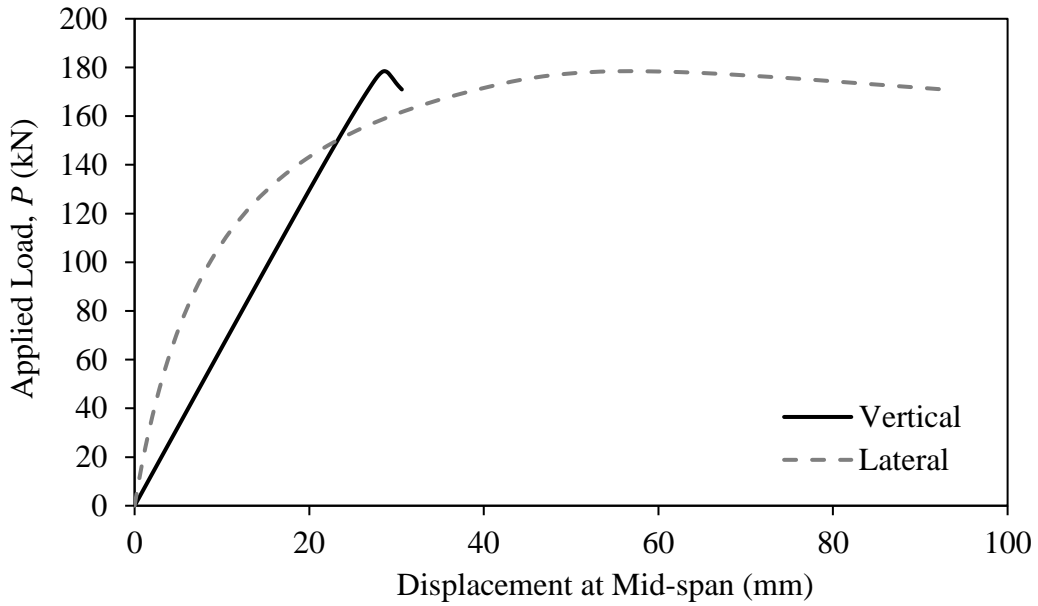


Figure D-6: Predicted load–displacement response of G8-390-25-2-p

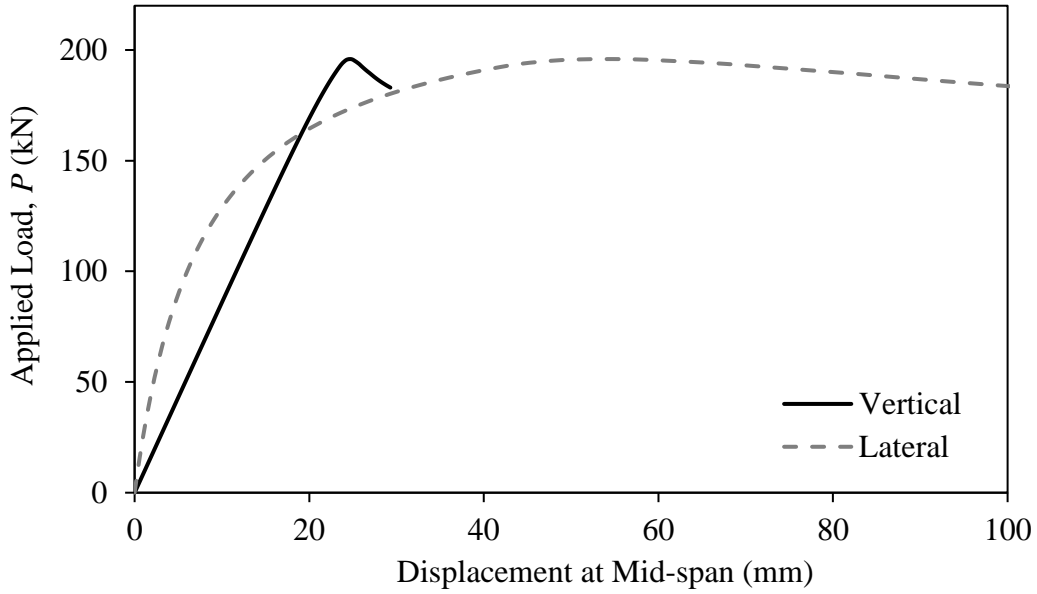


Figure D-7: Predicted load–displacement response of G9-360-32-3-p/f

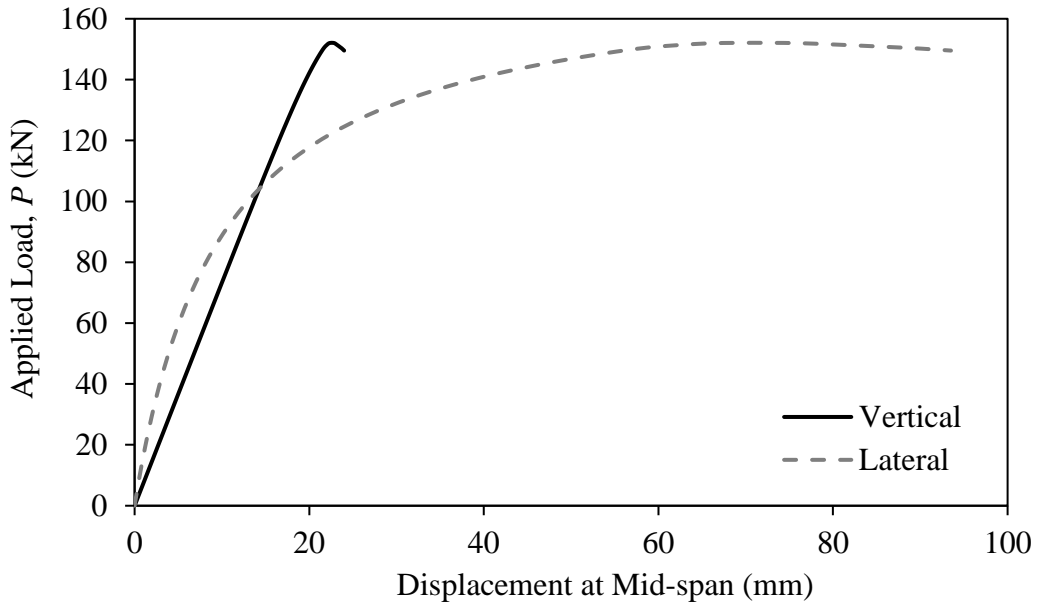


Figure D-8: Predicted load–displacement response of G9-360-25-3-3-f

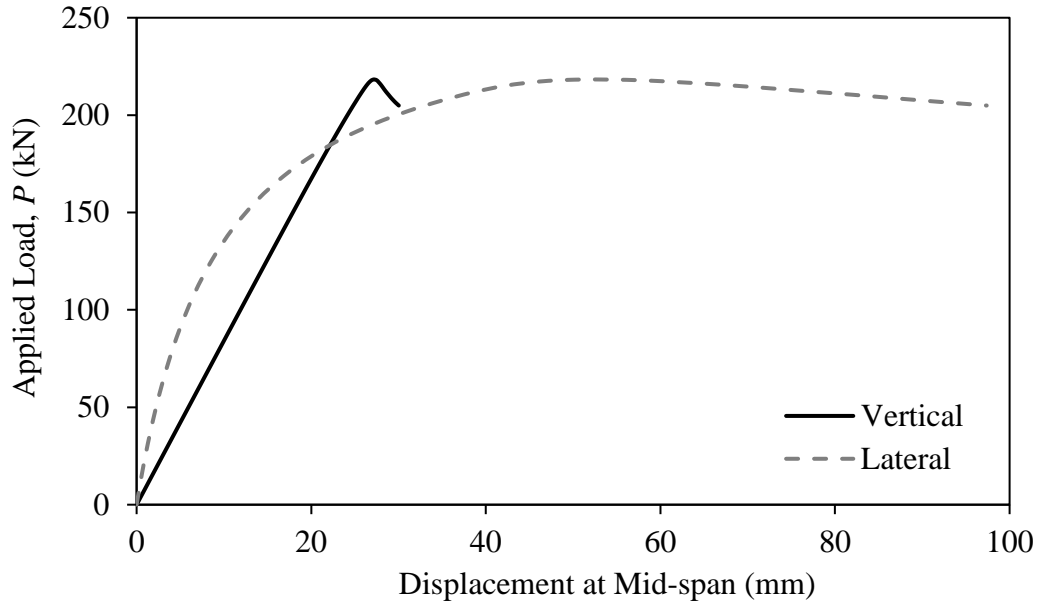


Figure D-9: Predicted load–displacement response of G9-430-25-3-f

## Appendix E: Experimental Load–Displacement Curves

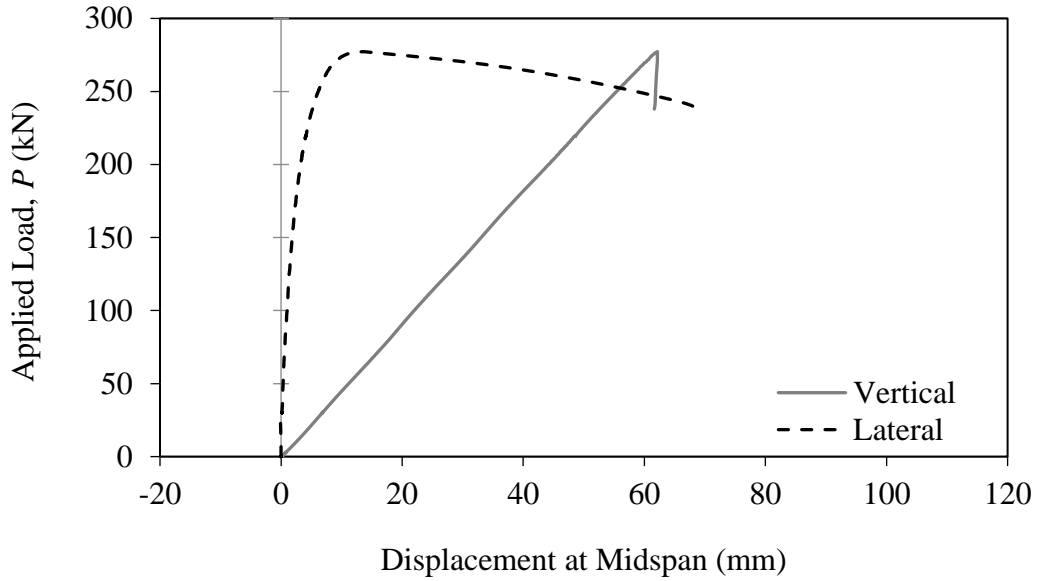


Figure E-1: Experimental load–displacement response of G6-470-32-2-p

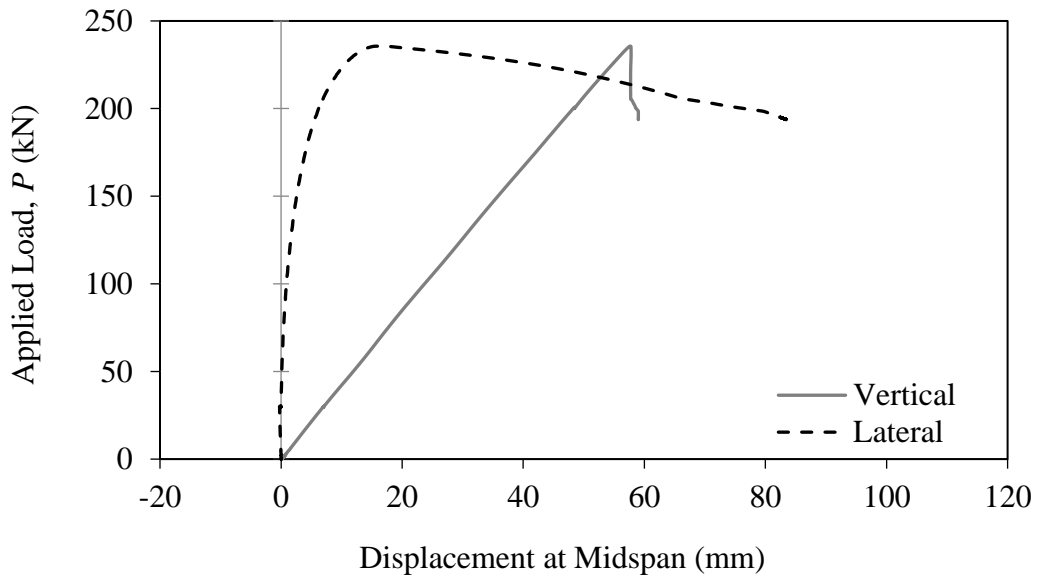


Figure E-2: Experimental load–displacement response of G6-430-32-1-p

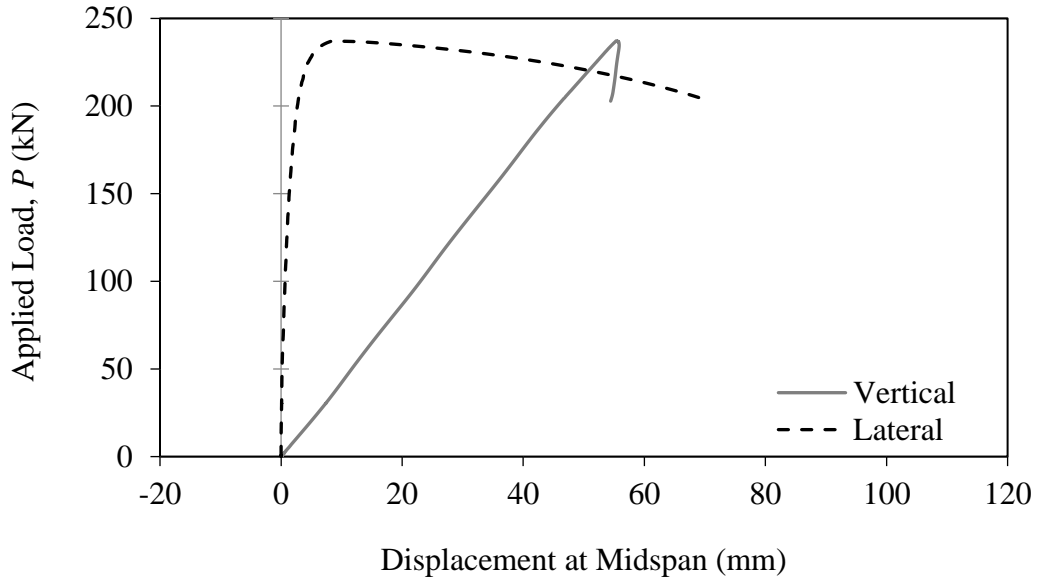


Figure E-3: Experimental load–displacement response of G6-430-32-1-f

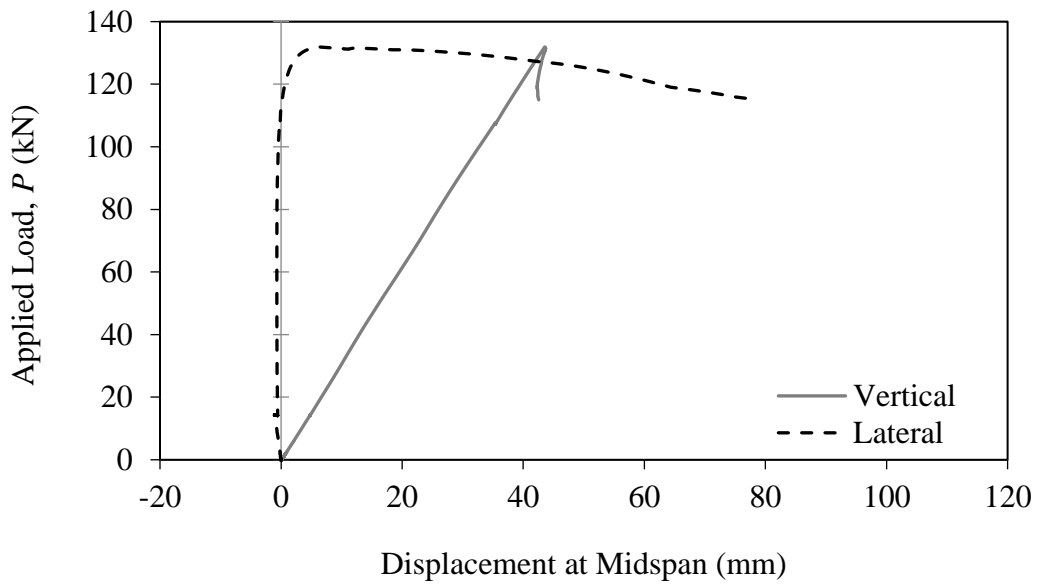


Figure E-4: Experimental load–displacement response of G6-300-32-1-p

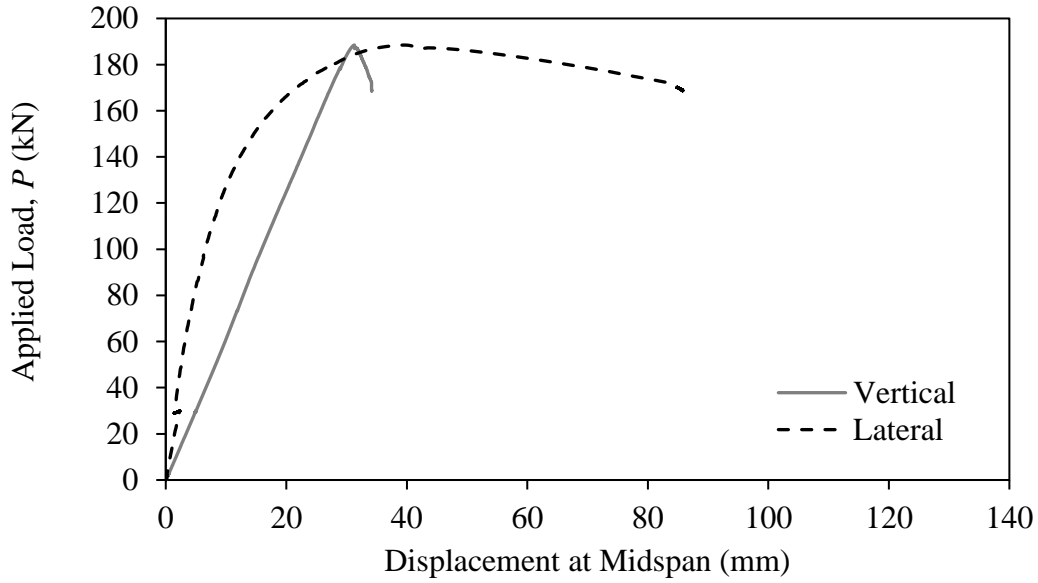


Figure E-5: Experimental load–displacement response of G8-430-25-2-p

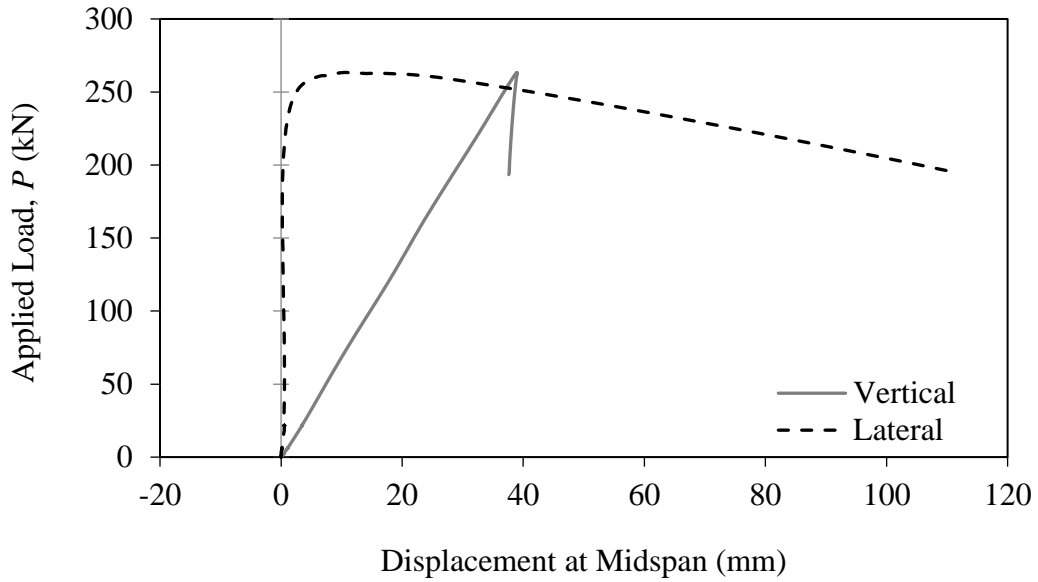


Figure E-6: Experimental load–displacement response of G8-390-32-2-p

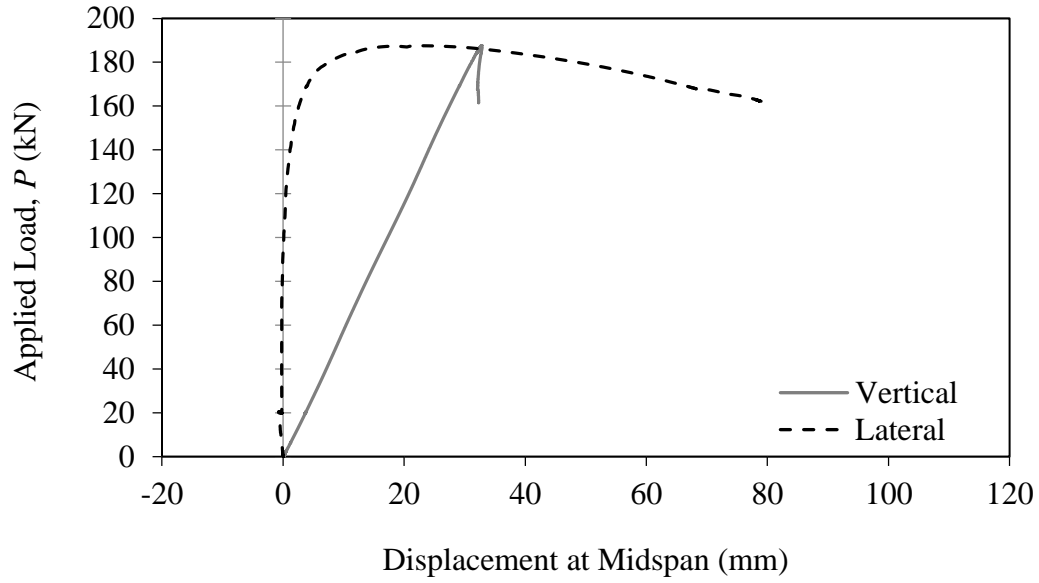


Figure E-7: Experimental load–displacement response of G8-390-25-2-p